UNIVERSITY OF PUERTO RICO

STUDIES OF STRUCTURAL, ELECTRICAL AND FERROELECTRIC PROPERTIES OF RARE-EARTH SUBSTITUTED BISMUTH TITANATE FILMS

by

RICARDO MELGAREJO

A Thesis Submitted In Partial Fulfillment of The Requirements for the Degree of

DOCTOR OF PHILOSOPHY

Program in Chemical Physics
Department of Physics
Faculty of Natural Sciences

Supervised by

Prof. Maharaj S. Tomar

San Juan, Puerto Rico
MAY 2007

STUDIES OF STRUCTURAL, ELECTRICAL AND FERROELECTRIC PROPERTIES OF RARE-EARTH SUBSTITUTED BISMUTH TITANATE FILMS

ACCEPTED BY FACULTY OF THE CHEMICAL PHYSICS PROGRAM OF THE UNIVERSITY OF PUERTO RICO
IN PARTIAL FULFILLMENT OF THE REQUIREMENTS FOR THE DEGREE OF DOCTOR OF PHILOSOPHY

Dr. Maharaj S. Tomar
THESIS ADVISOR

Dr. Ram S. Katiyar
THESIS COMMITTEE MEMBER

Dr. Yasuyuki Ishikawa
THESIS COMMITTEE MEMBER

TABLE OF CONTENTS

LIST OF FIGURES--VII

LIST OF TABLES---XIII

LIST OF ABBREVIATIONS--XIV

ABSTRACT---XV

PUBLICATIONS AND PRESENTATIONS-------------------------------------XVI

ACKNOWLEDGEMENTS---XXII

Chapter 1

Introduction to electroceramics

PAGE

1.1 Introduction---**1**

1.2 Ferroelectric materials--**2**

1.3 Ferroelectric domains--**10**

1.4 Poling of ferroelectrics---**15**

1.5 Ferroelectric hysteresis loop and polarization switching---------------**17**

1.6 Ferroelectric memories--**20**

1.7 Phase transition by Raman spectroscopy--------------------------------**24**

1.8 Research Background--**26**

1.9 Problem definition--**33**

1.10 References---**34**

Chapter 2

Experimental techniques

2.1 Introduction--**37**

2.2 Preparation techniques--37

2.2.1 Sol-gel technique--**38**

2.2.2 Sol-gel chemistry--**39**

2.2.2.1 2-Methoxyethanol Solution synthesis-------------------------------**40**

2.2.2.2. Hybrid Solution synthesis--**40**

2.2.2.3. Metalorganic-Deposition Solution Synthesis----------------------**41**

2.3 Film deposition and heat treatment--------------------------------------**42**

2.3.1. Preparing of lanthanum (La) substituted BTO films----------------**44**

2.3.2. Preparing of neodymium (Nd) substituted BTO films-------------**46**

2.3.3. Preparing of Samarium (Sm) substituted BTO films---------------**47**

2.3.4. Preparing of Gadolinium (Gd) substituted BTO films-------------**49**

2.4. Characterization techniques--**51**

2.4.1. Films thickness measurements---------------------------------------**51**

2.5. Structural and Microstructure---**53**

2.5.1. X-ray diffraction technique---------------------------------------**53**

2.5.2. Micro-Raman Spectroscopy--**57**
2.6Ferroelectric, Fatigue, Dielectric and Leakage measurements-----------**60**

2.6.1. Electrodes ---**60**

2.6.2. Hysteresis and Fatigue measurements-------------------------------**60**

2.6.3. Dielectric measurements---**61**

2.6.4 Current- Voltage (I-V) Characteristics-------------------------------**62**

2.7 References---**63**

Summary (chapter 3-6)--**65**

Chapter 3

Studies of $Bi_{4-x}La_xTi3O_{12}$ for ferroelectric devices

3.1 Introduction---**67**

3.2 Experimental Details --**69**

3.3 Results and Discussions ---**70**

3.3.1 XRD analysis --**70**

3.3.2 Micro Raman analysis --**74**

3.3.3 Ferroelectric properties of $Bi_{4-x}La_xTi_3O_{12}$ thin films ----------------**83**

3.3.4 Dielectric properties of $Bi_{4-x}La_xTi_3O_{12}$ thin films---------------------**89**

3.3.5 Leakage current properties of $Bi_{4-x}La_xTi_3O_{12}$ thin films--------------**92**

3.4 Conclusions--**94**

3.5 References---**95**

Chapter 4

Studies of $Bi_{4-x}Nd_xTi_3O_{12}$ for ferroelectric devices

4.1 Experimental Details --**98**

4.2 Results and Discussions --**99**

4.2.1 XRD analysis ---**99**

4.2.2 Micro Raman analysis ---**103**

4.2.3 Ferroelectric, properties of $Bi_{4-x}Nd_xTi_3O_{12}$ thin films ------------**108**

4.2.4 Dielectric properties of $Bi_{4-x}Nd_xTi_3O_{12}$ thin films ----------------**116**

4.2.5 Leakage current properties of $Bi_{4-x}Nd_xTi_3O_{12}$ thin films ---------**118**

4.4 Conclusions--**121**

4.5 References---**122**

Chapter 5

Studies of $Bi_{4-x}Sm_xTi_3O_{12}$ for ferroelectric devices

5.1 Experimental Details ---**123**

5.2 Results and Discussions --**125**

5.2.1 XRD analysis --**125**

5.2.2 Micro Raman analysis --**130**

5.2.3 Ferroelectric properties of $Bi_{4-x}Sm_xTi_3O_{12}$ thin films -------------**134**

5.2.4 Dielectric properties of $Bi_{4-x}Sm_xTi_3O_{12}$ thin films-----------------**140**

5.2.5 Leakage current propiertes of $Bi_{4-x}Sm_xTi_3O_{12}$ thin films-----------**142**

5.3 Conclusions---**145**

5.4 References--**145**

Chapter 6

Studies of $Bi_{4-x}Gd_xTi_3O_{12}$ for ferroelectric devices

6.1 Introduction---**148**

6.2 Experimental Details --**148**

6.3 Results and Discussions --**150**

6.3.1 XRD analysis --**150**

6.3.2 Micro Raman analysis ---**154**

6.3.3 Ferroelectric properties of $Bi_{4-x}Gd_xTi_3O_{12}$ thin films --------------- **159**

6.3.4 Dielectric properties of $Bi_{4-x}Gd_xTi_3O_{12}$ thin films ------------------ **163**

6.3.5 Leakage current properties of $Bi_{4-x}Gd_xTi_3O_{12}$ thin films ------------**167**

6.4 Magnetic properties---**169**

6.5 Conclusions--**171**

6.6 References---**173**

Chapter 7

Conclusions

7.1 Conclusions--**174**

LIST OF FIGURES

1.1	Hysteresis loop of a ferroelectric material	----------**3**
1.2	ABO_3 perovskite unit cell	----------**4**
1.3	a) Hysteresis of a single ferroelectric crystallite b) Hysteresis loop for rhombohedral polycrystalline ferroelectric	----------**7**
1.4	Interrelationship of piezoelectric and subgroups on the basis of symmetry.	----------**12**
1.5	Illustration of (*a*) 180° and (*b*) 90° ferroelectric domains and domain-wall regions in a tetragonal perovskite ferroelectric.	----------**13**
1.6	A polycrystalline ferroelectric with random orientation of grains before and after poling. Many domain walls are present in the poled material, however, the net remanent polarization is nonzero.	----------**16**
1.7	Ferroelectric (*P*–*E*) hysteresis loop. Circles with arrows represent the polarization state of the material at the indicated fields. The symbols are explained in the text.	----------**19**
1.8	One half of unit cell of $Bi_4Ti_3O_{12}$	----------**28**
1.9	Structure of lanthanum substituted bismuth titanate	----------**31**
1.10	a) The refined unit-cell structure of BNdT at 298 k. b) the refined result of Ti1 and Ti2 sites projected on the *b*-*c* plane. c) The polarization vector of the Ti2 site projected on the *b*-*c* plane.	----------**32**
2.1	Flow chart of the sol-gel process of BLaT sol and thin film preparation.	----------**43**
2.2	Schematic of the filmetrics system.	----------**52**
2.3	Bragg’s law	----------**54**

2.4 Experimental set up of the micro Raman scattering ----------**59**

3.1 X-ray diffraction patterns of $Bi_{4-x}La_xTi_3O_{12}$ (BLaT) thin films on $Pt/TiO_2/SiO_2/Si$ substrate for the compositions x = 0.00, 0.16, 0.26, 0.36, 0.46, 0.56, 0.75, 0.95, 1.00 and 1.50. The inset shows the variation of the FWHM of (117) peak with La content. ----------**71**

3.2 Variation in lattice parameters of BLaT thin films with different La content. ----------73

3.3 SEM micrographs of (a) BTO, (b) x = 0.26, (c) x = 0.56, (d) x = 0.75 (e) x = 1.50 Lanthanum content in BTO thin films on $Pt/TiO_2/SiO_2/Si$ substrate. ----------75

3.4 Room temperature Raman spectra of $Bi_{4-x}La_xTi_3O_{12}$ films on a Pt substrate ($Pt/TiO_x/SiO_2/Si$) for x = 0.00, 0.16, 0.26, 0.36, 0.46, 0.56, 0.75, 0.95, and 1.50 composition. The indexes in the figure indicate peculiar modes to the local structures. -----------77

3.5 Raman frequencies as a function of Lanthanum compositions in $Bi_{4-x}La_xTi_3O_{12}$ thin films. -----------78

3.6 Room temperature raman squared frequency of the soft mode as a function of Lanthanum compositions in $Bi_{4-x}La_xTi_3O_{12}$ thin films. -----------**82**

3.7 a) Superposition of Ferroelectric response of the $Bi_{4-x}La_xTi_3O_{12}$ thin films for x = 0.00, 0.46, 0.56, 0.56 (annealed electrode), 0.75 and 0.95, on Pt ($Pt/TiO_2/SiO_2/Si$) substrate at 700°C. -----------**84**

3.7 b) Separate Ferroelectric response of the $Bi_{4-x}La_xTi_3O_{12}$ thin films for x = 0.00, 0.46, 0.56, 0.56 (annealed electrode), 0.75 and 0.95, on Pt ($Pt/TiO_2/SiO_2/Si$) substrate at 700°C. -----------**85**

3.8 The values of a) the remnant polarization (P_r) and b) the coercive field (E_c) of the $Bi_{4-x}La_xTi_3O_{12}$ thin films for x = 0.00, 0.46, 0.56 (annealed electrode), 0.75, and 0.95, on Pt ($Pt/TiO_2/SiO_2/Si$) substrate at 700°C ------------**86**

3.9 a) Ferroelectric response of the $Bi_{3.44}La_{0.56}Ti_3O_{12}$ thin film ------------**88**

deposited on Pt ($Pt/TiO_2/SiO_2/Si$) substrate and annealed at 7000C, for 1 cycle and after fatigue $1.4x10^9$ cycles. b) Fatigue characteristics of the $Bi_{3.44}La_{0.56}Ti_3O_{12}$ film under $1.4x10^9$ cycles at a frequency of 1 MHz.

3.10 a) Dielectric constant and loss (tan δ) vs applied electric field on $Bi_{3.44}La_{0.56}Ti_3O_{12}$ film at 1 MHz, and b) dielectric constant measured at 25^0C as a function of frequency in the range between 1 kHz and 1 MHz. -----------**91**

3.11 Leakage current at room temperature of the $Bi_{4-x}La_xTi_3O_{12}$ thin films deposited on Pt ($Pt/TiO_2/SiO_2/Si$) substrate and annealed at 700ºC for the compositions: x = 0.00, 0.46, 0.56, 0.75, 0.95 and 1.50. -----------**93**

4.1 X-ray diffraction patterns of $Bi_{4-x}Nd_xTi_3O_{12}$ (BNdT) thin films on $Pt/TiO_2/SiO_2/Si$ substrate for the compositions x = 0.00, 0.26, 0.46, 0.56, 0.75, 0.85, 1.00 and 2.00, the inset shows the variation of the FWHM of (117) peak with Nd content. ----------**100**

4.2 Variation in lattice parameters of BNdT thin films with different Nd content. ---------**102**

4.3 SEM micrographs of (a) BTO, (b) x = 0.26, (c) x = 0.40 and d) x = 0.56, Neodymium content in BTO thin films on $Pt/TiO_2/SiO_2/Si$ substrate. ----------**104**

4.4 Room temperature Raman spectra of $Bi_{4-x}Nd_xTi_3O_{12}$ films on a Pt substrate ($Pt/TiO_x/SiO_2/Si$) for x = 0.00, 0.26, 0.46, 0.56, 0.75, 0.85, 1.00 and 2.00 composition. The indexes in the figure indicate peculiar modes to the local structures. ----------**106**

4.5 Raman frequencies as a function of Neodymium compositions in $Bi_{4-x}Nd_xTi_3O_{12}$ thin films. ----------**107**

4.6 a) Ferroelectric response of the $Bi_{4-x}Nd_xTi_3O_{12}$ thin films for x = 0.00, 0.26, 0.36,0.40, 0.46, 0.56, 0.56 (annealed electrode), 0.75, 0.85 and 1.00, on Pt ($Pt/TiO_2/SiO_2/Si$) substrate at 700ºC ----------**110**

4.6 b) Separate ferroelectric response of the $Bi_{4-x}Nd_xTi_3O_{12}$ thin films for x = 0.00, 0.26, 0.36,0.40, 0.46, 0.56, 0.56 (annealed ----------**111**

electrode), 0.75, 0.85 and 1.00, on Pt ($Pt/TiO_2/SiO_2/Si$) substrate at 700ºC

4.7 The values of a) the remnant polarization (P_r) and b) the coercive field (E_c) of the $Bi_{4-x}Nd_xTi_3O_{12}$ thin films for x = 0.00, 0.26, 0.36,0.40, 0.46, 0.56 (annealed electrode), 0.75, 0.85 and 1.00, on Pt ($Pt/TiO_2/SiO_2/Si$) substrate at 700ºC. ----------**112**

4.8 Compares the polarization vs electric field (P-E) switching curve of the a) highly c-axis oriented BNdT film ($Bi_{3.44}Nd_{0.56}Ti_3O_{12}$ with x = 0.85) with that of the b) (117) preferred oriented $Bi_{3.44}Nd_{0.56}Ti_3O_{12}$ film ----------**113**

4.9 a) Ferroelectric response of the $Bi_{3.44}Nd_{0.56}Ti_3O_{12}$ thin film deposited on Pt ($Pt/TiO_2/SiO_2/Si$) substrate and annealed at 7000C, for 1 cycle and after fatigue 10^9 cycles. b) Fatigue characteristics of the $Bi_{3.44}Nd_{0.56}Ti_3O_{12}$ film under 10^9 cycles at a frequency of 1 MHz. ----------**115**

4.10 a) Dielectric constant and loss (tan δ) vs applied electric field on $Bi_{3.44}Nd_{0.56}Ti_3O_{12}$ film at 1 MHz, and b) dielectric constant measured at 25^0C as a function of frequency in the range between 1 kHz and 1 MHz ----------**117**

.

4.11 Leakage current at room temperature of the $Bi_{4-x}Nd_xTi_3O_{12}$ thin films deposited on Pt ($Pt/TiO_2/SiO_2/Si$) substrate and annealed at 700ºC for the compositions: x = 0.00, 0.26, 0.36, 0.50, 0.56, 0.75, 0.85 and 1.00. ----------**119**

5.1 X-ray diffraction patterns of $Bi_{4-x}Sm_xTi_3O_{12}$ thin films on $Pt/TiO_2/SiO_2/Si$ substrate for the compositions x = 0.00, 0.36, 0.46, 0.56, 0.70, 0.75, and 0.85. The inset shows the variation of the FWHM of (117) peak with Sm content. ----------**126**

5.2 Variation in lattice parameters of BSmT thin films with different Sm content. ----------**128**

5.3 SEM micrographs of (a) BTO, (b) x = 0.56, (c) x = 0.70, (d) x = 0.80 Samarium content in $Bi_{4-x}Sm_xTi_3O_{12}$ thin films on $Pt/TiO_2/SiO_2/Si$ substrate. ----------**129**

5.4 Room temperature Raman spectra of $Bi_{4-x}Sm_xTi_3O_{12}$ films on a Pt substrate ($Pt/TiO_x/SiO_2/Si$) for x = 0.00, 0.46, 0.56, ----------**132**

0.70, 0.75, and 0.85 composition. The indexes in the figure indicate peculiar modes to the local structures.

5.5 Raman frequencies as a function of Samarium compositions in $Bi_{4-x}Sm_xTi_3O_{12}$ thin films. ----------**133**

5.6 Ferroelectric response of the $Bi_{4-x}Sm_xTi_3O_{12}$ thin films for x = 0.00, 0.46, 0.50, 0.60, 0.70, 0.70 (annealed at 750^0C), 0.75 and 0.85, on Pt ($Pt/TiO_2/SiO_2/Si$) substrate at 700ºC. ----------**135**

5.7 The values of a) the remnant polarization (P_r) and b) the coercive field (E_c) of the $Bi_{4-x}Sm_xTi_3O_{12}$ thin films for x = 0.00, 0.46, 0.60, 0.70, 0.75 and 0.85, on Pt ($Pt/TiO_2/SiO_2/Si$) substrate at 700ºC. ----------**136**

5.8 a) Ferroelectric response of the $Bi_{3.30}Sm_{0.70}Ti_3O_{12}$ thin film deposited on Pt ($Pt/TiO_2/SiO_2/Si$) substrate and annealed at 700^0C, for 1 cycle and after fatigue $1.4x10^9$ cycles.
b) Fatigue characteristics of the $Bi_{3.30}Sm_{0.70}Ti_3O_{12}$ film under $1.4x10^9$ cycles at a frequency of 1 MHz. ----------**138**

5.9 Fatigue characteristics of the $Bi_{3.30}Sm_{0.70}Ti_3O_{12}$ film annealed at 750ºC under $4.4x10^9$ cycles at a frequency of 1 MHz. ----------**139**

5.10 Dielectric constant measured at 25^0C on $Bi_{3.30}Sm_{0.70}Ti_3O_{12}$ film as a function of frequency in the range between 1 kHz and 1 MHz. ----------**141**

5.11 Leakage current at room temperature of the $Bi_{4-x}Sm_xTi_3O_{12}$ thin films deposited on Pt ($Pt/TiO_2/SiO_2/Si$) substrate and annealed at 700ºC for the compositions: x = 0.00, 0.46, 0.60, 0.70, and 0.75. ----------**143**

6.1 X-ray diffraction patterns of $Bi_{4-x}Gd_xTi_3O_{12}$ (BGdT) thin films on $Pt/TiO_2/SiO_2/Si$ substrate for the compositions x = 0.00, 0.30, 0.46, 0.56, 0.60, 0.70, 0.85, and 1.00. The inset shows the variation of the FWHM of (117) peak with Gd content. ----------**151**

6.2 Variation in lattice parameters of BGdT thin films with different Gd content. ----------**153**

6.3	SEM micrographs of (a) BTO, (b) x = 0.30, (c) x = 0.50 and (d) x = 1.00. Gadolinium content in BTO thin films on $Pt/TiO_2/SiO_2/Si$ substrate.	----------**154**
6.4	Room temperature Raman spectra of $Bi_{4-x}Gd_xTi_3O_{12}$ films on a Pt substrate ($Pt/TiO_x/SiO_2/Si$) for x = 0.00, 0.20, 0.25, 0.30, 0.46, 0.50, 0,60, 0.70, 0.75, 0.85 and 1.00 composition. The indexes in the figure indicate peculiar modes to the local structures.	----------**156**
6.5	Raman frequencies as a function of Gadolinium compositions in $Bi_{4-x}Gd_xTi_3O_{12}$ thin films.	----------**157**
6.6	Ferroelectric response of the $Bi_{4-x}Gd_xTi_3O_{12}$ thin films for x = 0.00, 0.20, 0.30, 0.36, 0.46, 0.56, 0.60, and 0.70, on Pt ($Pt/TiO_2/SiO_2/Si$) substrate at 700°C.	----------**160**
6.7	The values of a) the remnant polarization (P_r) and b) the coercive field (E_c) of the $Bi_{4-x}Gd_xTi_3O_{12}$ thin films for x = 0.00, 0.20, 0.30, 0.36, 0.46, 0.56, 0.60 and 0.70, on Pt ($Pt/TiO_2/SiO_2/Si$) substrate at 700°C.	----------**161**
6.8	Fatigue characteristics of the $Bi_{3.70}Gd_{0.30}Ti_3O_{12}$ film deposited on Pt ($Pt/TiO_2/SiO_2/Si$) substrate and annealed at 700^0C, under $0.4x10^9$ cycles at a frequency of 1 MHz.	----------**163**
6.9	a) Dielectric constant and loss (tan δ) vs applied electric field on $Bi_{3.70}Gd_{0.30}Ti_3O_{12}$ film at 1 MHz, and b) dielectric constant measured at 25^0C as a function of frequency on x= 0.30 ,0.56 and 0.85 in the range between 1 kHz and 1 MHz.	----------**164**
6.10	Leakage current at room temperature of the $Bi_{4-x}Gd_xTi_3O_{12}$ thin films deposited on Pt ($Pt/TiO_2/SiO_2/Si$) substrate and annealed at 700°C for the compositions: x = 0.00, 0.30, 0.56, and 0.85.	----------**167**
6.11	Magnetization as a function of temperature at 100 Oe magnetic field of the powder $Bi_{3.15}Gd_{0.85}Ti_3O_{12}$.	----------**169**
6.12	Magnetization Vs applied magnetic field for $Bi_{3.15}Gd_{0.85}Ti_3O_{12}$ powder at 300 and 5 K.	----------**171**

LIST OF TABLES

1.1 Point groups for the seven-crystal system ----------**11**

1.2 key characteristics of candidate nonvolatile memory technologies ----------**23**

2.1 Precursors used for preparation the $Bi_{4-x}La_xTi_3O_{12}$ sol synthesis. ----------**44**

2.2 Precursors used for preparation the $Bi_{4-x}Nd_xTi_3O_{12}$ sol synthesis. ----------**46**

2.3 Precursors used for preparation the $Bi_{4-x}Sm_xTi_3O_{12}$ sol synthesis. ----------**48**

2.4 Chemical used for preparation the $Bi_{4-x}Gd_xTi_3O_{12}$ sol synthesis. ----------**49**

3.1 Variation of crystallite size for different La content in $Bi_4Ti_3O_{12}$ films ----------**72**

4.1 Variation of crystallite size for different Nd content in $Bi_4Ti_3O_{12}$ films ----------**101**

5.1 Variation of crystallite size for different Sm content in $Bi_4Ti_3O_{12}$ films ----------**127**

6.1 Variation of crystallite size for different Gd content in $Bi_4Ti_3O_{12}$ films ----------**152**

7.1 Results of properties Ferroelectric, dielectric and leakage current of rare earth substituted bismuth titanates ----------174

LIST OF ABBREVIATIONS

BGdT	Gadolinium substituted bismuth titanate
BLSFs	Bismuth layer structured ferroelectric
BLaT	Lanthanum substituted bismuth titanate
BNdT	Neodymium substituted bismuth titanate
BSmT	Samarium substituted bismuth titanate
BTO	Bismuth titanate
CCD	Charge Couple Device
DRAM	Dynamic Random Access Memories
DRO	Destructive readout
EPROM	Erasable programmable read-only memory
EEPROM	Electrically erasable programmable read-only memory
FE	Ferroelectric
FeRAM	Ferroelectric Random Access Memories
FWHM	Full Width at Half the Maxima
IC	integrated circuit
LO	Longitudinal Optic
MOCVD	Metal Organic Chemical Vapor Deposition
MOS	Metal Oxide Semiconductor
MRAM	magnetoresistive random access memory
NDRO	nondestructive readout
PLD	Pulsed Laser Deposition
Pt	Platinum
PLD	Pulsed Laser Deposition
PZT	Lead Zirconate Titanate
SBT	Strontium Bismuth Tantalate
SCLC	Space Charge Limited Current
SQUID	Superconducting quantum interference device
SEM	Scanning Electron Microscopy
SONOS	Silicon oxide nitride oxide silicon
Tc	Temperature Curie
TO	Transversal Optic
XRD	X-Ray Diffraction
ZFC	Zero field cooled

ABSTRACT

In the present research, $Bi_4Ti_3O_{12}$ (BTO) and its rare earth (La, Nd, Sm, Gd)-substituted derivative thin films were synthesized using a sol-gel method and were systematically investigated. Films were deposited by spin coating on Pt ($Pt/TiO_2/SiO_2/Si$) substrates followed by their annealing at 700°C in air. According to the x-ray diffraction analysis of $Bi_{4-x}M_xTi_3O_{12}$ (M = La, Nd, Sm, Gd) patterns showed polycrystalline materials with preferential (117) orientation.Microstructure by SEM and X-ray studies shows that the crystallite sizes decrease as the rare earth (La, Nd, Sm, Gd) content increase.Raman spectroscopy analysis suggest that the Rare earth ions (La^{3+} Nd^{+3}, Sm^{+3}, Gd^{+3}) are incorporated into the Bi site (A site). On the other hand, $Bi_{3.44}La_{0.56}Ti_3O_{12}$, $Bi_{3.44}Nd_{0.56}Ti_3O_{12}$, $Bi_{3.30}Sm_{0.70}Ti_3O_{12}$ and $Bi_{3.70}Gd_{0.30}Ti_3O_{12}$ thin films capacitor showed significantly improved values of the remanent polarization P_r = 47.59, 70, 29 and 27.5 $\mu C/cm^2$ and enhanced fatigue-free behavior respectively. Their dielectric constants and losses were 535, 0.09, 434, 0.07, 344, 0.039 and 333, 0.039 respectively at the frequency 1MHz. At lower field, the leakage current is dominated by ohmic behavior in all thin films. $Bi_{3.70}Gd_{0.30}Ti_3O_{12}$ showed the lowest leakage current 10^{-8} A/cm^2 under low fields. $Bi_{3.15}Gd_{0.85}Ti_3O_{12}$ powder was tested using SQUID, which showed super-paramagnetic at room temperature and magnetic behavior at 5 K with magnetic coercitivity (Hc = 29 Oe).

PUBLICATIONS/PRESENTATIONS

Thesis related Publications:

1. Studies of $Bi_{4-x}Gd_xTi3O12$ Bifunctional Material, M. S. Tomar, **R.E. Melgarejo**, R. Singhal, L.M. Angelats and R.S. Katiyar. Res. Soc. Symp. Proc., Vol **888** 165(2005).

2. Effect of Composition on Ferroelectric Response of $Bi_{4-x}Sm_xTi_3O_{12}$ thin films, S.Dussan, M. S. Tomar, **R.E. Melgarejo**, and R. S. Katiyar. Mater. Res. Soc Symp. Proc., Vol 902E 0902-T03-54.1-092-T03-54.6 (2005).

3. Leakage current and ferroelectric memory in Nd and Sm substituted $Bi_4Ti_3O_{12}$ films, M.S. Tomar, **R.E. Melgarejo**, S.P. Singh, Microelectronic Journal **36** 574 (2005).

4. Ferroelectric Behavior of Sol-Gel Derived $Bi_{4-x}Nd_xTi_3O_{12}$ Thin Films, M.S. Tomar, **R.E. Melgarejo**, A. Hidalgo, S.P. Singh and R.S. Katiyar, Journal Integrated Ferroelectrics. vol. 62, no. 1, pp. 221-227(7) (2004).

5. Ferroelectric memory in La substituted $Bi_4Ti_3O_{12}$ thin films, **R.E. Melgarejo** and M.S. Tomar Mater. Res. Soc Symp. Proc., Vol 784 C11.11.1-C11.11.6 (2004).

6. Large Ferroelectric Polarization in $Bi_{4-x}La_xTi_3O_{12}$ Thin films, **R.E. Melgarejo**, M.S. Tomar, S.P. Singh, Physics of Semiconductor Devices 1133-1135 (2003).

7. Structural and ferroelectric studies of $Bi_{3.44}La_{0.56}Ti_3O_{12}$ films, M.S. Tomar, **R.E. Melgarejo**, A. Hidalgo, S.B. Majumder and R.S. Katiyar, Applied Physics Letters. Vol 83, 341-343 (2003).

8. Large Ferroelectric response $Bi_{4-x}Nd_xTi_3O_{12}$ films prepared by Sol-gel process, **R.E. Melgarejo**, M.S. Tomar, S. Bhaskar, P.S. Dobal and R.S. Katiyar, Applied Physics Letters. Vol 81, 2611-2613 (2002).

9. Synthesis and ferroelectric response of $Bi_{4-x}Nd_xTi_3O_{12}$ thin films, A. Hidalgo, M.S. Tomar, **R.E. Melgarejo**, and R.S. Katiyar. Integrated Ferroelectrics. *Volume 42 No. 1*; (2002).

Other Publications:

1. Synthesis and structural characterization of $BiFeO_3$-$BaTiO_3$ materials, **R.E. Melgarejo**, M.S. Tomar, R. Guzman, S.P. Singh. Integrated Ferroelectrics, (in press).

2. Structural and dielectric properties of $Ca_{1-x}Mg_xCu_3Ti_4O_{12}$ thin films, L.A. Bermúdez, R.P. Guzman, M.S. Tomar, **R.E. Melgarejo**, Mater. Res. Soc Symp. Proc., Vol 785 D6.7.1-D6.7.6 (2004).

3. Synthesis and characterization of $Ca_{1-x}Sr_xCu_3Ti_4O_{12}$ thin films for dielectric applications, R. Guzman, M.S. Tomar, **R.E. Melgarejo.** and R.S. Katiyar, Mater. Res. Soc Symp. Proc., Vol 785 D4.10.1-D4.10.6 (2004).

4. Sol-Gel derived $BiFeO_3$ thin films for bi-functional devices, **R.E. Melgarejo**, M.S. Tomar, R. Guzman and S.P. Singh, Physics of Semiconductor Devices, 1136-1138 (2003).

5. Aurivillius phase materials and ferroelectric devices, **R.E. Melgarejo**, A. Hidalgo, and M.S. Tomar, Physics of Semiconductor Devices, V. New Delhi, pp 1129-1132 (2001).

6. Growth and properties of $Sr_{1-x}Ba_xBi_2TaNbO_9$, materials and thin films, M.S. Tomar, **R.E. Melgarejo**, P.S. Dobal, M. Jain, and R.S Katiyar, J. Materials Science 36, 3919 (2001).

7. A novel route for the synthesis of $LiAl_xCo_{1-x}O_2$ battery materials and their structural properties, M.S. Tomar, A. Hidalgo, P.S. Dobal, A. Dixit, **R. E. Melgarejo**, and R. S. Katiyar, and K.A. Kuenhold, Proceedings of Materials Research Society, 658 (2001).

8. Preparation and characterization of Ba an Nd substituded $SrBi_2Ta_2O_9$ compounds, R.R. Das, P.S. Dobal, A. Dixit, W. Perez, M. S. Tomar**, R.E. Melgarejo**, and R. S. Katiyar, Proc Mater. Res. Soc. Symp. Proc. 655 (2001).

9. {1-x $SrBi_2Ta_2O_9$- xBi_3TiTaO_9} materials: structural behavior and ferroelectric response,**R.E. Melgarejo**, M. S. Tomar, P.S. Dobal, S. K Filippov, R. S. Katiyar, and K.A. Kuenhold, Mater. Sci. and Engineering (B) 83, 89 (2001).

10. Synthesis of $Zn_{1-x}Mg_xO$ and its structural characterization, M.S. Tomar, **R.E. Melgarejo**, P.S. Dobal, and R.S Katiyar. J. Mater. Res. 16, 903(2001).

11. Structural and electrical properties of $Sr_{1-x}Ba_xBi_2Ta_2O_9$ thin films, **R. E. Melgarejo**, M.S. Tomar, P.S. Dobal, and R.S. Katiyar, Thin Solid films 377-378 745 (2000).

12. Synthesis and characterization of $Sr_{1-x}Ba_xBi_2Ta_2O_9$ materials,**R.E. Melgarejo** , M.S. Tomar, P.S. Dobal, and R.S. Katiyar, J. Mater. Res. 15, 1661 (2000).

13. Synthesis and studies of $Ti_{1-x}Co_xO_2$ for device applications, M.S. Tomar, A. Hidalgo, **R.E. Melgarejo**, and R.S. Katiyar, Mater. Res Symp. Proc. Vol 690 F6.6.1-F6.6.4, (2002).

14. Structural properties and doping of $Zn_{1-x}(Li,Mg)_xO$ materials, **R.E. Melgarejo**, M.S. Tomar and R.S. Katiyar, Mater. Res. Soc Symp. Proc., Vol 692 H6.4.1-H6.4.6 (2002).

15. Structural characterization of $[(1-x)SrBi_2Nb_2O_9-(x)Bi_3TiNbO_9]$ for ferroelectric application, **R.E. Melgarejo**, M.S. Tomar, A. Hidalgo, and R.S. Katiyar. J. Ferroelectric Volume 269 No. 1; (2002).

Thesis Related Presentation:

1. Studies of $Bi_{4-x}Gd_xTi_3O_{12}$ Bifunctional Material, Maharaj S. Tomar, **Ricardo E. Melgarejo**, Raúl singhal, Luis M. Angelats and Ram S. Katiyar. Materials Research Society Meeting, Boston Nov 28-2 Dec (2005) (Oral).

2. Rare earth substituted $Bi_4Ti_3O_{12}$ films and ferroelectric devices, M.S. Tomar, **R.E. Melgarejo**, Ferroelectric and Dielectric Conf. New Dehli. Nov 23-25 (2004). (Oral)

3. Leakage Current and Ferroelectric Response of $Bi_{4-x}Nd_xTi_3O_{12}$ Thin Films, **R.E. Melgarejo**, M.S. Tomar, and R.S. Katiyar, Materials Research Society Meeting, Boston Nov 28-2 Dec (2004) (Poster).

4. Ferroelectric memory in La substituted $Bi_4Ti_3O_{12}$ thin films, **R.E. Melgarejo** and M.S. Tomar, Materials Research Society Meeting, Boston, Dec. 1-5 (2003) (Poster).

5. Ferroelectric Behavior of spin Coated $Bi_{4-x}La_xTi_3O_{12}$ Thin Films, M.S. Tomar, **R.E. Melgarejo**, A. Dixit, and R.S. Katiyar, 10th International Meeting on Ferroelectricity, Madrid, September 3-7, 2001. (poster).

Other conference Presentations:

1. Structural and magnetic behavior of $Zn_{1-x}Co_xFe_2O_4$ for potential application in spintronics, M.S. Tomar, R.P. Guzman, **R.E. Melgarejo**. Ferroelectric and Dielectric Conf. New Dehli. Nov 23-25 (2004).(oral)

2. Synthesis and magnetic properties of $Zn_{1-x}Co_xFe_2O_4$ for spintronics applications, M.S. tomar, R.P. Guzman, **R.E. Melgarejo**, S.P. Singh, Materials Research Society Meeting, Boston Nov 28-2 Dec (2004) (Poster).

3. Structural and dielectric properties of $Ca_{1-x}Mg_xCu_3Ti_4O_{12}$ thin films, L.A. Bermúdez, R.P. Guzman, M.S. Tomar, **R.E. Melgarejo.** Materials Research Society Meeting, Boston, Dec.1-5(2003) (Poster).

4. Synthesis and characterization of $Ca_{1-x}Sr_xCu_3Ti_4O_{12}$ thin films for dielectric applications, R. Guzman, M.S. Tomar, **R.E. Melgarejo** and R.S. Katiyar, Materials Research Society Meeting, Boston, Dec. 1-5 (2003) (Poster).

5. Structural characterization of [$1-xSrBi_2Nb_2O_9-xBi_3TiNbO_9$] ferroelectric applications, **R.E. Melgarejo**, M.S. Tomar, A. Hidalgo, S. K. Filippov, and R.S. Katiyar, 10th International Meeting on Ferroectricity, Madrid, Spain, Spt. 3-7, 2001(Poster).

6. Studies of $Ti_{1-x}Co_xO_2$ for spintronic devices, A. Hidalgo, M.S. Tomar, **R.E. Melgarejo**, R. S. Katiyar, Materials Research Society symposium, Boston, Nov 2001(Poster).

7. A novel route for the synthesis of $LiAl_xCo_{1-x}O_2$ battery materials and their structural properties, M.S. Tomar, A. Hidalgo, P.S. Dobal, A. Dixit, **R.E. Melgarejo**, and R. S. Katiyar, and K.A. Kuenhold, Materials Research Society Meeting, Boston, Nov. 27-Dec (2000) (Poster).

8. Ba and Nd substituted $SrBi_2Ta_2O_9$ compounds for ferroelectric application,R.R. Das, P.S. Dobal, A. Dixit, W. Perez, M.S.Tomar, **R.E. Melgarejo**, and R.S. Katiyar, Materials Research Society Meeting, Boston, Nov. 27-Dec 2, 2000 (Poster).

STUDIES OF STRUCTURAL ELECTRICAL AND FERROELECTRIC PROPERTIES OF RARE-EARTH SUBSTITUTED BISMUTH TITANATE FILMS

Dedicated to

Manuel and Erceliz

Ricardo Antonio and Irene Nicole

Beatriz, Maryzender and Nelly

Acknowledgements

I would like to thank my advisor Prof. M.S. Tomar for giving me the opportunity to work on this project. He gave me advice and direction while allowing me the freedom to develop the project according to my own vision. Without his advice and encouragement, I would never have finished this quickly. I would also like to thank Prof. R.S. Katiyar for acting as my co-advisor. He gave the motivation for the project and helped me considerably along the way. Thank to him for the opportunities and tremendous help, advises and for providing excellent facilities. I would like to thank Prof. Ishikawa for graciously agreeing to be members of my thesis committee.

I would also like to thank to Dr. Luis Fonseca who is also the coordinator of chemical physics program, for his help and support on the matters related to my graduate studies in the Chemical Physics Program.

My special thanks are to Dr. Srinivasan Bhaskar, who taught me the basics of sol-gel processing and his valuable experience in ferroelectrics and lab setting efforts that helped me in a long way completing this thesis. My sincere thank to Dr. P.S. Dobal, who taught me lots of aspects of Raman spectroscopy.

My special thanks to Dr. Antonio Martinez for providing excellent X-ray diffraction measurement facilities.

Thanks to some speclab members: Anju, Alex, Bhaskar, Juan, Kishore, Menka, Naba, Nora, Margarita, Pijush, Rasmi, Santander, Supreme, Dr.Yuri and William for

maintaining harmonius atmosphere in lab . William deserves my special thanks for giving valuable assistance in Raman espectroscopy.

Thanks to good friends: Arturo, Hulusi, Javier, Luis, Singh, Rahul, Osber, Janilet, Luz, Moira, Ivette, Michelle, Judith, Wanda, Sandra Troche, Aida, Lenska, Ligmar, Taima, Wilda, Yani, Mary, for sharing nice time.

I also wish to acknowledge very generous financial support of this work by the grants: National Science Foundation and DOE.

Finally, my sincere thanks to the EPSCoR and the Physics department staff at the University of Puerto Rico.

Chapter 1

Introduction to Electroceramics

1.1. Introduction

The field of electroceramics has emerged as one of the most exciting areas in materials science research. The electroceramics can be used as capacitors, ferroelectrics, piezoelectrics, pyroelectrics and dielectrics. Nowadays, the electrical properties of oxide-based electroceramics in thin film form have attracted tremendous attention to fully understand and utilize these materials for different applications. One of the properties that have gained large attention both for academic reason as well as industrial application is the dielectric nature of oxides which is used as capacitors. Dielectric materials form dipoles when they are polarized by an applied voltage. The polarization is, however, lost when the applied voltage is shut off. These materials are electrical insulators and are often used as capacitors or electrical insulators in electrical devices, *e.g.* SiO_2 as gate dielectric in metal-oxide-semiconductor (MOS) structures. For a dielectric material to be useful in applications higher applied voltage and low dielectric loss (not loosing energy as heat in an alternating electric field) are required.

Since the discovery of ferroelectricity in single crystal materials sodium potassium tartrate tetrahydrate (Rochelle Salt) in 1921 by Joseph Valasek and its subsequent extension into the realm of polycrystalline ceramics (e.g. barium titanate, $BaTiO_3$) during the early to mid-1940s, there has been a continuous succession of new oxide based electroceramics and their technological developments and can be directly credited to ferroelectricity[1] which is magnetic analogous to ferromagnetism of the

magnetic iron, but it has no connection with iron at all. Under the external pressure, several oxide based ferroelectrics can produce an electric voltage, referred as piezoelectricity. Such piezoelectric materials are used in pressure transducers.

1.2. Ferroelectric materials

Ferroelectric materials are characterized by properties such as high dielectric constant, high piezoelectric constants, relatively low dielectric loss and high electrical resistivity. For ordinary dielectric materials, the relationship between the applied electric field and the induced polarization is linear. However, for ferroelectric materials the behavior is more complicated and is represented by a hysteresis loop (figure 1.1.) and is generally defined by reversible spontaneous polarization in the absence of electric field[2,3]. The cause of the observed spontaneous polarization is non-centrosymmetric arrangement of ions in the unit cell, the center of positive charge of the crystal does not coincide with the center of the negative charge, which produces an electric dipole moment related to the unit cell. Adjacent unit cells are inclined to polarize in the same direction and form a region called a ferroelectric domain. Unit cell of typical ferroelectric material ABO_3 has perovskite crystal structure illustrated in Figure 1.2, where A, B ions occupy the corner and body-centered sites, respectively, and O (oxygen) occupy the face-centered site. Under an applied electrical field to the ferroelectric material, the B ion which has two thermodynamically stable positions inside oxygen octahedral is displaced relative to the oxygen ions upward or downward, depending on the polarity of the electric field. This displacement generates a dipole moment inside the oxygen octahedral, referred as

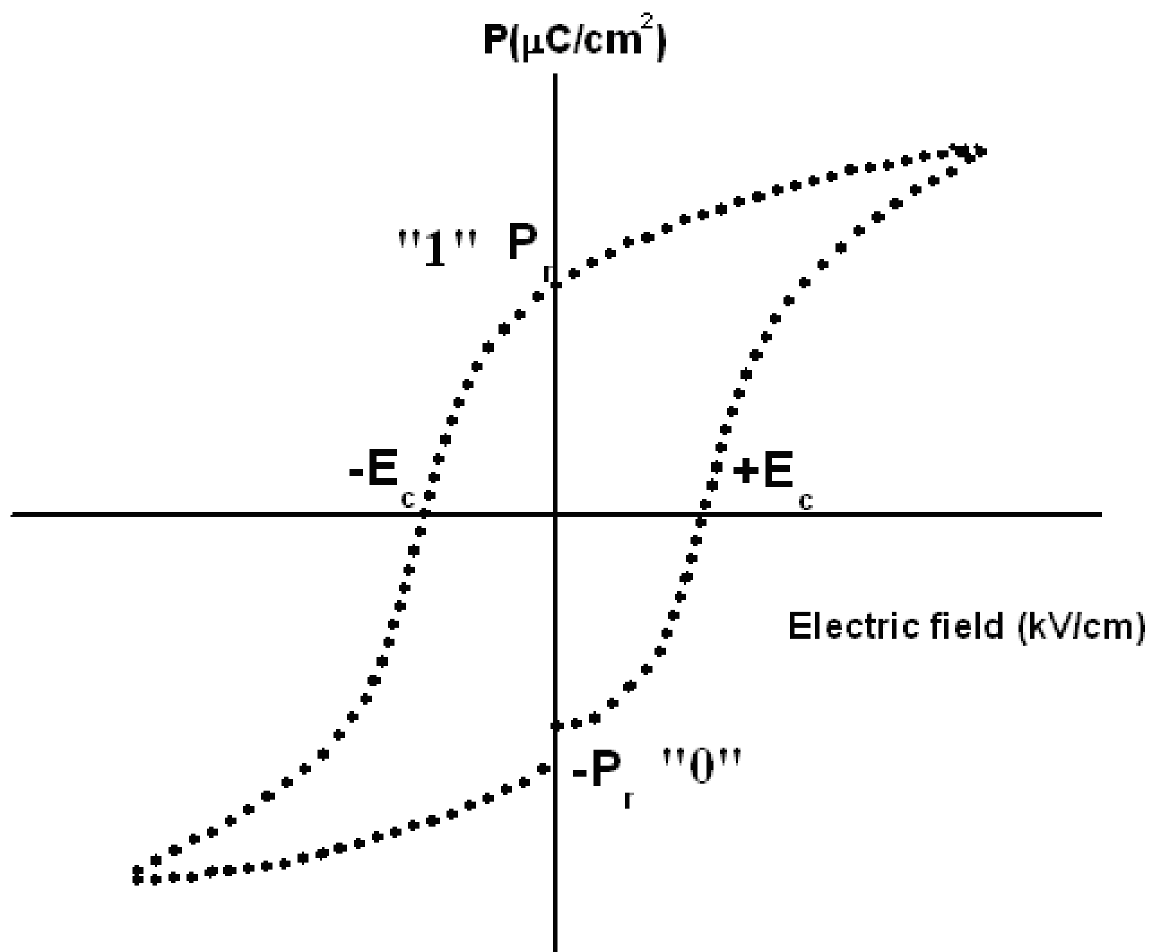

Figure 1.1. Hysteresis loop of a ferroelectric material

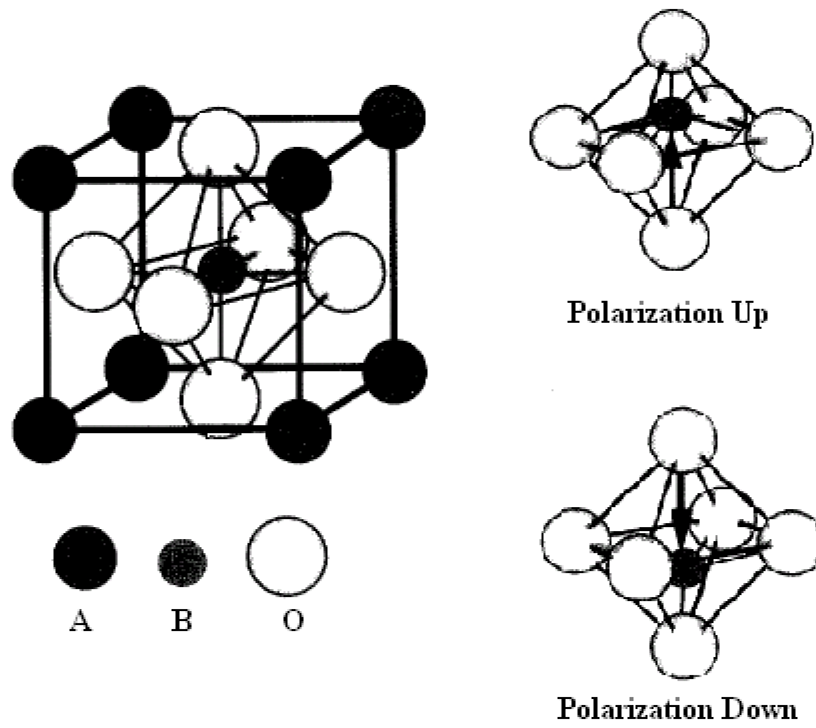

Figure 1.2. ABO_3 perovskite unit cell

saturated polarization ($\pm P_s$). When the applied electric field is removed, the B atom remains in the displaced position and generates a residual polarization in the absence of applied electric field, or remnant polarization ($\pm P_r$). In order to reverse the direction of polarization, we need to apply an electric field in reverse direction, the so called coercive electric field ($\pm E_c$), which is defined as a minimum electric field for switching the polarization. Therefore, the basic characteristics of a ferroelectric material that make it suitable for non-volatile memory applications are its ability to retain two stable remnant polarization (Pr) values at zero electric field providing nonvolatility. The state of polarization can be controlled and sensed by reversing the polarization from up (+1) to down (0) or vice versa as a function of applied voltage. Therefore, such a property can be used a non-volatile memory foe device applications.

Within the orientation of the polarization mechanism there are two subclasses of polarizibilities. They are the reversible polarization mechanism, which reverts back to its original unpolarized state after field removal, and the spontaneous polarization mechanisms that exhibit remnant polarization after removal of field. Materials, which possess reversible spontaneous polarization, belong to the class of ferroelectrics. Thus, ferroelectricity is a property of certain nonconducting crystals or dielectrics that exhibit spontaneous electric polarization that can be reversed in direction by an application of an appropriate electric field[2]. Number of dipole moment per unit volume **N**, dipole moment

μ= **qd**, charge **q**, distance between positive and negative charges **d**, volume **V** and surface area **A.**

$$P = \frac{N\mu}{V} = \frac{Nqd}{Ad} = \frac{Nq}{A} \quad \textbf{(1.1)}$$

The phenomenon of ferroelectricity can be explained using phenomenological theory based on Landau free energy considerations[3].

$$F(P) = F_0 \frac{1}{2}\alpha P^2 + \frac{1}{4}\beta P^4 + 1\frac{1}{6}\gamma P^6 \quad \textbf{(1.2)}$$

Where F is the free energuy of the system, P is polarization, α, β, and γ are the Landau coefficients. The Electric field E is

$$E = \frac{dF}{dP} = \alpha P + \beta P^3 + \gamma P^5 \quad \textbf{(1.3)}$$

Utilizing first two terms, one can get the expression for the polarization P as a function of electric field E, and is expressed by,

$$P(E) = -\frac{\alpha}{3\beta\left(\frac{E}{2\beta} + \sqrt{\frac{\alpha^3}{27\beta^3} + \frac{E^2}{4\beta^2}}\right)^{\frac{1}{3}}} + \left(\frac{E}{2\beta} + \sqrt{\frac{\alpha^3}{27\beta^3} + \frac{E^2}{4\beta^2}}\right)^{\frac{1}{3}} \quad \textbf{(1.4)}$$

The theoretical plot of P vs E in this expression can be represented in figure 1.3 which are hysterises curves for single crystal and polycrystalline materials, respectively.

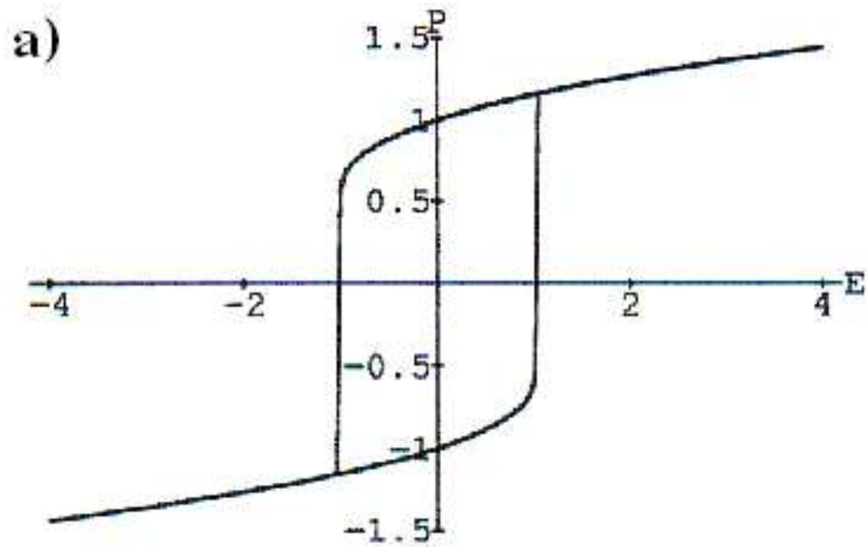

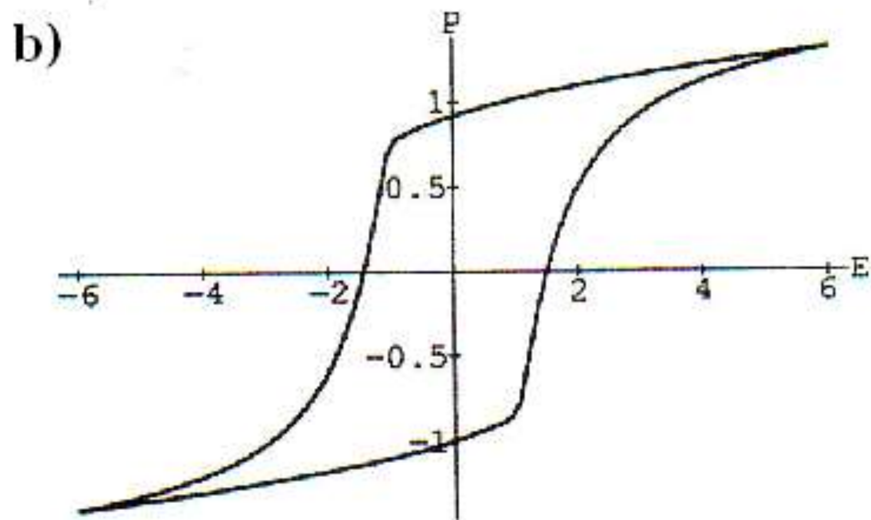

Figure 1.3 a) Hysteresis of a single ferroelectric crystallite b) Hysteresis loop for rhombohedral polycrystalline ferroelectric.

According to Neumann's principle, the symmetry of a crystal's internal structure is reflected in the symmetry of its external properties, and the lattice structure described by Bravis unit cell of the crystal governs the crystal symmetry. The symmetry of material whether it is a crystal, polycrystalline or amorphous thin films affects its properties. Ferroelectricity is caused by asymmetries in the lattice structure. A crystal is ferroelectric when it has two or more orientation of the states in the absence of an electric field and can be shifted from one state to another by an electric field. Any two of the orientation states are identical in crystal structure and differ only in electric polarization vector of null electric field. The spontaneous polarization is measured in terms of dipole moment per unit volume or with reference to the charge induced on surfaces perpendicular to the polarization in terms of charge per unit area. Though there are thousands of crystals in nature, they all can be grouped together into 230 microscopic types of space group based on symmetry elements. If only the orientation of the symmetry elements, are taken into account, the microscopic symmetry elements in crystals reduce to: (1) a center of symmetry, (2) mirror planes, (3) axes of rotation and (4) axis of inversion. All crystals can be divided into 32 different classes or point groups utilizing these symmetry elements, as shown in Table 1.1. These 32 point groups are subdivisions of seven basic crystal systems that are triclinic, monoclinic, orthorhombic, tetragonal, rhombohedral (trigonal), hexagonal, and cubic in the order of ascending symmetry. Of the 32 point groups, as shown in Figure 1.4, 21 classes are non-centrosymmetric (a necessary condition for piezoelectricity to exist) and 20 of these are piezoelectric. The lack of a center of symmetry is important for the presence of piezoelectricity. When one considers

a homogeneous stress as centrosymmetric and cannot produce an unsymmetric result, such as a vector-quantity-like polarization produces electric dipoles i.e. polarization. For those materials it is piezoelectric but no ferroelectric (i.e., they do not possess spontaneous polarization), the stress itself is the only means by which the dipoles are generated resulting piezoelectricity. For piezoelectricity, the effect is linear and reversible, and the magnitude of the polarization is dependent on the magnitude of the stress and the sign of the charge produced is dependent on the type of stress (tensile o compressive).There are 10 crystal classes out of a possible 20 that are designated as pyroelectric. This group of materials possesses the unusual characteristic of being permanently polarized within a given temperature range. Unlike the more general piezoelectric classes that produce a polarization under stress, the pyroelectrics develop this polarization spontaneously and form permanent dipoles in the structure. This polarization also changes with temperature –hence, the term pyroelectricity. Pyroelectric crystals, such as tourmaline and wurtzite, are polar materials, thus referring to the unique polar axis existing within the lattice. The total dipole moment varies with temperature, leading to a change in sign for the current flowing out of a short-circuited crystal.

Thus, the two conditions necessary in a material to classify it as a ferroelectric are:

(1) The existence of spontaneous polarization and

(2) A demonstrated reorienting of the polarization.

Four types of ceramic ferroelectrics are also given in figure 1.3 as subcategories of the general group of ferroelectric materials, with typical examples representing the type based on its unit cell structure:

(1) the tungsten-bronze group,

(2) the oxygen octahedral group,

(3) the pyrochlore group, and

(4) the bismuth layer-structured group.

The special relationship of ferroelectrics as a subgroup of piezoelectrics infers that ″all ferroelectrics are piezoelectric, but not all piezoelectrics are ferroelectric.″ Among the four categories, the fourth group $(Bi,M)_4Ti_3O_{12}$ (M = trivalent or rare earth ion) is of great, and there process-structural-property in context of ferroelectric behavior will be presented in details.

1.3. Ferroelectric Domains

The spontaneous polarization in a ferroelectric crystal (or a grain in a ferroelectric film or ceramic) is usually not uniformly aligned throughout the whole crystal along the same direction. The regions of the crystal with uniformly oriented spontaneous polarization are ferroelectric domains[4] and the region between two domains is called domain wall as shown in figure 1.5. Domain walls that separate different orientations of the spontaneous polarization vector may be referred as ferroelectric domains walls. Ferroelectric domains form to minimize the electrostatic energy of the depolarizing fields and the elastic energy associated with mechanical constraints to which

Table 1.1 Point groups for the seven crystal system

Crystal Structure	Point Groups	Centro Symmetry	Non-Centrosymmetry	
			Piezoelectric	Pyroelectric
Triclinic	1, $\underline{1}$	$\underline{1}$	1	1
Monoclinic	2, m, 2/m	2/m	2, m	2, m
Orthorhombic	222, mm2, mmm	mmm	222, mm2	mm2
Tetragonal	4, $\underline{4}$, 4/m, 422, 4mm, $\underline{4}$2m, (4/m)mm	4/m, (4/m)mm	4, $\underline{4}$, 422, 4mm, $\underline{4}$2m	4, 4mm
Trigonal	3, $\underline{3}$, 32, 3m, $\underline{3}$m	$\underline{3}$, $\underline{3}$m	3, 32, 3m	3, 3m
Hexagonal	6, $\underline{6}$, 6/m, 622, 6mm, $\underline{6}$m2, (6/m)mm	6/m, (6/m)mm	6, $\underline{6}$, 622, 6mm, $\underline{6}$m2	6, 6mm
Cubic	23, m3, $\underline{4}$32, 43m, m3m	m3, m3m	23, $\underline{4}$3m	None

underlined numbers represent inversion symmetry

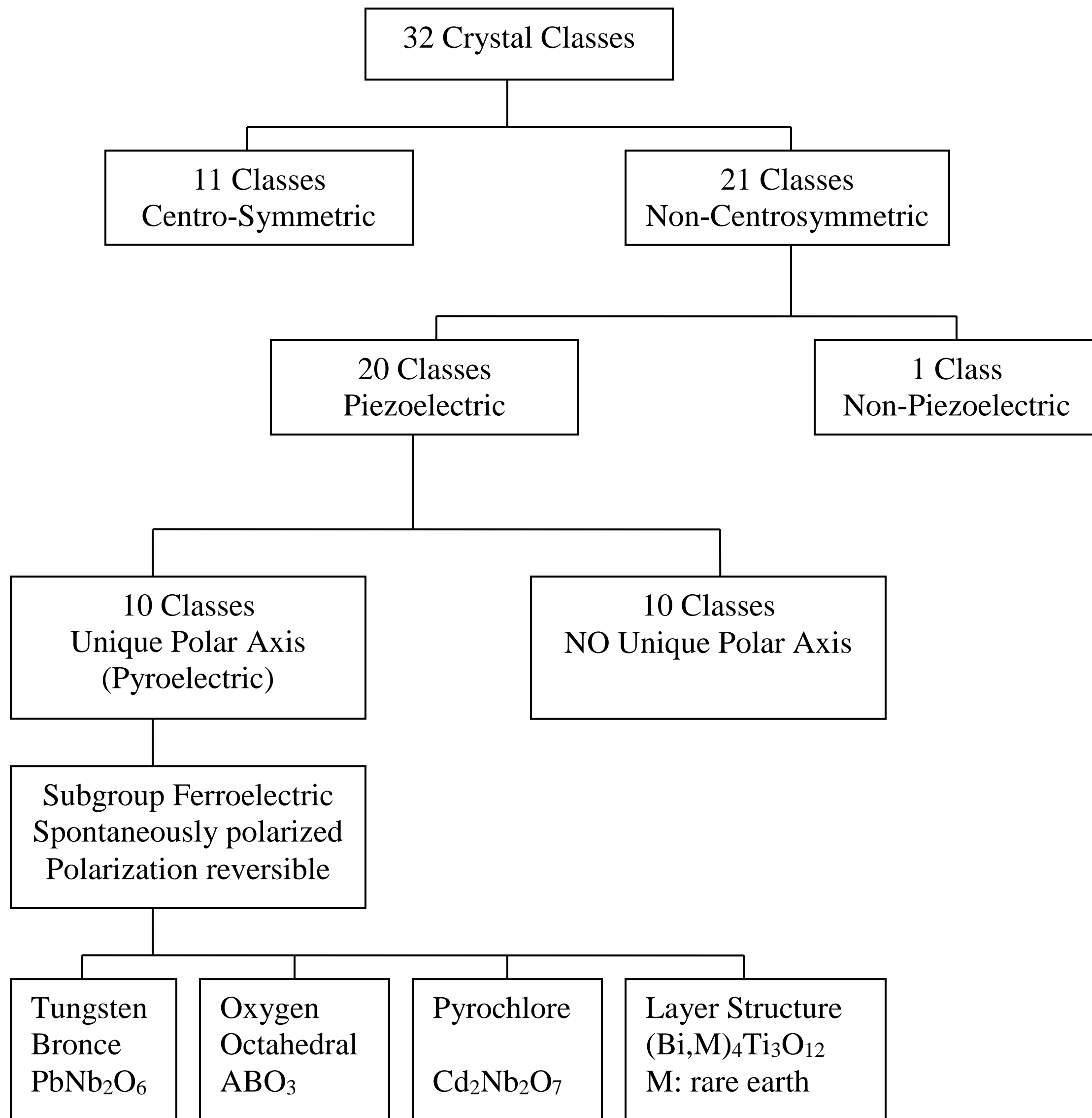

Figure 1.4 interrelationship of piezoelectric and subgroups on the basis of symmetry.

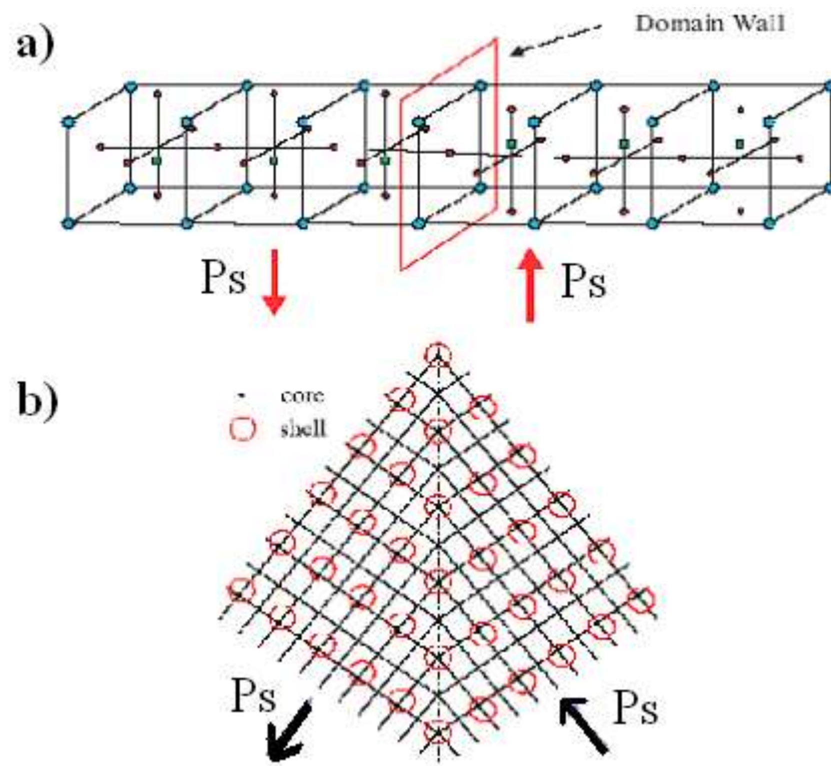

Figure 1.5 Illustration of (*a*) 180° and (*b*) 90° ferroelectric domains and domain-wall regions in a tetragonal perovskite ferroelectric.

the ferroelectric material is subjected during the transition from the paraelectric to the ferroelectric phase. Depolarizing fields develop whenever a non-homogeneous distribution of the spontaneous polarization appears, for instance, during the formation of the ferroelectric phase. Also, the fall-off of the polarization at a grain boundary usually causes strong depolarizing fields of the order of 10 kV/cm. Due to these high values, the depolarizing fields cause the single-domain state of a ferroelectric to be energetically unfavorable. As a consequence, the electrostatic energy associated is minimized by splitting the ferroelectric into domains with opposite polarization. Alternatively, the charges associated with the depolarizing fields may be neutralized by conduction of free charges through the crystal or coming from the surrounding of the material.

The domain structure that develops in single crystal perovskites (ABO_3) is well known. The spontaneous polarization can be oriented only along three mutually perpendicular crystallographic directions (in the tetragonal phase). This gives rise to two types of domain walls: walls that separate domains with oppositely oriented polarization (called 180°-walls), and those which separate regions with mutually perpendicular polarization (called 90°-walls). The 90°-walls are both ferroelectric and ferroelastic domain walls, because they separate regions with different orientation of the polarization and of the strain. Ferroelectric domain walls are much narrower than domain walls in ferromagnetic materials. Observations with transmission electron microscopy (TEM) show that domain walls in ferroelectric thin films are on the order of 1–10 nm.

The ferroelectric domain structure is the most important factor that determines the ferroelectric properties of a ferroelectric material, and splitting into domains at the formation of the ferroelectric phase it depends very much on the mechanical and electrical boundary conditions imposed on the sample, as well as on the nature of the sample itself.

1.4. Poling of ferroelectrics

Due to the complex set of elastic and electric boundary conditions at each grain, ferroelectric grains in ceramics and polycrystalline films are always split into many domains (figure 1.6). If the direction of the spontaneous polarization through the material is random or distributed in such a way as to lead to zero net polarization, the pyroelectric and piezoelectric effects of individual domains will cancel and such material is neither pyroelectric nor piezoelectric. Polycrystalline ferroelectric materials may be brought into a polar state by applying a strong electric field (10–100 kV cm^{-1}), usually at elevated temperatures. This process, called poling, cannot orient grains, but can reorient domains within individual grains in the direction of the field. A poled polycrystalline ferroelectric exhibits pyroelectric and piezoelectric properties, even if many domain walls are still present, figure 1.6. As grown ferroelectric single crystals usually contain many domains and may exhibit weak piezoelectric and pyroelectric properties. A single crystal that does not contain domains is said to be in a single-domain or monodomain state. The single-domain state in single crystals may be achieved by poling.

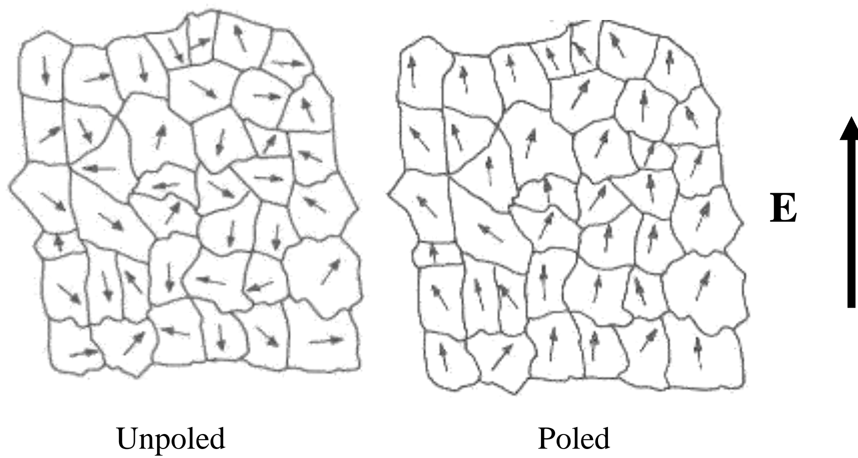

Figure 1.6 A polycrystalline ferroelectric with random orientation of grains before and after poling. Many domain walls are present in the poled material, however, the net remnant polarization is nonzero.

The poling, i.e. polarization reversal by a field is possible only in ferroelectric materials. A pyroelectric (non-ferroelectric) or piezoelectric polycrystalline material with randomly oriented grains cannot be poled and exhibit pyroelectric or piezoelectric properties. The polarization after the removal of the field (at zero field) is called remanent polarization, P_R. Maximum remnant polarization that may be achieved in a polycrystalline material depends on available domain states. In a ferroelectric which exhibits only 180° domain walls the maximum remnant polarization. $(P_R)_{max}$ in the polycrystalline state is $0.25P_S$. In a tetragonal ferroelectric with six available domain states, $(P_R)_{max} = 0.83\ P_S$. In an rhombohedral ferroelectric with eight possible domain states, $(P_R)_{max} = 0.87\ P_S$. In an orthorhombic ferroelectric with 12 possible domain states, $(P_R)_{max} = 0.91\ P_S$. These values are ideal assuming reorientation of all domains along available directions dictated by the poling field. The actual polarization is in fact always lower, as many domains cannot be reoriented due to a complex set of internal stresses and electric fields in grains and because some domains will switch back after the poling field is removed. If the symmetry of the ferroelectric is such so as to allow non-180° domain walls, the poling process will change the sample dimensions, because reorientation of non-180° domains involves reorientation of the spontaneous strain (see figure 1.6).

1.5 Ferroelectric hysteresis loop and polarization switching

One consequence of the domain-wall switching in ferroelectric materials is the occurrence of the ferroelectric hysteresis loop (figure 1.7). The hysteresis loop can be

observed experimentally by using a Sawyer–Tower circuit[5]. At small values of the AC electric field, the polarization increases linearly with the field amplitude. This corresponds to segment AB in figure 1.7. In this region, the field is not strong enough to switch domains with the unfavorable direction of polarization. As the field is increased the polarization of domains with an unfavorable direction of polarization will start to switch in the direction of the field, rapidly increasing the measured charge density (segment BC). The polarization response in this region is strongly nonlinear. Once all the domains are aligned (point C) the ferroelectricity again behaves linearly (segment CD). If the field strength starts to decrease, some domains will back-switch, but at zero field the polarization is nonzero (point E). To reach a zero polarization state the field must be reversed (point F). Further increase of the field in the negative direction will cause a new alignment of dipoles and saturation (point G). The field strength is then reduced to zero and reversed to complete the cycle. The value of polarization at zero field (point E) is called the remnant polarization, P_R. The field necessary to bring the polarization to zero is called the coercive field, E_C. The spontaneous polarization P_S is usually taken as the intercept of the polarization axis with the extrapolated linear segment CD, (in polycrystalline materials true spontaneous polarization equal to that of a single crystal can never be reached and it is saturated rather than of spontaneous polarization.) It should be mentioned that the coercive field E_C that is determined from the intercept of the hysteresis loop with the field axis is not an absolute threshold field. If a low electric field

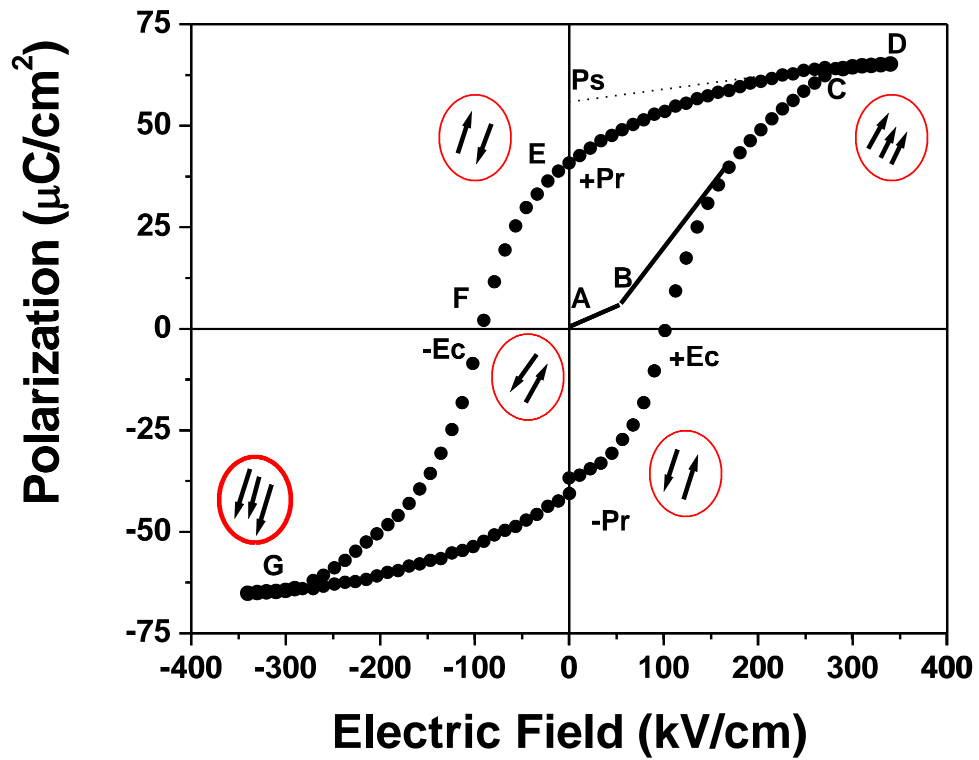

Figure 1.7 Ferroelectric (*P*–*E*) hysteresis loop. Circles with arrows represent the polarization state of the material at the indicated fields. The symbols are explained in the text.

is applied over a (very) long time period the polarization will eventually switch. An ideal hysteresis loop is symmetrical so that $+E_C = -E_C$ and $+P_R = -P_R$. The coercive field, spontaneous and remnant polarization and shape of the loop may be affected by many factors including the thickness of the film, the presence of charged defects, mechanical stresses, preparation conditions, and thermal treatment. The essential feature of a ferroelectric is thus not the fact that it has a spontaneous polarization, but rather the fact that this spontaneous polarization can be switched by means of an electric field. It may be noted that, owing to the relation between dielectric displacement D, electric field E, and polarization P,

$$D = E + 4\pi P \quad \textbf{(1.5)}$$

1.6. Ferroelectric memories

The fabrication of nonvolatile memory devices using ferroelectric materials was intensively studied between 1950's and 1970's by many market-leading companies such as IBM, RCA, Bell Laboratories and Westinghouse. Due to the incompatibility with the silicon process, the research was almost abandoned after 1975. However, since 1986, it has exploded as a result of the improvements in thin film technology, especially $Pb(Zr_xTi_{1-x})O_3$ (PZT) sol-gel and sputtering deposition techniques[6]. Ferroelectric memories in PZT have been investigated by many semiconductor memory industries as

well as by the defense industries, because of the nonvolatility, radiation hardness, high speed, low power, and compatibility with silicon process[7-10].

Nonvolatile memory is an essential part of all computer systems. It is especially important for specific use such as military systems where vital information has to be stored in some type of a nonvolatile memory that not loose information when power is lost in a hostile environment. Among the available nonvolatile memory technologies, disk memories offer large capacities, and are widely used in such items as personal computers. However, they are slow, bulky, and susceptible to breakdown because of their mechanical nature. Magnetic core and magnetoinducive plated wire memories are very limited in capacity, are very bulky, have large power requirements and are very expensive. Erasable programmable read-only memories (EPROM) and electrically erasable programmable read-only memory (EEPROM) have slower write speed, are susceptible to radiation damage, and fatigue faster than either core or silicon random access memories. Silicon oxide nitride oxide silicon (SONOS) memory is a type of nonvolatile memory option that is fast to read and can be radiation hard. However, SONOS is yet to be programmed for long retention (over five years) with programmable pulses of 1 μs or shorter. Another memory option currently is the magnetoresistive random access memory (MRAM), which has the potential to provide high density, radiation hardness, and nondestructive readout (NDRO) operation with unlimited endurance. Major disadvantages of this device are its slower read cycle time and larger cell design. Key characteristics of some of the current and future nonvolatile memory

technology are listed in Table 1.2. When one considers all the selection requirements for a nonvolatile memory, namely fast read/write, cost effectiveness, radiation hardness which is especially required for military and space applications, and compatibility with currently used integrated circuit (IC) processing technology, high endurance and retention, and nondestructive readout capability, the ferroelectric random access memory (FeRAM) stands out as the logical choice for all applications where submicro-second programming is needed[11]. In principle, FeRAM could replace EPROM, EEPROM. Furthermore, if high density FeRAM could be developed and the production cost could be reduced down to the level of magnetic core, the FeRAM could also replace the hard disk as the mass storage device, because of its faster access speed and the absence of mechanical wear problems. Actually, low density FeRAM, such as 4 k, 16 k, and 64 k FeRAM, have been manufactured by some semiconductor industries, such as Ramtron, Rohm, and Hitachi. Such a low density FeRAM is replacing EPROM and EEPROM in some areas, such as game machines and smart cards. Matzushita Electric Co in Osaka, Japan is the largest consumer-electronics firm for ferroelectric memories. Explosive demands in video games, cellular phones, portable computers and other portable electronic goods, indicate that annual sales of those speedy nonvolatile memories could amount to more than $20.7 billion by 2010[13].

Table 1.2. key characteristics of candidate nonvolatile memory technologies[12]

	FLOATIN GATE EEPROM	FLASH EEPROM	SNOS nvSDRAM (shadow)	MNOS EEPROM (SNOS)	SONOS EEPROM	DRO FeRAM	NDRO FeRAM	MRAM	CORE
SPEED (ACCES TIME)	150 nsec	120 nsec	35 nsec	150 nsec	150 nsec	100 nsec	200 nsec	Density Dependent 200 ns-2µs	350 nsec
WRITE TIME	10 msec byte/page	High	SRAM write 35 nsec; Download 11 msec	10 msec Byte	10 msec Byte	100-200 nsec	100-200 nsec	100-200 nsec	900 nsec
ENDURANCE	10^4-10^5	10^4 Write cycles	10^5 Power cycles	10^5 write cycles	10^6 write cycles	10^{10} Read/Write	10^{10} Write cycles	No known Limitations	No Limits
RADIATION HARDNESS	Low-Moderate	Low-Moderate	Moderate	High	High	High	None	High	Moderate High
LIMITATIONS	Write speed Endurance	Write speed Endurance	Density	Write speed	Write speed	None	Potentially Low to Moderate	Read speed, Density	Speed, Density Power
COST	Moderate	low	Moderate to High	Low	Moderate	Potentially Low to Moderate		Potentially Moderate	High

1.7 Phase transition by Raman spectroscopy

When light encounters molecules in the air, the predominant mode of scattering is elastic scattering, called Rayleigh scattering. This scattering is responsible for the blue color of the sky; it increases with the fourth power of the frequency and is more effective at short wavelengths. It is also possible for the incident photons to interact with the molecules in such a way that energy is either gained or lost so that the scattered photons are shifted in frequency. Such inelastic scattering is called Raman scattering. C.V. Raman discovered the inelastic scattering phenomenon in 1928, which bears his name and for it he was awarded the Nobel Prize for Physics in 1930.

Like Rayleigh scattering, the Raman scattering depends upon the polarizability of the molecules. For polarizable molecules, the incident photon energy can excite vibrational modes of the molecules, yielding scattered photons, which are diminished in energy by the amount of the vibrational transition energies. A spectral analysis of the scattered light under these circumstances will reveal spectral satellite lines below the Rayleigh scattering peak at the incident frequency. Such lines are called "Stokes lines". If there is significant excitation of vibrational excited states of the scattering molecules, then it is also possible to observe scattering at frequencies above the incident frequency as the vibrational energy is added to the incident photon energy. These lines, generally weaker, are called anti-Stokes lines.

In the optical frequency range, photon wave vectors are about 1000 times smaller than the shortest reciprocal lattice vectors. Thus, to very good approximation, elementary excitations with zero wave vectors, i.e., at the center of the Brillouin zone, are observed by Raman scattering. Most of the ferroelectrics are insulators. Their response to oscillatory external fields, whose frequencies are substantially lower than optical frequencies, is determined by the lattice vibration spectrum. The most striking feature of phonon spectra of ferroelectrics is the optical fluctuations with anomalously low and highly temperature dependent frequencies-the so-called soft modes. C.V Raman and T.M.K. Nedungati[14] showed the relationship between an unstable or 'soft' optical phonon and a structural phase transition in a crystal.

Twenty years later, the theory of soft mode phase transition was presented by W.Cochran[15]and the basic similarities between paraelectric; ferroelectric and antiferroelectric transitions were explained from a lattice dynamical point of view. Raman scattering, is primarily concerned with lattice dynamics and it has been proven valuable for the study of ferroelectric materials as ferroelectricity has close relationship with lattice dynamics[16]. If a phase transition occurs, the Raman selection rules, which ultimately depend on crystal and molecular symmetries, will also change and new spectral features, characteristics for the new lattice, will appear. The unstable temperature-dependent phonon is always Raman active in the low temperature phase[17]. Thus this method is of great help in elucidating crystal structures. To investigate the origin of structural phase transitions, a lattice dynamical soft-mode model was proposed[15]

by Cochran. According to this model the unstable normal mode (i.e., the soft mode) has a frequency, which decreases as each transition temperature is approached (from above or below) and is described by the relation:

$$\boldsymbol{\omega_s^2 = A\ (T\text{-}T_c)} \tag{1.6}$$

Where A is constant and T_c is one of the transition temperatures. This displacive model, in addition to explaining the sequence of phase transitions, was successful in other ways. For instance equation (1.3) along with the Lyddane-Sachs-Teller (LST) relation is,

$$\boldsymbol{\varepsilon(0) = \varepsilon_\infty\, \omega^2_{LO} / \omega^2_{TO}} \tag{1.7}$$

Which relates the high- [ε_∞] and low- [$\varepsilon(0)$] frequency dielectric constants to a particular optic mode's longitudinal (LO) and transverse (TO) frequencies, implies a divergence in ε (0) at T_c.

1.8. Research background

Bismuth titanate $Bi_4Ti_3O_{12}$ (or BTO) is interesting material currently because of its applications to ferroelectric memory devices. It belongs to the series of bismuth layer-structure oxides with the chemical formula $(Bi_2O_2)^{2+}$ $(A_{n-1}B_nO_{3n+1})^{2-}$ that have a monoclinic ferroelectric structure with a space group of B1a1[18] with a = 0.545 nm, b = 0.541 nm, and c = 3.283 nm at room temperature.[19] It was first synthesized and described by Aurivilllius.[20] In the above formula, A stands for a mono-, di-, or trivalent ion or a mixture of those; B represents Ti^{4+}, Nb^{5+}, or Ta^{5+}; and n = 2, 3, 4, etc. This material can

be described as a stacking of $Bi_2O_2^{2+}$ and $Bi_2Ti_3O_{10}^{2-}$ layers along the c axis (see fig.1.7)[21]. In the $Bi_2Ti_3O_{10}^{2-}$ units, Ti ions are coordinated by oxygen octahedral, which form linear chains, and Bi ions occupy the interstitials outside the TiO_6 octahedra. $Bi_2Ti_3O_{10}^{2-}$ unit has some similarity with the perovskite structure, and the height of the perovskite-type layer sandwiched between $Bi_2O_2^{2+}$ layers is equal to six Ti-O distances or to three ABO_3 perovskites units. Figure 1.7 shows the typical crystal structure of $Bi_4Ti_3O_{12}$. Compared to other ferroelectric materials [e.g., $Pb(Zr,Ti)O_3$], this compound has a high Curie temperature (T_c = 675°C) which makes it useful over a wide temperature range either for standard electronic elements (capacitors, piezoelectric transducers and sensors) or new ones, such as nonvolatile memories.[22,23]

With current complementary metal oxide semiconductor (CMOS) technology, the integration of ferroelectric random access memories (FeRAMs) can be achieved using thin films compatible with silicon process temperature. The ever increasing demands for nonvolatile memories have led to the search for a new material having a large spontaneous polarization P_s with fatigue-resistant characteristics for high-density memories and for the reliability of performances. Among many materials that exhibit ferroelectricity, only two families of perovskites are currently scrutinized for their use in nonvolatile memories: (1) PZT (lead zirconate titanate) based perovskites[24-28] and

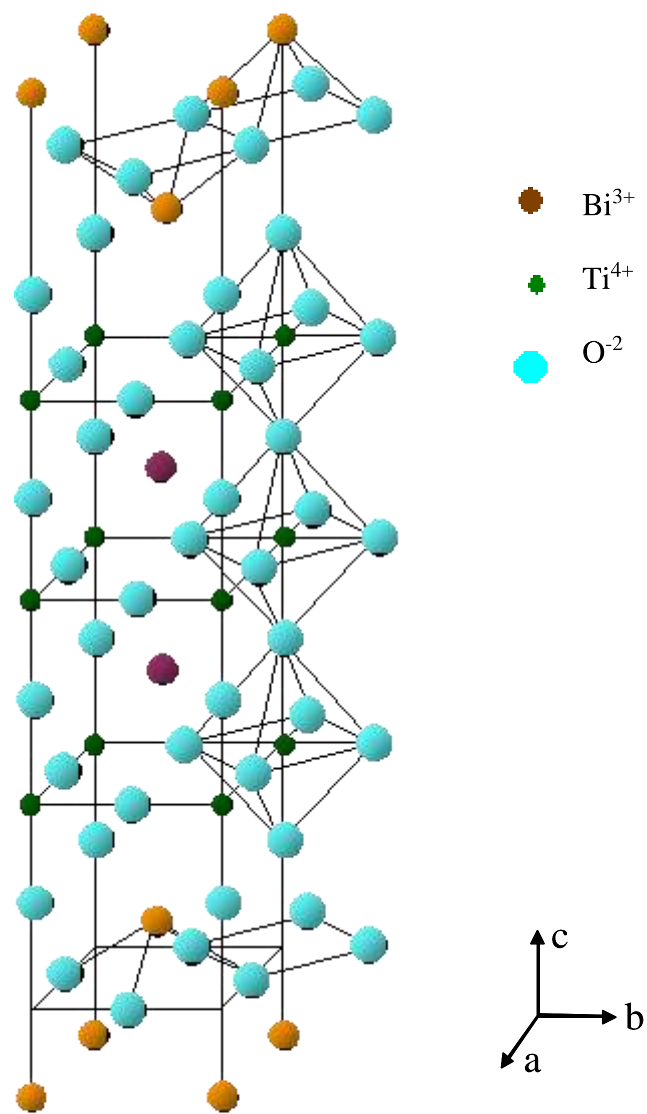

Figure 1.8. One half of unit cell of $Bi_4Ti_3O_{12}$

(2) layered perovskites such as strontium bismuth tantalate (SBT)[7] and lanthanum-modified bismuth titanate (BLT)[29,30].

PZT-based perovskites have been studied extensively and PZT films show large values of Pr, which vary from 20 to 70 μC/cm^2. But, a poor fatigue resistance makes them less attractive for direct commercialization using common Pt electrodes, the value of P_r is reduced after repetitive read/write cycles. This fatigue problem has been attributed to space charges resulting from defects inside the ferroelectric material. The fatigue resistance has been significantly improved by employing metal-oxide electrodes including RuO_2 and Ir/IrO_2[26,27]. However, they are electrically leaky, in general, and make the process more complicated. On the other hand, SBT show a superior fatigue resistance as compared to Pt/PZT/Pt capacitor structure, but suffers from its high-processing temperatures (~ 800° C) and very low switchable remnant polarization (2P_r) values, lead free ferroelectric materials are desired. Therefore, there has been an interest to investigate new type of materials for ferroelectric devices that are compatible with the current CMOS technology for integration.

$Bi_4Ti_3O_{12}$ (BTO) thin films have been fabricated by various deposition techniques such as rf magnetron sputtering, pulsed laser deposition, sol-gel processing, and metal organic chemical vapor deposition (MOCVD) techniques. In literature, since the major component of the spontaneous polarization of single crystal $Bi_4Ti_3O_{12}$ is directed along its *a* axis ($P_s^a \approx 50$ μC/cm^2) and the component along the *c* axis is very small ($P_s^c \approx 4$ μC/cm^2)[31-33], the growth of non-*c*-axis-oriented films is required to achieve a higher polarization component along the normal to the film plane. But due to strong anisotropic

characteristics, it is difficult to orient the films along the polarization *a*-axis. BTO films showed fatigue and unexpectedly low values of (P_{sw}-P_{ns}) = 4 - 8 μC/cm^2, and also has high transition temperature resulting in large switching fields. To reduce the voltage, it is desirable to reduce Tc.[34-36]

Recent studies[37-41] revealed that Bi^{3+} ions in $Bi_4Ti_3O_{12}$ (BTO) structure can be substituted by trivalent rare earth ions to improve their ferroelectric behavior. Park and coworkers modified $Bi_4Ti_3O_{12}$ using La substitution for Bi and forming a solid-solution of $Bi_{3.25}La_{0.75}Ti_3O_{12}$ (BLT). This material showed improved ferroelectric response in comparison with pure $Bi_4Ti_3O_{12}$. They proposed that lanthanum ions substituted for bismuth ions are located near the Ti-O octahedron layer and thereby enhanced the stability of the oxygen ions in the lattice (Fig. 1.9). Thin films of this composition can be deposited at lower temperatures than SBT or BTO, so that they can be integrated with the silicon CMOS technology more readily. Furthermore, BLT films showed higher remnant polarization than that of SBT or BTO, while at the same time displaying free fatigue polarization. Chon and coworkers[42] reported that, the direction and the magnitude of 2P*r* of highly *c*-axis oriented bismuth titanate (BTO)-based films were very susceptible to the substitution of trivalent rare-earth cations for bismuth. One important conclusion obtained from the refinement is that the major contribution to the development of P*s* along the *c*-axis comes from the TiO_6 octahedron unit adjacent to the interleaving Bi_2O_2 layer (Ti2 bottom or Ti2 top site) rather than from the TiO_6 unit of the inner central octahedron layer (Ti1 site) (fig. 1.10). Thus, one would expect to obtain BTO-based thin films having both fatigue-free characteristics and large P_s by suitably substituting

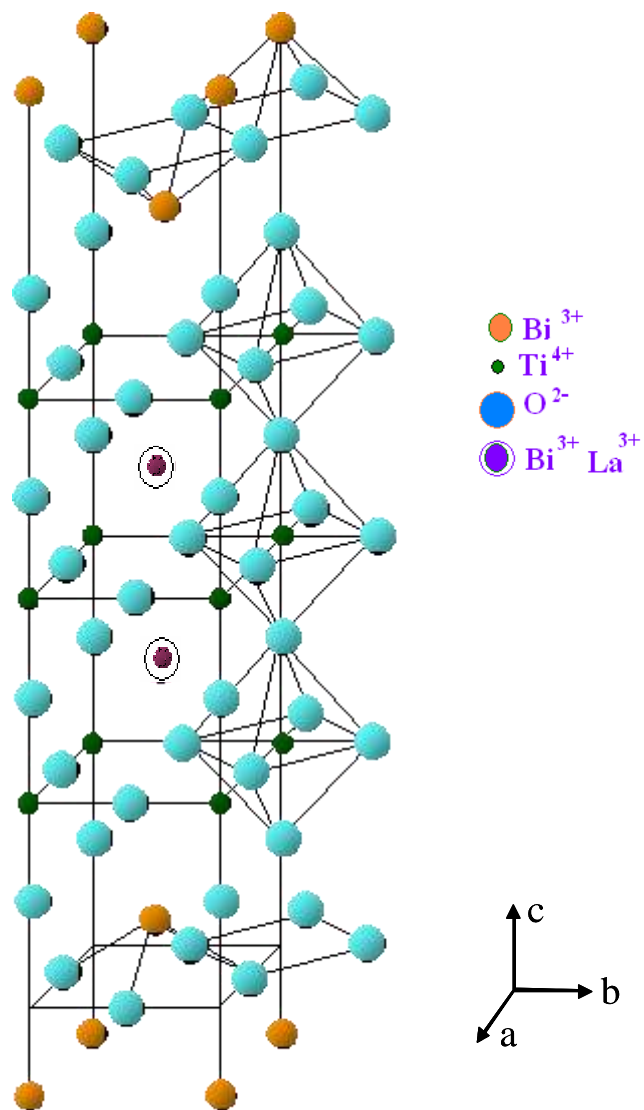

Figure 1.9 Structure of lanthanum substituted bismuth titanate

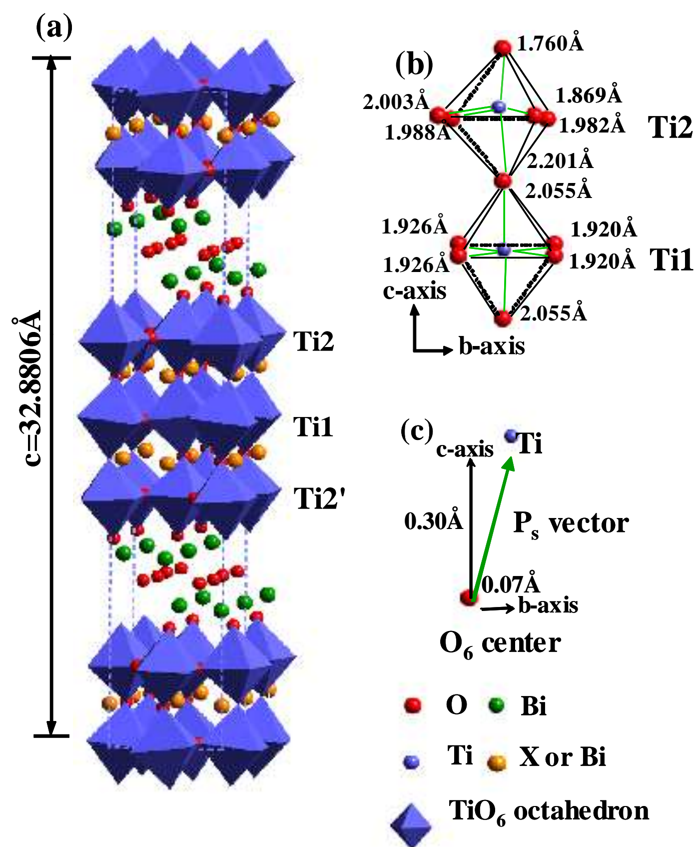

Figure 1.10 a) The refined unit-cell structure of BNdT at 298 k. b) the refined result of Ti1 and Ti2 sites projected on the *b-c* plane. c) The polarization vector of the Ti2 site projected on the *b-c* plane[42].

trivalent ions for volatile bismuth ions that tend to destabilize the oxygen ions located at the Ti-O octahedron layer. Among many rare-earth (Re) cations, La, Nd, Sm, Pr, and Gd meet the requirement of the ionic radius, the stable Curie temperature (> 400°C), and the phase stability of $(BiO)_2M_2Ti_3O_{10}$ –type layered perovskite[10]. For most, if not for all currently considered applications, the main interest is in polycrystalline ferroelectrics thin films, which are easier to make and which offer a larger variety of easily achievable compositional modifications than single crystals. Among many rare-earth (M) cations, La, Nd, Sm, Pr, and Gd meet the requirement of the would to obtain higher Pr value in rare-earth-cations-modified bismuth titanate by the contribution of both *a*-axis polarization and *c*-axis polarization component due to the difference of crystal orientation obtained in polycrystalline films[43].

1.9. Problem definition

Extensive efforts have been made for the realization of reliable high-density non-volatile ferroelectric random access memories (FeRAMs) using various deposition techniques. However, the reliability and performance of FeRAM devices is not satisfactory at present, and is limited by the following three causes:

a) Polarization fatigue

b) Imprinted polarization, and

c) Time-dependent charges loss of ferroelectric capacitors.

Lead free materials are preferred**.** The attempt to solve the above problems is to develop layered perovskite-based capacitors with large non-volatile charges and the reliability in

their performance. Preliminary study indicated that the direction and the magnitude of spontaneous polarization of preferred (117) orientation bismuth titanate-based films were susceptible to the substitution of trivalent rare-earth such as La, Nd, Sm and Gd for bismuth. With this motivation, the main objective of the present investigation is to develop highly (117) oriented rare-earth ions-modified titanate films by solution based techniques, such as sol-gel and solution deposition processes, and investigate their structural, electrical, ferroelectric, and fatigue response[43], in order to evaluate their potential in high-density non-volatile ferroelectric random access memories (FeRAMs).

1.10 References

1. Gene H. Haertling, J. Am. Ceram. Soc. **82**, 797(1999).
2. M. Lines and A. Glass, *Principles and Applications of Ferroelectrics and Related Devices*, (Clarendon Press, Oxford, 1977).
3. C. Brennan, Ferroelectrics **132**, 245 (1992)
4. Dragan Damjanovic, Rep. Prog. Phsys. **61**, 1267, 1998.
5. Sawyer C.B. Tower C. H. Phys. Rev. 35 269, 1930
6. K. D. Budd, S. K. Dey, and D. A. Payne, Brit Ceram. Soc. Proc., **36**, 107 (1985).
7. C. A. Araujo, J. D. Cuchiaro, L. D. McMillan, M. C. Scout, and J. F. Scott, Nature **374**, 627 (1995).
8. D. J. Jung, S. Y. Lee, B. J. Koo, Y. S. Hwang, D. W. Shin, J. W. Lee, Y. S. Chun, S. H. Sin, M. H. Lee, H. B. Park, S. I. Lee, K. Kim and J. G. Lee, VLSI Tech. Symp., 122 (1998).
9. S. Tanaka, R. Ogiwara, T. Miyakawa, Y. Takeuchi, S. Doumae, H. Takenawa and H. Kamata, IEDM Technical Digest, 359 (1998).

10. K. Amanuma, T. Tatsumi, Y. Maejima, S. Takehashi, H. Hada, H. Okizaki and T. Kunio, IEDM Technical Digest, 363 (1998).

11. S. Sinharoy, H. Buhay, D. R. Lampe, and M. H. Francombe, J. Vac. Sci. Technol, A, 10(4), p 1554, (1992).

12. Bob Peters, Defense Electronics, p. 82, (1991).

13. The Economist, Aug, 22nd, 63 (1998).

14. C.V. Raman and T.M.K.Nedungati, Nature, 144, 1940.

15. W. Cochran, Phys. Rev. Lett., 3, 412 (1959) ; Adv.Phys., 387, 1960.

16. P.S. Dobal and R.S. Katiyar, J. Raman Spectroscopy, 33, 405, 2002.

17. J.F.Scott and R.S.Katiyar, Indian J. Pure & Appl phy., 9, 950, 1971.

18. Min Ju Jeon, Yong-II Kim and Seong Ihl Woo, Proceedings of the International Symposium on Research Reactor and Neutron Science, (2005).

19. A. D. Rae, J. G. Thompson, R. L. Withers, and A. C. Willis, Acta Crystallogr., Sect. B: Struct. Sci. **46**, 474 (1990).

20. B. Aurivillius, Ark. Kemi **1**, 463(1949); **1**, (1949); **2**, 519 (1950).

21. E.C. Subbarao, Phys. Rev. **122**, 804 (1961).

22. A. Fouskova and L. E. Cross: J. Appl. Phys. **41** 2834 (1970).

23. T. Takenaka and K. Sakata: J. Appl. Phys. 55 1092 (1984).

24. O. Auciello, J. F. Scott, and R. Ramesh, Phys. Today **51**, No. 7, 22 (1998).

25. A. kingon, Nature (London) **401**, 658 (1999).

26. H. N. Al-Shareef, K.R. Bellur, A. I. Kingon, and O. Auciello, Appl. Phys. Lett. **66**, 239 (1995).

27. K. B. Lee, S. Tirumala, and S.B. Desu, Appl. Phys. Lett. **74**, 1484 (1999).

28. S. R. Shannigrahi and H. M. Jang, Appl. Phys. Lett. **79**, 1051 (2001).

29. B. H. Park et al, Nature (London) **401**, 682 (1999).

30. U. Chon, G.-C. Yi, and H. M. Jang, Appl. Phys. Lett. **78**, 658 (2001).

31. H. N. Lee and D. Hesse, Appl. Phys. Lett. **80**, 1040 (2002).

32. S. E. Cummins and L. E. Cross, J. Appl. Phys. **39**, 2268 (1968).

33. R. W. Wolfe and R.E. Newnham, J. Electrochem. Soc. **116**, 832 (1969).

34. P. C. Joshi and S.B. Krupanidhi, Appl. Phys. Lett. **62**, 1928 (1993)

35. T. Kijima, M. Ushikubo, Matsunaga, H. New. J. Appl. Phys. **38**, 127 (1999).

36. S. Y. Wu, W. J. Takei, M. H. Francamhe and S.E. Cummins, **3**, 217 (1972).

37. B. H. Park, B. S. Kang, S. D. Bu, T. W. Noh, J. Lee, and W. Jo, Nature (London) 401, 682(1999).

38. Y. Noguchi and M. Miyayama, Appl. Phys. Lett. 78, 1903 (2001).

39. T. Kojima, T. Sakai, T. Watanabe, H. Funakubo, K. Saito, and M. Osada, Appl. Phys. Lett. **80**, 2746 (2002).

40. H. Uchida, H. Yoshikawa, I. Okada, H. matsuda, T. Iijima, T. Watanabe, T. Kojima, and H. Funakubo, Appl. Phys. Lett. **81**, 2229 (2002).

41. T. Hyashi, N. Iizawa, D. Togawa, M. Yamada, W. Sakamoto, and S. Hirano, Jpn. J. Appl. Phys. (in press).

42. U. Chon, H. M. Jang, M. G. Kim, and C. H. Chang, Phys. Rev. Lett. **89**, 87601-1 (2002).

43. R.E. Melgarejo and M.S. Tomar, Mat. Resr. Soc. Symp. Proc. **784**, 219 (2004).

Chapter 2

Experimental techniques

2.1. Introduction

Present chapter is devoted to the preparation and characterization of $Bi_{4-x}Re_xTi_4O_{12}$ (Re = La, Nd, Sm and Gd) thin films of several compositions. Material was synthesized by sol-gel technique and thin films were deposited by spin coating on Pt substrate ($Pt/TiO_2/SiO_2/Si$). Description of various characterization techniques will be discussed.

2.2. Preparation techniques

The fabrication of oxide ferroelectric thin films is done by three main methods including physical vapor deposition (PVD), chemical vapor deposition (CVD) and chemical solution deposition (CSD). Because these techniques have different inherent advantages and disadvantages, the technique of choice will be dictated by property requirements, as well as by issue of cost, uniformity, and manufacturability. In PVD, the targets of the desired film composition are utilized and deposited on the substrate by techniques such as rf, dc magnetron sputtering, pulsed laser deposition (PLD) etc. The objective of these deposition processes is to controlled transfer atoms from a source to a substrate where film formation and growth proceed. In evaporation, atoms are removed from the source by thermal means, whereas in sputtering they are dislodged from solid target (source) surfaces through impact of gaseous ions. The CVD technique uses volatile chemical precursors in the gaseous forms, which are then deposited on the heated substrates. The advantages of this technique include high deposition rates, pinhole free

films and good stoichiometric control. On the other hand chemical solution deposition (CSD) is a popular technique for making new oxide based materials for several electronic devices[1,2]. In our case CSD techniques are preferred because they offer a relatively simple low cost approach at relatively low temperatures to fabricating thin films that permit excellent compositional and orientational control, which is critical for stoichiometric and multicomponent oxide systems, that is compatible with commercial processing equipment and techniques such as spin coating and photolithography. In the present study sol-gel was used to prepared thin films.

2.2.1. Sol-gel technique

Today, sol-gel thin film coatings are used extensively for such diverse applications as protective and optical coatings, passivation and planarization layers, sensors, high or low dielectric constant films, inorganic membranes, electro-optic and nonlinear optical films, electrochromics, semiconducting anti-static coatings, oxide superconducting films, strengthening layers, and ferroelectrics[3].

The sol-gel technique offers a low-temperature method for synthesizing materials that are either totally inorganic in nature or both inorganic and organic. The process, which is based on the hydrolysis and condensation reaction of organometallic compounds in alcoholic solutions, offers many advantages for the fabrication of coatings, including excellent control of the stoichiometry of precursor solutions, ease of compositional modifications, customizable microstructure, ease of introducing various functional groups

or encapsulating sensing elements, relatively low annealing temperatures, the possibility of coating deposition on large-area substrates, and simple and inexpensive equipment.

Sol-gel processing is a wet chemical route for the synthesis of a colloidal suspension of solid particles or cluster in a liquid (sol) and subsequently for the formation of a dual phase material of a solid skeleton filled with a solvent (wet gel) though sol-gel transition (gelation). The first step of the sol-gel process included the selection of the precursors of the desired materials. The most important reagent (precursor) in the sol-gel process is a hydrolysable organometallic, called metal-alkoxide. The general formula for a metal-alkoxide is $M(OR)_n$, where the metal atom M with valence n is bonded to alkoxy group (OR). An alkoxy group contains an alkyl group (R) such as methyl (CH_3), ethyl (C_2H_5) etc. The precursor, by its chemistry, lead to the reactions towards the formation of either colloidal particles, or polymeric *gels*. The colloidal particles obtained can be precipitated and treating accordingly (cold/hot pressing and sintering) to produce desired ceramic.

2.2.2. Sol-gel chemistry

In the preparation of ferroelectric thin films by solution deposition there are three categories:

(1) sol-gel process that uses 2-methoxyethanol as a reactant and solvent,

(2) hybrid process using chelating agent such as acetic acid, or diethanolamine to reduce alkoxide reactivity, and

(3) metalorganic decomposition (MOD) approach that uses large, water-insensitive carboxylate compounds[4,5]

The three classes of solution preparation approaches have in common the synthesis of a precursor solution that is used to deposit an amorphous thin film, which is subsequently crystallized into the desired phase by the heat treatment.

2.2.2.1. 2-Methoxyethanol Solution synthesis

The 2-methoxyethanol process is considered a sol-gel process since alkoxide starting reagents are used and the key reaction leading to the formation of the precursor species are hydrolysis and condensation, where metal-oxygen-metal (M-O-M) bonds are formed as follows:

$$M(OR)_n + H_2O \rightarrow M(OR)_{n-1}(OH) + ROH \quad \text{(hydrolysis)} \qquad (2.1)$$

$$2M(OR)_{n-1}(OH) \rightarrow M_2O\,(OR)_{2n-2} + H_2O \quad \text{(condensation)} \qquad (2.2)$$

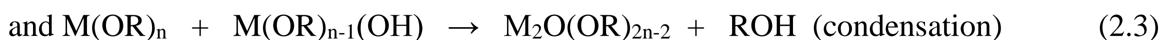

$$\text{and } M(OR)_n + M(OR)_{n-1}(OH) \rightarrow M_2O(OR)_{2n-2} + ROH \quad \text{(condensation)} \qquad (2.3)$$

2.2.2.2. Hybrid Solution synthesis

This second process, which are ‘hybrid’ or ‘chelate’ routes, also utilize alkoxide compounds as starting reagents but modify the nature of those compound through reactions with other reagents. Although these deposition processes initiate molecular modification of the alkoxides by using chelating agents such as acetic acid, acetylacetone, or diethanolamine, the processes still share common attributes with methoxyethanol-

based deposition utilizing similar starting reagents and oligomeric species are again formed during the solutions synthesis. The most commonly used hybrid processes are based on the solvent-chelating agent acetic acid.

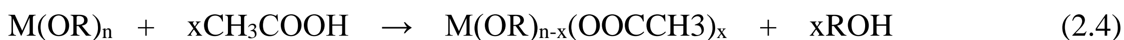

$$M(OR)_n + xCH_3COOH \rightarrow M(OR)_{n-x}(OOCCH3)_x + xROH \qquad (2.4)$$

Since chelation results in molecular modification of the alkoxide compounds, chelating reagents also dictate the structure and properties of the resulting species. Such substitute groups, i.e. acetate or nitrate (from acetic acid) or acetylacetone, serve to reduce susceptibility of the starting reagents to hydrolysis and condensation. Compared to the 2-methoxyethanol processes, the hybrid processes offer the advantage of relatively simple solution synthesis. Involved distillation and refluxing strategies are not required. However, while process is simple and rapid, the chemistry involved in solution preparation is quite complex due to a number of side reactions that occur. This results in a diminished ability to control precursor structure and properties.

2.2.2.3. Metalorganic-Deposition Solution Synthesis

The third deposition approach. MOD use large carboxylate or β-diketonate (acac-type) compounds, such as, lead 2-ethylhexanoate, neodecanoate, and titanium di-methoxy di-neodecanoate. This process is different from 2-methoxyethanol and hybrid processes. The basic approach consists of simply dissolving the metal-organic compounds in a common solvent, usually xylene, and combining the solutions to yield the desired stoichiometry.

While the process is straightforward, it does posses a number of limitations. The large organic ligands, of the most commonly used starting reagents may cause cracking during the thin-film processing. To solve this difficulty, proper control of solution concentration and thermal processing is required.

2.3. Film Deposition and Heat Treatment

Several methods can be used to make sol-gel films with the sol-gel process. Spin coating and dip coating are two basic techniques used to deposit sol-gel coatings. Spin coating produces a one-sided coating, while dip coating yields a double-sided coating. Both techniques are used in manufacturing different coatings and thin films. In this work all films were prepared by spin coating method. This is usually achieved by depositing a few drops of the solution onto a clean substrate using a syringe with a 0.2 μm filter while spinning the substrate around 3000 rpm. The as-deposited film is amorphous and can retain a significant organic fraction. Its nature at this stage is highly dependent on the size and reactivity of the solution precursor species.

After deposition is immediately followed by pyrolysis. Then each layer is crystallized before the next deposition. General flow chart of the sol-gel process for BLaT is given in figure 2.1. In the single-step process, the film is usually heated rapidly to the crystallization temperature, which results in both organic pyrolysis and crystallization. Typical examples of the sol-gel calculation are presented for the La substitution Bismuth titanate thin films using acetic acid modified route. The mixing and weighing of the samples were carried under at air atmosphere.

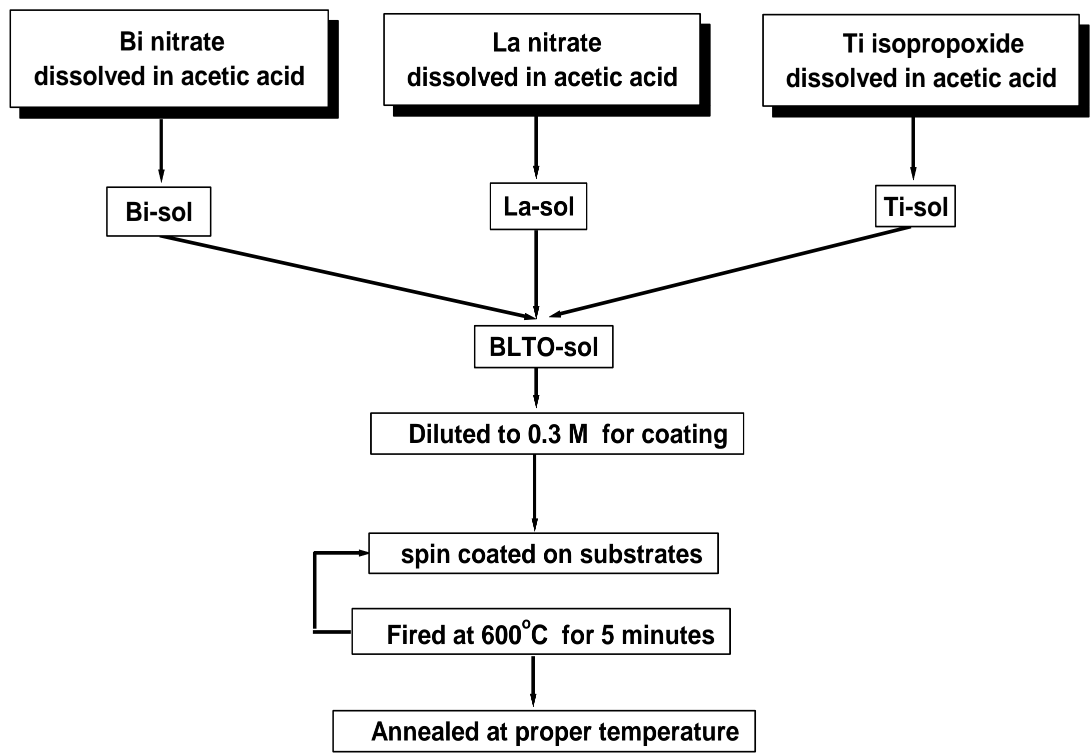

Figure 2.1 Flow chart of the sol-gel process of $Bi_{4-x}La_xTi_3O_{12}$ (BLaT) sol and thin film preparation.

2.3.1. Preparing of lanthanum (La) substituted $Bi_4Ti_3O_{12}$ films.

Parent sol of $Bi_{4-x}La_xTi_3O_{12}$ (BLaT) was prepared as describe above. List of precursor materials are listed in table 2.1. The coating sol of 0.30 M was spin coated on the cleaned Pt/Si (i.e. $Pt/TiO_x/SiO_2/Si$) substrates using multilayer approach. Film was coated number of times as required. After the deposition of each coating, the films are kept in a preheated furnace at 600° C for 5 minutes, for removal of organics and crystallization. In this way, each coating is crystallized before the deposition of next coating. After the final coating BLaT were annealed at different temperatures. The annealing condition used in the different studies will be described in the respective chapters.

Table 2.1. Precursors used for preparation the $Bi_{4-x}La_xTi_3O_{12}$ sol synthesis.

Chemical	**Molecular wt. (gms)**	**Yield (%)**	**Company**
Bismuth nitrate pentahydrate	485.07	98	Aldrich
Lanthanum nitrate hexahydrate	433.02	99.9	Aldrich
Titanium isopropoxide	284.26	99.999	Alfa Aesar

5% excess bismuth.

Chemical Formula: BLT for $Bi_{4-x}La_xTi_3O_{12}$; and BLaT-56 for $Bi_{3.44}La_{0.56}Ti_3O_{12}$

1) ***Bismuth nitrate pentahydrate***

0.001 * 3.49 * 485.07 * 100/98 = 1.727 gms

Acetic acid solvent = 2.50 gms

2) *Lanthanum nitrate hexahydrate*

0.001 * 0.56 * 433.02* 100/99.9 = 0.243 gms

Acetic acid solvent = 1.00 gms

3) *Ti(IV)-isopropoxide*

0.001 * 3.00 * 284.26 * 100/99.999 = 0.853 gms

Acetic acid solvent = 1.2 gms

The three solutions were mixed together at room temperature to get the final sol named as Parental sol. The parent sol was diluted to a concentration of 0.3 ML^{-1} with the addition of acetic acid and then used for spin coating. Further calculations are given below:

Volume of the parent sol: 18.6 ml

Strength of the parent sol: 0.01/18.6 = 0.537 M/L

Coating sol:

V_1 Known volume of parent sol: 5ml (usually)

N_1 Known strength of parent sol: 0.537 M/L

N_2 Required strength of Coating sol: 0.3M/L (as per requirements)

V_2 Required volume of Coating sol: = $V_1 X N_1 / N_2$ = 5* 0.537/0.3 = 8.95 ml

∴ Volume of solvent (acetic acid) to be added for dilution: 8.95 –5.00 = 3.95 ml

The parent sol was coated on Pt/Si substrates by multilayer spin coating approach. Films were coated at 300 rpm for 10 seconds for the deposition of each layer. Each individual layer is about 100 nm thick yielding a total film thickness of about 500 nm. Finally, the films were annealed at 700° C for 1h in air followed by the normal furnace cooling down to room temperature.

2.3.2. Preparing of neodymium (Nd) substituted BTO films.

To prepare Nd substituted BTO sol, stoichiometric amount of neodymium nitrate hexahydrate, bismuth nitrate pentahydrate and titanium isopropoxide dissolved in acetic acid. The neodymium solution, bismuth solution and titanium solution were mixed at room temperature. The precursor sol thus prepared is termed as parent sol. List of precursor materials are listed in table 2.2.

Table 2.2. Precursors used for preparation of $Bi_{4-x}Nd_xTi_3O_{12}$ (BNdT) sol synthesis

Chemical	Molecular wt. (gms)	Yield (%)	Company
Bismuth nitrate pentahydrate	485.07	98	Aldrich
Neodymium nitrate hexahydrate	438.35	99.9	Aldrich
Titanium isopropoxide	284.26	99.999	Alfa Aesar

5% excess bismuth.

Chemical Formula: $Bi_{4-x}Nd_xTi_3O_{12}$; For BNdT56: $Bi_{3.44}Nd_{0.56}Ti_3O_{12}$

1) ***Bismuth nitrate pentahydrate***

0.001 * 3.49 * 485.07 * 100/98	**=**	**1.727 gms**
Acetic acid solvent	**=**	**2.50 gms**

2) ***Neodymium nitrate hexahydrate***

0.001 * 0.56 * 438.35* 100/99.9	**=**	**0.246 gms**
Acetic acid solvent	**=**	**1.00 gms**

3) ***Ti(IV)-isopropoxide***

0.001 * 3.00 * 284.26 * 100/99.999	**=**	**0.853 gms**
Acetic acid solvent	**=**	**1.2 gms**

After mixing them in proper conditions, parent sol is obtained. It is then diluted to required strength (0.30 M) to get the solution for spin coating.

The coating sol was spun coated on cleaned platinized silicon (Pt/Si) substrates at 3000 rpm for 10s. Just after deposition the films were fired at 600°C for 5 min. for organic removal and crystallization into the Aurivillius phase. The coating and firing sequences was repeated several times to attain a film thickness of about 450nm. After the final coating, the films were annealed at 700°C for complete Aurivillius phase formation and better crystallinity.

2.3.3. Preparing of Samarium (Sm) substituted BTO films.

To prepare parent sol of Sm substituted BTO, samarium nitrate hexahydrate, bismuth nitrate pentahydrate and titanium isopropoxide were used as precursors. Acetic

acid was selected as the solvent. The samarium solution, bismuth solution and titanium solution were prepared separately. List of precursor materials are listed in table 2.3

Table 2.3. Precursors used for preparation of $Bi_{4-x}Sm_xTi_3O_{12}$ sol synthesis

Chemical	Molecular wt. (gms)	Yield (%)	Company
Bismuth nitrate pentahydrate	485.07	98	Aldrich
Samarium nitrate hexahydrate	444.47	99.9	Aldrich
Titanium isopropoxide	284.26	99.999	Alfa Aesar

5% excess bismuth.

Chemical Formula: BSmT for $Bi_{4-x}Sm_xTi_3O_{12}$; and BSmT70 for $Bi_{3.30}Sm_{0.70}Ti_3O_{12}$

1) *Bismuth nitrate pentahydrate*

0.001 * 3.35* 485.07 * 100/98 = 1.658 gms

Acetic acid solvent = 2.80 gms

2) *Samarium nitrate hexahydrate*

0.001 * 0.70 * 444.47* 100/99.9 = 0.31 gms

Acetic acid solvent = 1.00 gms

3) *Ti(IV)-isopropoxide*

0.001 * 3.00 * 284.26 * 100/99.999 = 0.853 gms

Acetic acid solvent = 1.2 gms

These three solutions were mixed together to obtain a transparent solution. The precursor sol thus prepared is termed as parent sol. 0.30M was prepared to get the solution for spin coating.

The coating sol was spun coated on to $Pt/TiO_x/SiO_2/Si$ substrates using a spin coater at a speed of 3000 rpm for 10s. After each coating the films were fired at 600°C for 10 min. for organic removal and crystallization into the Aurivillius phase. Seven layers were coated to achieve a final thickness of about 400 nm. Post deposition annealing of the films was carried out in a conventional furnace 700°C in an oxygen atmosphere for one hour for complete Aurivillius phase formation and better crystallinity.

2.3.4. Preparing of Gadolinium (Gd) substituted BTO films.

Bismuth nitrate pentahydrate, Gadolinium nitrate hexahydrate and titanium isopropoxide were used as precursors for Bi, Gd and Ti and acid acetic was solvent. The gadolinium solution, bismuth solution and titanium solution were prepared separately. List of precursor materials are listed in table 2.4

Table 2.4. Precursors used for preparation of $Bi_{4-x}Gd_xTi_3O_{12}$ (BGdT) sol synthesis.

Chemical	Molecular wt. (gms)	Yield (%)	Company
Bismuth nitrate pentahydrate	485.07	98	Aldrich
Gadolinium nitrate hexahydrate	433.34	99.9	Aldrich
Titanium isopropoxide	284.26	99.999	Alfa Aesar

5% excess bismuth.

Chemical Formula: BGdT for $Bi_{4-x}Gd_xTi_3O_{12}$; BGdT30 for $Bi_{3.70}Gd_{0.30}Ti_3O_{12}$

1) ***Bismuth nitrate pentahydrate***

0.001 * 3.75* 485.07 * 100/98	=	**1.658 gms**
Acetic acid solvent	=	**2.80 gms**

2) ***Gadolinium nitrate hexahydrate***

0.001 * 0.30 * 433.34* 100/99.9	=	**0.13 gms**
Acetic acid solvent	=	**1.00 gms**

3) ***Ti(IV)-isopropoxide***

0.001 * 3.00 * 284.26 * 100/99.999	=	**0.853 gms**
Acetic acid solvent	=	**1.2 gms**

A transparent multicomponent solution was prepared by mixing these three solutions. The concentration of BGdT expected in the final solution was adjusted to 0.30 M to get the solution for spin coating.

In the first step of preparing the films, the $Pt/TiO_x/SiO_2/Si$ substrates were spin coated with the prepared solution at a speed of 3000 rpm for 10s. The wet film was fired at 600° C for 5 min. for organic removal and crystallization into the Aurivillius phase. The first step were repeated several times for each film to obtain the desired film thickness. For complete crystallization, the BGdT thin films were finally annealed at 700° C in an oxygen atmosphere for one hour.

2.4. Characterization techniques

2.4.1. Films thickness measurements

In this work the films thickness was measurement using Filmetrics F20 (Filmmetrics Inc. CA) system[4]. The filmetrics system illuminates a sample with a tungsten-halogen white light source from 400nm to 3000nm with an effective measurement range from 400nm to 850nm. This supplied via a fiber optic cable from the light source output port. The light reflected by the sample is then captured and fed back to the Filmetric unit via another cable to the spectrometer input port. The reflectivity spectrum of the sample is compared to an internal mathematical reflectivity spectrum for the given sample. A calculated curve is then fitted to the measured curve and the corresponding thickness of the calculated model is reported.

The reflected light will have a certain wavelength and amplitude depending on the properties of the material. These properties are n and k, where n and ka are the film's refractive index and extinction coefficient, respectively. The accuracy of this system is usually limited by the accuracy of these two parameters. Light reflected off of a material in air is then given by:

$$R = [(n - 1)^2 + k^2]/[(n + 1)^2 + k^2] \tag{2.5}$$

These techniques are preferred methods for measuring thin films because they are accurate, nondestructive, and require little or no sample preparation. Schematic of the filmetrics system is shown in Figure 2.2

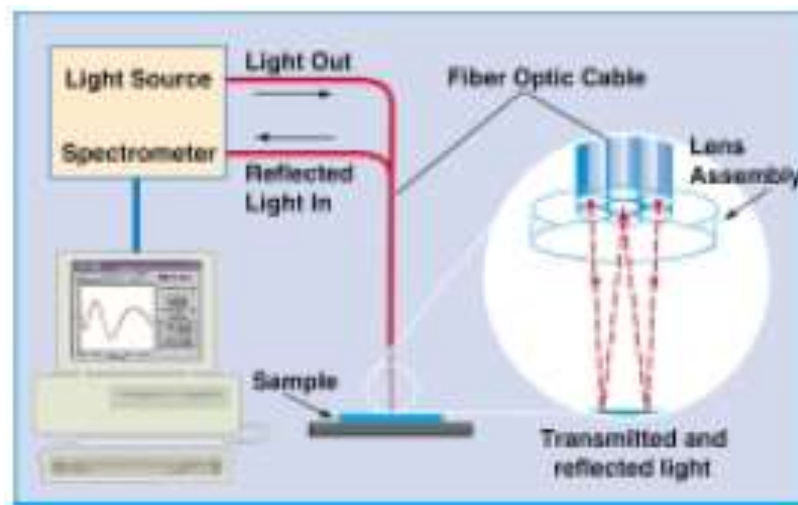

Figure 2.2 Schematic of the filmetrics system. (Filmmetrics Inc. CA)

2.5. Structural and microstructure

2.5.1. X-ray diffraction technique

X-ray diffraction is a versatile, non-destructive technique used for identifying the crystalline phases present in solid materials, thin films and powders and for analyzing structural properties (such as stress, grain size, phase composition, crystal orientation, and defects) of the phases. The method uses a beam of X-rays to bombard a specimen from various angles. The X-rays are diffracted (according to Bragg's law) as they are reflected from successive planes formed by the crystal lattice of the material. By varying the angle of incidence, a diffraction pattern emerges that is characteristic of the sample. The pattern is identified by comparing it with an internationally recognized data base containing tens of thousands of reference patterns.

When X-ray radiation passes through matter, the radiation interacts with the electrons in the atoms, resulting in scattering of the radiation. If the atoms are organized in planes (i.e. the matter is crystalline) and the distances between the atoms are of the same magnitude as the wavelength of the X-rays, constructive and destructive interference will occur. These results in diffraction where X-rays are emitted at characteristic angles based on the spaces between the atoms organized in crystalline structures called planes. Most crystals can have many sets of planes passed through their atoms. Each set of planes has a specific interplanar distance and will give rises to a characteristic angle of diffracted X-rays. The relationship between wavelength, atomic spacing (d) and angle was solved as the Bragg Equation. If the illuminating wavelength is known (depends on the type of X-ray tube used and if a monochromator is employed) and the angle can be measured (with

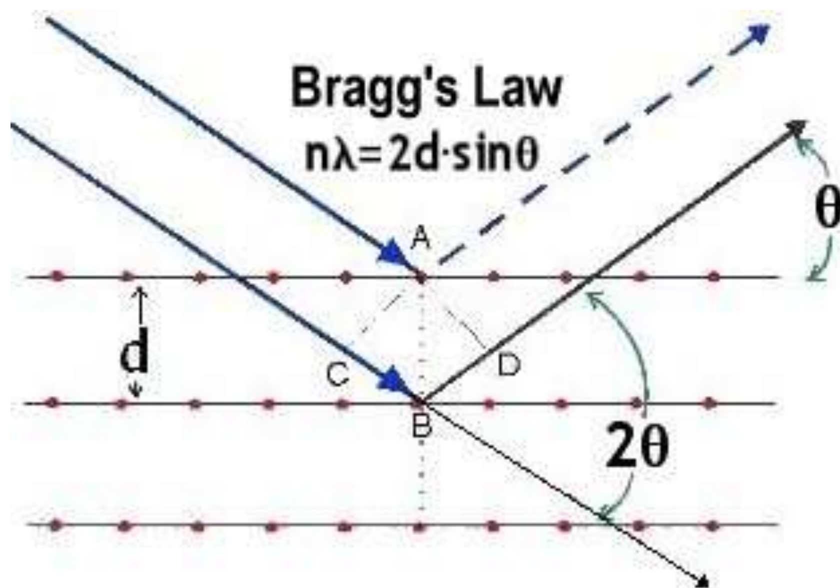

Figure 2.3. Bragg's law

a diffractometer) then the interplanar distance can be calculated from the Bragg equation. A set of ‘d-spaces’ obtained from a single compound will be represent the set of planes of d-spaces obtained from standard compounds.

$$n\lambda = 2d \sin \theta \tag{2.6}$$

Where n is the order of diffraction, λ is the wavelength of the radiation, d is the spacing between planes of atoms and θ is the angle of radiation with the diffraction plane (Figure 2.3). For most samples, the aim of the analysis is to identify the crystalline phases present. Even for work where other information is sought (i.e., unit cell calculations, quantitative determinations, etc.), identification of the phase(s) present is usually the first step. Phase identification is accomplished by comparing the data (peaks and relative intensities) from your specimen with peaks and relative intensities from a very large set of “standard” data provided by the International Center for Diffraction Data (ICDD). The widths of the peaks in a particular pattern provide an indication of the average crystallite size. Large crystallites give rise to sharp peaks, while the peak width increases as crystallite size reduce. The crystallite size is a measurement of adjacent, repeating crystalline units. The term crystallite size is commonly substituted for the term grain size when related to films. Crystallite size is performed by measuring the broadening of a particular peak in a diffraction pattern associated with a particular planar reflection from within the crystal unit cell. It is inversely related to the FWHM (full width at half maximum) of an individual peak –the more narrow the peak, the larger the crystallite size. All the crystallite size calculation was determined using the Scherrer equation once the corrected FWHM is known.

$$R = 0.9\lambda / \beta \text{Cos}\theta \tag{2.7}$$

Where R is the crystallite size (Å), λ is the wavelength of the x-ray, θ (radian) is the Bragg's angle of the 100% intensity diffraction peak and β corrected by taking into the instrumental broadening (usually silicon sample (β_s) as standard) is given by:

$$\beta = (\beta^2_m - \beta^2_s)^{1/2} \tag{2.8}$$

It is possible to distinguish between particle size and strain broadening effects by analyzing the line broadening of the X-ray diffraction profiles using the relation:

$$\beta \text{Cos}\theta/\lambda = 1/d + n\text{Sin}\theta/\lambda \tag{2.9}$$

In a plot of $\beta \text{Cos}\theta/\lambda$ versus $\text{Sin}\theta/\lambda$ one expects a straight line with zero slope (n = 0) for unstrained pure particle size broadening. A non zero slope of the straight line indicates the presence of strain due to lattice distortions. X-ray diffractograms (XRD) were recorded using Siemens D5000 X-ray diffractometer, CuK_α radiation (0.15405 nm) in 2θ range 10 to 60 degrees with scan speed of 0.5 deg/min, with step 0.02 degree and slits of 1mm-2mm-2mm-1mm widths. The peaks corresponding to *hkl* planes of the films were identified using JCPDS files.

Lattice parameters for the pseudo orthorhombic (a ≠ b ≠ c) systems were calculated from the x-ray diffractograms using the relation:

$$1/d^2_{hkl} = h^2/a^2 + k^2/b^2 + l^2/c^2 \tag{2.9}$$

Where d_{hkl} is the distance between adjacent planes in the set (*hkl*) (called as interplanar distance) and a, b, and c are the lattice parameters in x, y and z-axis, respectively.

2.5.2. Micro-Raman Spectroscopy

Raman spectroscopy is a sensitive tool to analyze the homogeneity, composition, and the required phases in the material through the symmetry allowed phonon modes. Raman spectra also indicate the structural phase transition, local order, disorder due to impurities, vacancies or doping. When a beam of monochromatic light from laser impinges upon a material, scattering occurs in all directions. If the frequency of the scattered light being the same as that of the original light (υ_o) the effect is known as Rayleigh scattering. Another type of scattering that occurs simultaneously at frequencies both higher and lower than υ_o and with considerably diminished intensities, is known as Raman effect. The difference, $\Delta\upsilon$, between incident and scattering frequencies are equal to the actual vibrational frequencies of the material[5].

Raman scattering produces scattered photons, which differ in frequency from the radiation source, which causes it, and the difference is related to vibrational and/or rotational properties of the molecules from which the scattering occurs. It has become more prominent in the years since powerful monochromatic laser sources could provide the scattering power.

In the present work the Raman spectra of these films were recorded using an ISA T64000 triple monochromator. The Raman experimental setup used in our studies is

shown in Fig 2.4. An optical microscope with 80X objective was used to focus the 514.5 nm line of a Coherent Innova 99 Ar^{+} laser on the sample. The same microscope objective collected the backscattered radiation. The scattered light dispersed by the spectrophotometer was detected by a charge-coupled device (CCD) detection system.

With 1" CCD and 1800 grooves/mm grating, the spectral resolution was typically less than 1 cm^{-1}. The laser beam traveled through a set of filters, polarization rotator, and iris and then it was brought to a sample through the Olympus BH2-UMA microscope with an 80X objective equipped with a NEC NC-15 camera. For temperature dependent measurements, the illumination of the samples was adjusted at each temperature.

Scattered light was passed through a polarizer and analyzer and through a set of mirrors brought to the entrance slit of the triple grating spectrophotometer ISA Model T64000 equipped with liquid nitrogen cooled CCD detector and photomultiplier tube (PMT). The backscattering spectra were recorded using a Raman microprobe system interfaced to a computer. Data analysis was carried out using the software packages, namely PeakFit v4.02 (Jandel Scientific Software) and Origin 7.5 (OriginLab Corporation).

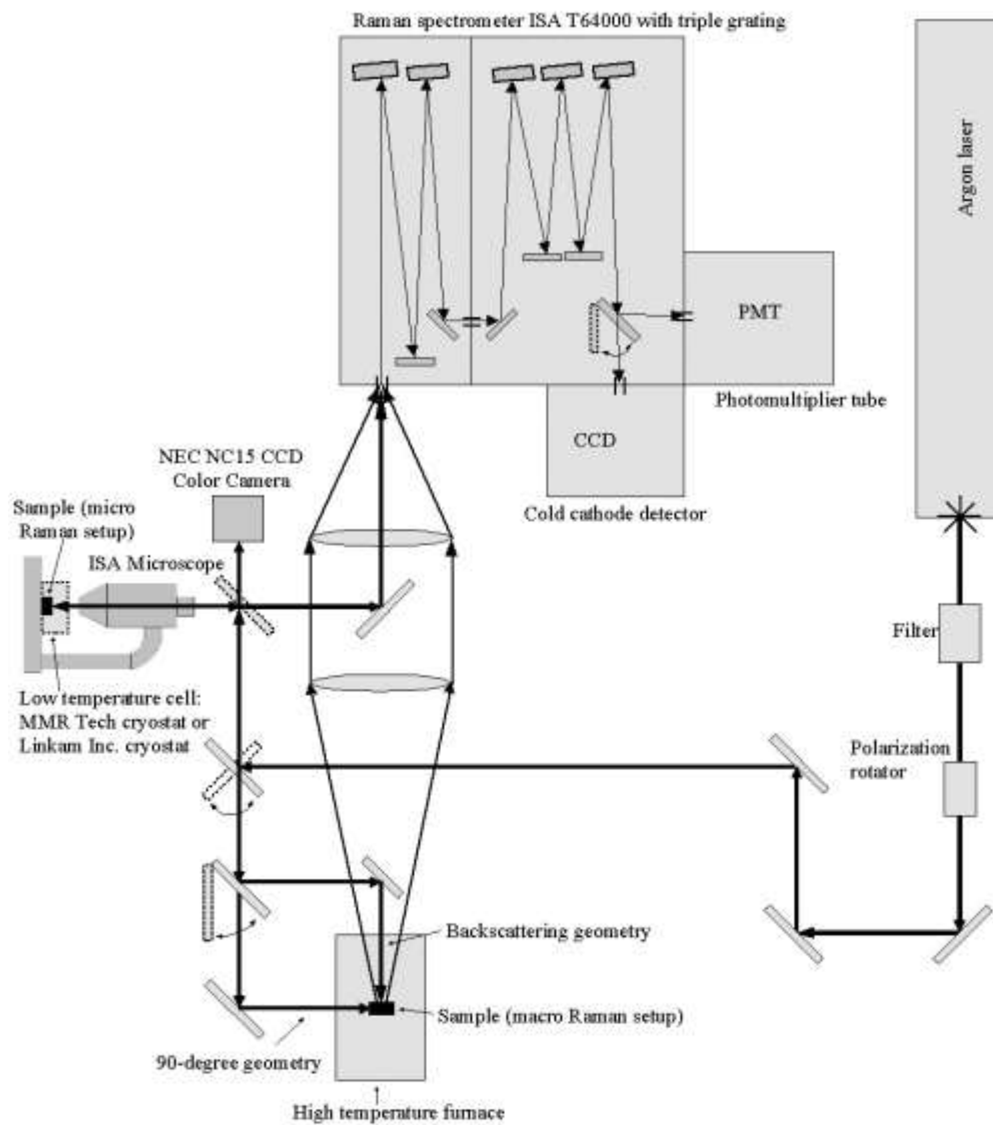

Figure 2.4. Experimental set up of the micro Raman scattering

2.6 Ferroelectric, Fatigue, Dielectric and Leakage measurements

2.6.1. Electrodes

The selection of capacitor electrode materials for the nonvolatile ferroelectric random access memory (FeRAM) is one the most important issues because capacitor electrical characteristics are strongly influenced by the electrode materials (remnant polarization, coercive field, dielectric constant, leakage current, etc) and reliabilities (fatigue, imprint, retention, etc). The electrode for high dielectric or ferroelectric oxides should be stable under oxidizing atmosphere and high temperature, because it undergoes these conditions when the oxide films are formed on it and the subsequent processes are performed. The most conventional electrode material for ferroelectric capacitors is Platinum (Pt), because complies the above conditions.

Films were measured in the metal-ferroelectric-metal (MFM) configuration by using Pt (Pt/TiO_2/SiO_2/Si) substrate and Pt top electrode. DC magnetron sputtering was used to deposited Pt top electrodes trough shadow mask of diameter 200 μm (electrode area 3.14 x $10^{-4}$$cm^2$) with thickness of 200 nm. Samples were etched on the surface to get the bottom contact. The top and bottom electrode contacts with the samples were made using a high resolution microscopositioner S-725. All room temperature measurements were carried out on a H100 Signatone probe station using the micropositioners.

2.6.2. Hysteresis and Fatigue measurements

The Polarization hysteresis nature of the films was analyzed using a ferroelectric test system RT-6000 HVS from Radiant Technologies Inc[6]. The Sawyer Tower measuring

technique is an established and accepted method to measure the ferroelectric polarization response of the non linear capacitors. It utilizes a sense capacitor in series with the device under test and measures the voltage drop across the test sample as shown in figure 2.6. For thin film measurement, we usually use virtual ground mode with a voltage range of +20 to -20 V. Apart from hysteresis the instrument also allows us to measure fatigue, retention, pulse hysteresis, and resistivities of thin film and bulk ferroelectric samples. The instrument has its in built microcomputer for control, data acquisition and analysis.

2.6.3. Dielectric measurements

The dielectric constant and the tangent loss were measured as the function of frequency (1 KHz to 1 MHz) using an HP 4294 impedance analyzer. The dielectric constant of the film was calculated from the measured capacitance in the parallel plate capacitor configuration. The dielectric constant measures the amount of charge that an electrode slab of material can store, relative to the charge that would be stored by identical electrodes separated by air or vacuum at the same voltage. In other words, dielectric Constant can be defined as,

$$\mathbf{K = \varepsilon/\varepsilon_0 = C\, d/ \varepsilon_0\, A} \qquad \textbf{(2.7)}$$

Where, ε is the permittivity of dielectric material 'A' area of the electrodes, 'ε_0' permittivity of free space = 8.85×10^{-14} farad/cm., 'd' thickness of the film, and 'C' is the capacitance of the film.

Dissipation (or loss) factor, is a measure of the dielectric loss in a material defined as the tangent of the loss angle, tan δ, i.e. the ratio of the imaginary part ε'' to the real part $\varepsilon'$of the permittivity.

2.6.4. Current- Voltage (I-V) Characteristics

Ferroelectrics are insulators. Insulators are materials that have no free electrons in their atomic structure, which are free to move under any applied field. In dielectrics, the electrons are tied up in ionic and covalent bonding of the atoms, and by definition these materials should possess almost infinite electrical resistivity. In reality, however, insulators do not display infinite but limited resistivity, as there are impurities and defects in the atomic lattice structure which give rise to charge carriers and which increases the leakage current. Ohm's Law states that the current (I) in a conductor is related to the applied voltage (V) and the resistance (R) of the conductor as:

$$\mathbf{I = V/R} \quad \textbf{(2.8)}$$

The resistance (R), however, is a dimensionally dependent property, and is related to the intrinsic resistivity of the material (*p*) as follows:

$$\mathbf{R = \rho L/A} \quad \textbf{(2.9)}$$

Where L = the length of the conductor, A = the cross sectional area of the conductor

The current (I), therefore, can be expressed as:

$$\mathbf{I = VA/\rho L} \quad \textbf{(2.10)}$$

When considering a capacitor, the leakage current (i) through the insulator can be expressed as in the above formula:

$$\mathbf{i = VA/\rho d} \qquad \mathbf{(2.11)}$$

Where, V = test voltage, A= active electrode area ρ = dielectric resistivity, d = dielectric thickness of the dielectric. As is evident from the above relationship, for any given test voltage (V), the leakage current is directly proportional to the active electrode area of the capacitor, and is inversely proportional to the thickness (and resistivity) of the dielectric layer.

The current –voltage (I-V) characteristics of thin films were done using Keithley made source measure unit which was connected to the probe stations either the room temperature one or if required with the MMR unit. The electrometer is computer interfaced with Labview software for instrument control and data acquisition. The set up allows us to measure the I-V characteristics of ferroelectric thin films in a wide temperature range. The home made junction box is used to connect the sample either to the hysteresis measurement unit or I-V set up or the impedance analyzer.

2.7 References

1. Alain C. Pierre, *Introduction to Sol-Gel Processing*, (Kluwer, Norwell, MA, 1998).
2. C.J. Brinker and G.W. Scherer, *Sol-Gel Science: The Physics and Chemistry of Sol-Gel Processing*, (Academic Press, San Diego, CA, 1990).
3. Huang, Yuhong; Zheng, Haixing; and Forsyth, Ian, *Application of Functional ceramic and Hybrid Nanostructure Coating Fabrication via Sol-Gel Processes, Fine, Ultrafine and Nano Powders* (Oct. 29-31, 2000, Montreal, Canada).
4. *Advanced thin-film measurement systems manual*, (Filmmetrics, Inc. CA, 1998).

5. K. Nakamoto*, infrared and Raman spectra of Inorganic and coordination compounds, (John Eiley and Sons, New York).*

6. RT6000 HVS Radiant Manual, Radiant Technologies Inc. New Mexico (1994).

SUMMARY (Chapters 3-6)

Recent interest[1,3] in bismuth-layer-structured ferroelectrics (BLSFs) such as $SrBi_2Ta_2O_9$ (SBT) is due to its good fatigue endurance[4,5], but the low polarization and high temperature processing (> 800ºC) is the limitation for integrating it in CMOS technology. Therefore, other lead free materials based on $Bi_4Ti_3O_{12}$ were investigated, but pure $Bi_4Ti_3O_{12}$ also shows very low polarization. However, the idea[6], that partially replacing Bi ion site by a trivalent transition metal or rare earth element may affect the polarization properties, was interesting. Ferroelectric response of La substituted $Bi_4Ti_3O_{12}$ with the composition $Bi_{3.25}La_{0.75}Ti_3O_{12}$ (-75) thin films deposited at 650° C by pulsed laser deposition showed[6] fatigue free response but poor polarization (~ Pr = 14 μC/cm^2). The fatigue-free behavior of SBT and thin films may be explained by the charge compensating effect of the Bi_2O_2 layers resulting in the space charges and in the unpinning of domain walls[7]. The ionic sizes of the Bi and trivalent ion also play an important role as explained in this chapter later. However, low polarization ($2P_r$ = 20 C/cm^2 for SBT and $2P_r$= 27 μC/cm^2 for, respectively) seems to be a serious disadvantage for high-density integration in FeRAMs[8]. Being lead free material, these material systems are potential candidate to replace PZT, if their ferroelectric response is improved at process temperatures compatible with standard Si based CMOS technology. However, world wide research activity[9-12] on substituted $Bi_4Ti_3O_{12}$ films enhanced a lot in the past several years. Literature survey indicates that the ferroelectric properties, crystal

structure, and the microstructure of BLSFs thin films are sensitive to the substitution of different-sized ions in the bismuth layer-structured compounds. Shimakawa *et al*. reported[13] that TiO_6 octahedra in pseudo-perovskite blocks are shifted along the a-axis which causes an increase in polarization due to substitution for Bi in the pseudo-perovskite blocks.

In order to understand the basic phenomena and material processing, a research program was initiated at UPRM to investigate the behavior of rare earth substituted $Bi_4Ti_3O_{12}$ material stystem. The structure-property relation of $Bi_{4-x}M_xTi_3O_{12}$ (where M = La, Nd, Sm, and Gd) material system is presented in this thesis. Because, the ionic size reduces from La to Gd in a sequence its effect is observed on the ferroelectric polarization and fatigue phenomena. The research performed is presented for each material system in Chapters (3-6) separately for their structural, electrical, and ferroelectric properties. The results show significant increase P_r values and fatigue free response, as demonstrated in the text. Thus, this material system is ideally suitable for practical devices.

Chapter 3

Studies of $Bi_{4-x}La_xTi_3O_{12}$ for ferroelectric devices

3.1 Introduction

$Bi_{4-x}La_xTi_3O_{12}$ (BLT) materials were prepared by sol-gel process and thin films were deposited by spin coating on Pt ($Pt/TiO_2/SiO_2/Si$) substrate. Structural properties of the films were examined by x-ray diffraction and Raman spectroscopy. films annealed at 700°C were found to have of a single phase of a bismuth-layered structure with preferred (117) orientation. La substituted $Bi_4Ti_3O_{12}$ leads to a marked improvement in the remanent polarization (P_r) and the coercive field (E_c). The thin film showed a large remanent polarization Pr = 47.5 $\mu C/cm^2$ for x = 0.56 composition (which is much higher than other reports). However, after 1.4 $x10^9$ switching cycles, 15.3% degradation of P_r is observed in the film. The measured leakage current in films were much lower in comparison with pure Bi_4Ti_3O12. The leakage current (less than 10^{-7} A/cm^2) at low field was observed in the film with composition x = 0.46, 0.56 and 1.50. These results indicate the potential application of La substitution bismuth titanate films in non-volatile ferroelectric memories.

Bismuth-layer-structured ferroelectrics (BLSFs) are described as $(Bi_2O_2)^{2+}(A_{n-1}B_nO_{3n+1})^{2-}$ (also known as the Aurivillius family of compounds, where A is mono-, di-, or trivalente ions or a mixture of them; B is tetra-, penta-, or hexavalent ions; *n* is the

number of BO_6 octahedron in the pseudo-perovskite layer).[14,15] (BLSFs) such as $SrBi_2Ta_2O_9$ (SBT) and $Bi_4Ti_3O_{12}$ (BTO) since their discovery, tremendous efforts have been focused on the preparation of either bulk or thin films and characterization of these materials. SBT has the Bi-layered perovskite structure where the double Ta-O octahedron layers were sandwiched between the $(Bi_2O_2)^{2+}$ layers. A conventional model claims that the $(Bi_2O_2)^{2+}$ layers should make SBT fatigue free: namely, the layers have net electrical charges, so their position in the lattice become self-regulated to compensate for the space charges due to oxygen vacancies. Noh, *et al.* show[16] that oxygen vacancies are preferably present near the Bi ions at the $(Bi_2O_2)^{2+}$ layers in SBT and oxygen vacancies can be induced in the neighborhood of the Bi and the Ti ions in $Bi_4Ti_3O_{12}$. Since ferroelectric responses are originated mainly from the metal-oxygen octahedral, the fatigue failures of $Bi_4Ti_3O_{12}$ films should be related to oxygen vacancies present at the titanium-oxygen octahedral. In addition to the self-regulating adjustment of the $(Bi_2O_2)^{2+}$ layers, the strong oxygen stability (for Ti valence is +4 and for Ta valence is +5) predicts the SBT films fatigue free.[17] It was known that La-substituted in $Bi_4Ti_3O_{12}$ has the highest solubility limits.

The ferroelectric properties, the crystal structure, and the microstructure of BLSFs thin films are sensitive to the substitution of different-sized ions in the bismuth layer-structured compounds. In this chapter, we report about $Bi_{4-x}La_xTi_3O_{12}$ (BLT) thin films with high polarizations produced by using sol-gel method to substitute La for Bi in $Bi_4Ti_3O_{12}$ structure. The structural and ferroelectric properties of the thin films were investigated in this chapter.

3.2. Experimental Details

The precursor solutions for $Bi_{4-x}La_xTi_3O_{12}$ (with x = 0.00, 0.16, 0.26, 0.36, 0.46, 0.56, 0.75, 0.95, 1.00 and 1.50.) were Bismuth nitrate pentahydrate, lanthanum nitrate hexahydrate, and titanium isopropoxide. Bismuth nitrate pentahydrate and lanthanum nitrate hexahydrate were initially dissolved in acetic acid and then mixed together to obtain Bi and La stock solutions. Titanium isopropoxide was added in this solutions were mixed together to prepare the stoichometry, clear, transparent, and stable precursor. A 5% excess amount of bismuth nitrate pentahydrate was used to compensate for the Bi loss that occurs during the annealing process. Sol was prepared as mentioned in chapter 2 of the section 2.3.1.

For the fabrication of the thin films, the diluted sol (0.3M) of the desired composition was used the precursor solution was syringed through a 0.2 μm syringe filter onto a $Pt/TiO_2/SiO_2/Si$ substrate. The films were produced by using a spin-coating technique with a spinner operated at 3000 rpm for 30s. To remove the organic contaminations, after the spin-coating procedure, we kept the films on a furnace at 600°C for 5 min. The coating and firing cycles were repeated required number of times. The pre-baked films were annealed at 700° C for 1 h under air atmosphere for crystallization. An optical thin films thickness measurement unit (F-20 Filmetrics Inc) was used to evaluate the thickness from the measured reflection spectrum of the annealed films. The top electrodes, 200 μm in diameter, were fabricated by using dc magnetron sputtering to deposit a 200 nm thick Pt film at room temperature.

Cu-K_α radiation (0.15405 nm) was used for recording x-ray diffraction patterns on $Bi_{4-x}La_xTi_3O_{12}$ materials for different compositions using Siemens D5000 x-ray diffractometer to determine the degree of orientation and crystallinity of the thin films. Room temperature micro-Raman spectra of the films were obtained by a spectrometer with triple monochromator (Jovin Yvon T6400) in a back scattering geometry. The spectra were excited with an Ar-ion laser operating at a wavelength of 514.5 nm. The frequency dependent dielectric permittivity and tangent loss were studied from 1 KHz to 1 MHz with an oscillating voltage of 500 mV using an HP 4294A impedance analyzer. The P-E hysteresis loops were measured using ferroelectric tester RT 600 HVS (Radiant Tech.) at virtual ground mode. Fatigue behavior was examined by applying triangular wave at 100 KHZ and 282 kV/cm. Leakage current behavior was studied by electrometer (keithley 6517) interfaced to a computer with a voltage step 0.2V and delay time of 10 s.

3.3 Result and Discussions

3.3.1 XRD Analysis

Figure 3.1 shows the X-ray diffraction patterns of $Bi_{4-x}La_xTi_3O_{12}$ (BLT) thin films on $Pt/TiO_2/SiO_2/Si$ substrate for the compositions x = 0.00, 0.16, 0.26, 0.36, 0.46, 0.56, 0.75, 0.95, 1.00 and 1.50. Miller indices were indexed according to the previous XRD data for BTO, are indicated for the diffraction peaks. As shown in Fig. 3.1, all of the films consisted of a single phase of a bismuth layered structured showing the preferred (117) orientation. The crystalline quality of the film can be estimated from the measured half width (FWHM) of the most intense (117) diffraction peak. Smaller

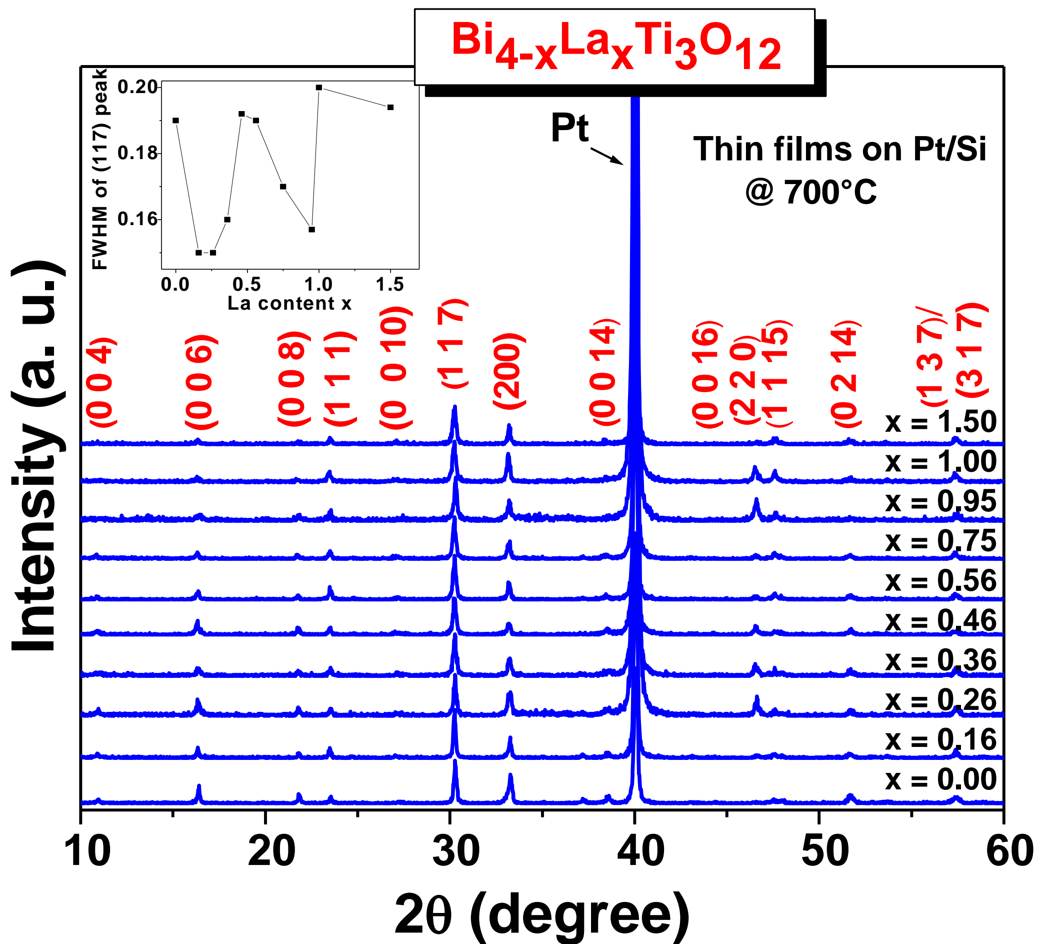

Figure 3.1 X-ray diffraction patterns of $Bi_{4-x}La_xTi_3O_{12}$ () thin films on $Pt/TiO_2/SiO_2/Si$ substrate for the compositions x = 0.00, 0.16, 0.26, 0.36, 0.46, 0.56, 0.75, 0.95, 1.00 and 1.50. The inset shows the variation of the FWHM of (117) peak with La content.

TABLE 3.1 Variation of crystallite size for different La content in $Bi_4Ti_3O_{12}$ films

Composition X	Crystallite size (nm)
0.00	62
0.16	58
0.26	58
0.36	54
0.46	45
0.56	46
0.75	51
0.95	55
1.00	43
1.50	44

FWHM value indicates better crystallinity of the film. The crystallite sizes of the $Bi_{4-x}La_xTi_3O_{12}$ films were calculated using Scherrer formula[18]. Table 3.1 shows that the crystallite sizes decrease as the La content increase. This may support the microstructural observation, as done using SEM (scanning electron microscopy), that the average grain size of perovskite films decreases with increasing La-content. The lattice parameters of the $Bi_{4-x}La_xTi_3O_{12}$ films were calculated from their X-ray diffractograms. The lattice constants *a*, *b*, and *c* for which were estimated from the (006), (200) and (111) Bragg reflection in the XRD patterns, are presented in figure 3.2 where shows the variation of lattice constants of thin films as a function of La content. The slightly change in lattice constants indicates that La ions are dissolved in the BTO lattice systematically for all compositions ($0 \leq x \leq 1.50$). The lattice distortion (*b*/*a* ratio) of the orthorhombic phase was smallest in the samples.

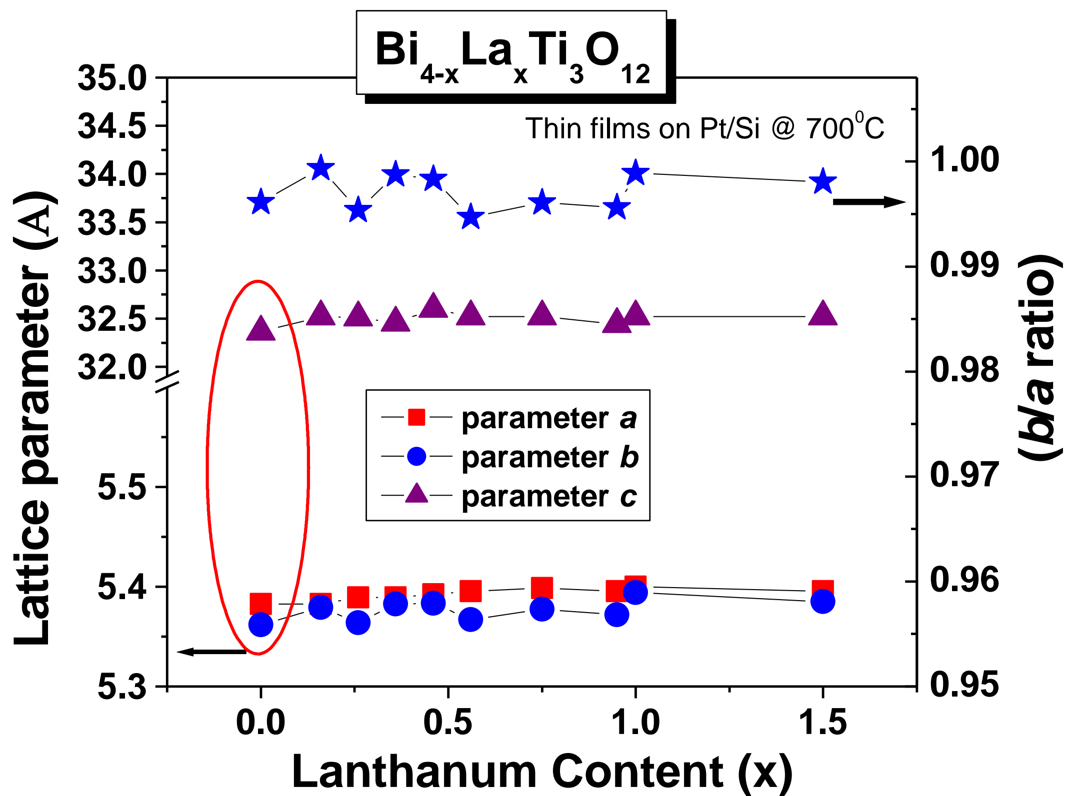

Figure 3.2 Variation in lattice parameters of BLaT thin films with different La content.

Figure 3.3 shows the SEM micrographs of (a) x = 0.00, (b) x = 0.26, (c) x = 0.56 d) x = 0.75 and e) x= 1.50 for $Bi_{4-x}La_xTi_3O_{12}T$ thin films on $Pt/TiO_2/SiO_2/Si$ substrates. As shown in micrographs, small grains of arbitrary shape are observed, the grain size of the $Bi_4Ti_3O_{12}$ film is substantially larger than that of the $Bi_{4-x}La_xTi_3O_{12}T$ films (x = 0.26, 0.56, 0.75 and 1.50) because of lower diffusivity of lanthanum. The substitution of lanthanum for bismuth suppresses the grain growth of. Therefore, the substitution of La^{3+} for Bi^{3+} in $Bi_4T_3O_{12}$ films lead to reduction in grain size.

3.3.2 Micro Raman analysis

Figure 3.4 shows the room temperature Raman spectra of preferred (117) orientation of the thin films in backscattering geometry using JY T64000 triple-monochromator. An optical microscope with 80X objective was used to focus the 514.5 nm excitation radiation from a Coherent Innova 99 Ar^+ laser and to collect the scattered radiation. The scattered signal was detected by a charge-couple device (CCD) detection system. The Raman selections rules in Aurivillius $Bi_4Ti_3O_{12}$ allow 16 phonon modes of different symmetries ($6 A_{1g} + 2 B_{1g} + 8 E_g$) if a tetragonal structure of the lattice is considered. It consist of Bi_2O_2 layers and perovskite-type structures ($A_{m-1}B_mO_{3m+1}$) with triple TiO_6 octahedra and A site Bi atom. The Bi^{3+} ion in A site is strongly under bonded and Ti^{4+} ion in B site is slightly over bonded. However, different numbers of Raman modes from $Bi_4Ti_3O_{12}$ have been reported in the literature[19-21], which can be explained by the possible overlap of the same symmetry vibrations and orthorhombic distortions of the material[22]. Figure 3.4 shows the room temperature recorded Raman spectra of

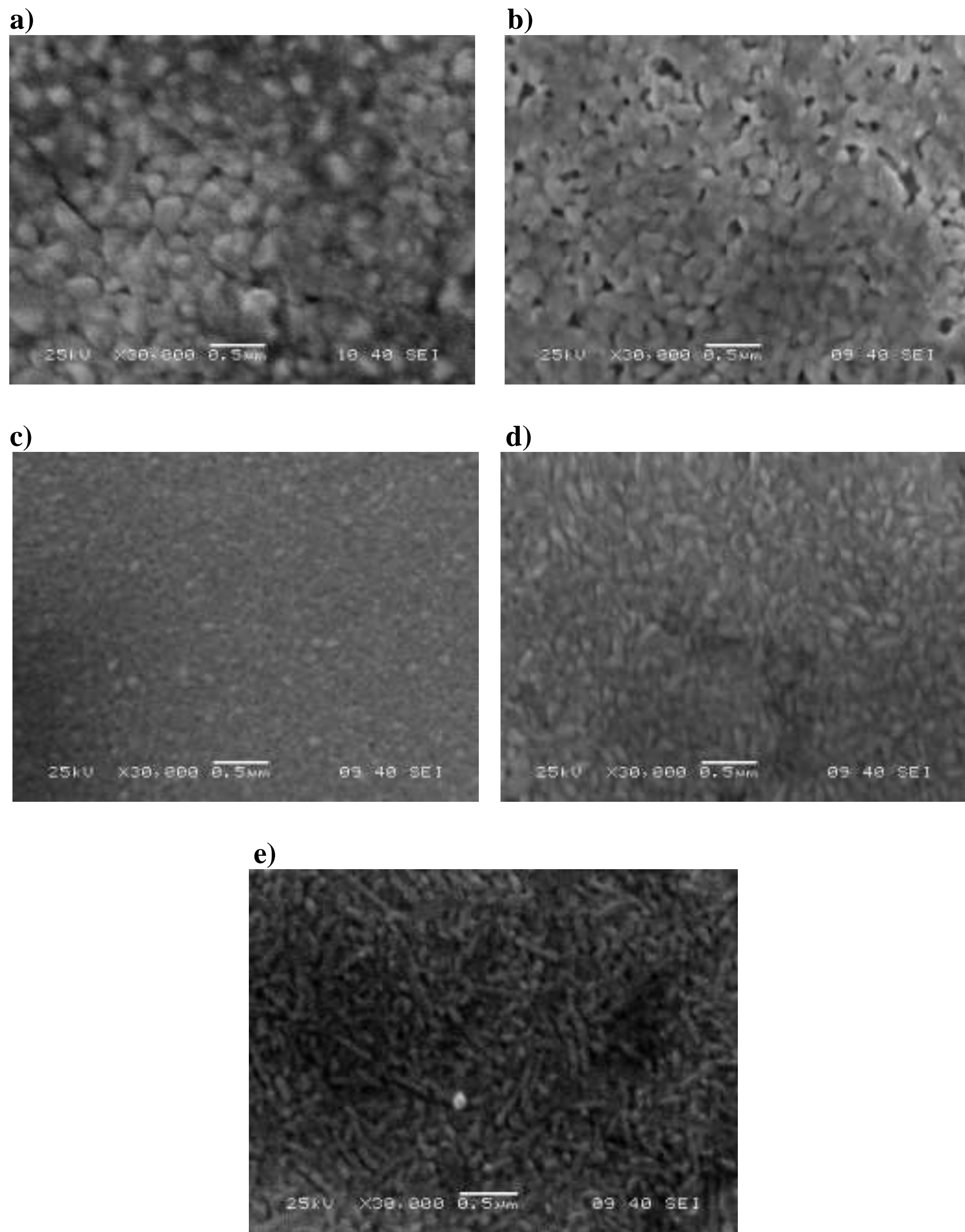

Figure 3.3. SEM micrographs of (a) BTO, (b) x = 0.26, (c) x = 0.56, (d) x = 0.75 (e) x = 1.50 Lanthanum content in BTO thin films on $Pt/TiO_2/SiO_2/Si$ substrate.

$Bi_{4-x}La_xTi_3O_{12}$ films for compositions: x = 0.00, 0.16, 0.26, 0.36, 0.46, 0.56, 0.75, 0.95, and 1.50. The Raman modes of $Bi_4Ti_3O_{12}$ films are in agreement with those observed in its crystal[19]. The film spectrum exhibits intense phonon modes at about 28, 45, 62, 115, 270, 540 and 850 cm^{-1} and many other weak features. As the vibrational modes strongly depend on the atomic masses, the heavy Bi ions should be responsible for the low frequency modes (ν <100 cm^{-1}). The 62 cm^{-1} mode is known to originate from[19,20] the Bi displacements in Bi_2O_2 layer. The modes at about 270, 540 and 850 cm^{-1} are the internal modes of TiO_6 octahedra having A_{1g} character. The compositional dependence of Raman spectra shows the similar effects on these internal modes they weaken and broaden with increasing content of La in films. Such changes are possible as La substituted BTO is expected to introduce cationic disorder even though there is only a small difference in the ionic radii of Bi^{+3} and La^{+3} ions. The triplet bands at 86, 115 and 150 cm^{-1}, which were assigned to the modes of Bi ions (A site), became diffuse and their frequency increased clearly with increasing La content. If La substitutes Bi on the A-sites of the lattice, an increase in the mode frequency is expected from the mass difference as Bi is 1.50 times heavier than La, which is in accordance with the observed hardening of these modes. These results suggest that the La^{3+} ions are mainly incorporated into the Bi site (A site) of the perovskite slab for low La contents ($x < 0.95$). For higher La content ($x > 0.95$), on the other hand, the situation appear to be different. Most prominent effect of La substituted was observed on the low frequency modes. The Raman frequencies were obtained for each composition by fitting the peaks with the damped harmonic oscillator-type phonon functions La are plotted in figure 3.5. The lowest frequency (28 cm^{-1}) mode,

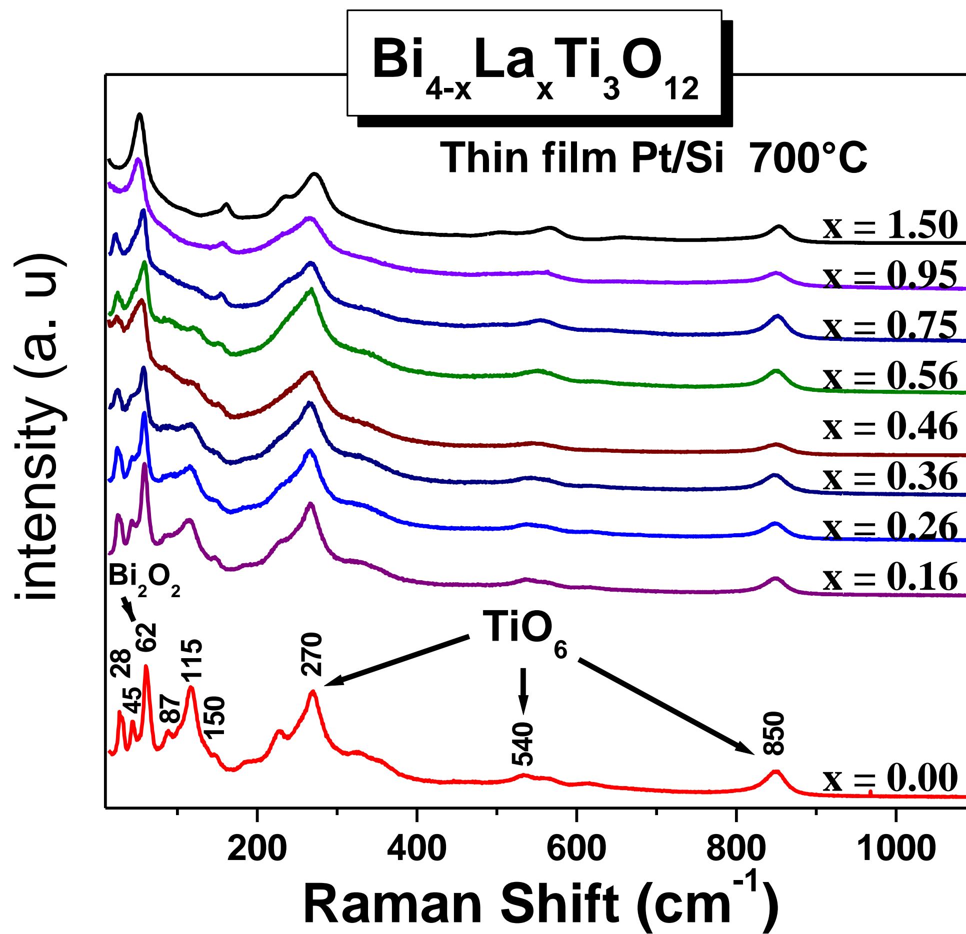

Figure 3.4. Room temperature Raman spectra of $Bi_{4-x}La_xTi_3O_{12}$ films on a Pt substrate ($Pt/TiO_x/SiO_2/Si$) for x = 0.00, 0.16, 0.26, 0.36, 0.46, 0.56, 0.75, 0.95, and 1.50 composition. The indexes in the figure indicate peculiar modes to the local structures.

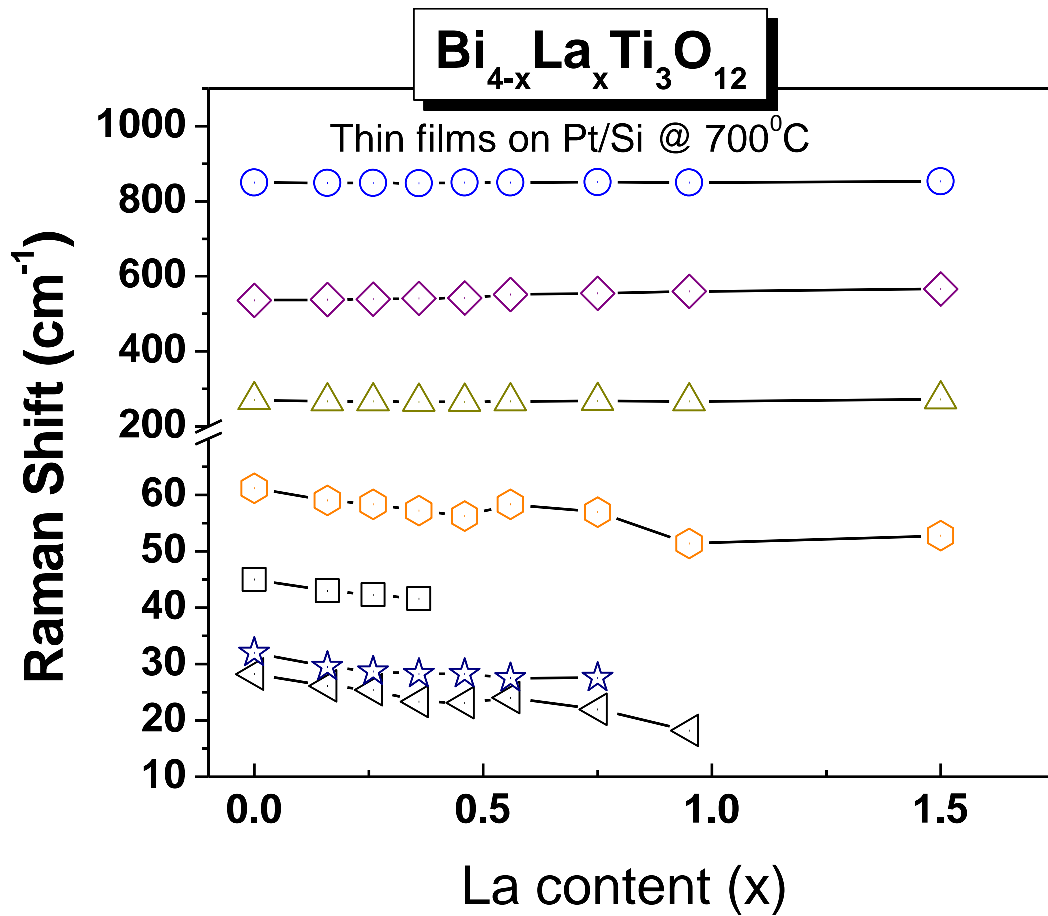

Figure 3.5. Raman frequencies as a function of Lanthanum compositions in $Bi_{4-x}La_xTi_3O_{12}$ thin films.

which has been assigned as a soft-mode responsible for a phase transition at 675°C for $Bi_4Ti_3O_{12}$, shows softening behavior with La substituted. Compared to the soft mode, a little variation in the 32 cm^{-1} mode and the 62 cm^{-1} mode suggest that the substituted process least affects the Bi_2O_2 layers for ($x < 0.95$). As shown in Fig. 3.4, the peak of the Bi_2O_2 layer mode at 62 cm^{-1} clearly broadens at $x \geq 0.95$ where the La ions start to incorporate into the Bi_2O_2 layers. This indicates the compositional inhomogeneity occurring in the Bi_2O_2 layers. We note that this type of cation disorder also seems to affect the ferroelectric property of this material. It should also be noted that the superior properties with fatigue-free characteristic are poised at $x = 0.56$ as demonstrated in section 3.3.3, but for the composition $x = 0.95$ where La^{3+} ions start to incorporate into Bi_2O_2 layers the polarization was affected. The inclusion of La^{3+} ion into the Bi site (A site) of perovskite block is expected to influence the electrical properties of $Bi_4Ti_3O_{12}$ thin films in two ways, First, by partial replacement of the volatile constituent Bi^{3+} by La^{3+} ions, which contributes to the chemical stability of oxygen ions in perovskite block and may yield better fatigue resistance and reduce the leakage current density. Bi loss is due to the volatility of Bi_2O_2 during the high temperature annealing of these films creates oxygen vacancies in the lattice. The second factor worth consideration is that the inclusion of La suppresses the dominant *c* axis growth in these films. It is known that the *c* axis oriented films have poor polarization value as compared to the *a* or *b* axis oriented films.[23] Therefore, any tilt of the TiO_6 octahedra towards the a-b plane should increase the polarization values of this material.

Another aspect considered in this work is the influence of La substitution on structural instability for $Bi_{4-x}La_xTi_3O_{12}$. Displacive ferroelectrics normally have at least one low-energy mode which softens approaching T_c. Similarly, one or more vibrational modes in a solid solution may soften when a structural phase transition is approaching by compositional modifications at constant temperature. Indeed, we find that the lowest frequency mode at 28 cm^{-1} shows some interesting behavior at room temperature. As is clearly evident in the low-frequency spectra of Fig. 3.4, this mode softens by ~14 cm^{-1} between $x = 0$ and $x = 0.95$ then disappears (at $x \leq 1.50$) probably due to the overdamping. Therefore, the ferroelectric-paraelectric phase transition for heavily La-substituted BTO occurs at room temperature at $x \approx 1.0$.

In the ferroelectric phase, the structure of BLSFs compounds can be described by small orthorhombic or monoclinic deviations form the undistorted I4/*mmm* parent structure. The structural study of withers *et al.* on BTO[24] suggests that the major component of large spontaneous polarization originates from the large *a*-axis displacement (with *F2mm* symmetry) of The Bi^{3+} ion in the perovskite A site. Thus, the quenching of the *F2mm* distortions of the Bi^{3+} ion (A site) should be correlated with the ferroelectric-to-paraelectric phase transition. In the parent BTO, the Bi^{3+} ions strongly deviate from the center of the dodecahedral coordination site of the ideal perovskite structure, leading to the distortion of the lattice.[24,25] In , the symmetric nonpolarizable La^{3+} ions tend to occupy the center of the 12-coordinated polyhedron. The replacement of the Bi^{3+} by La^{3+} ions would reduce the orthorhombic distortion causing a decrease of T_c. The softening of the 28 cm^{-1} mode indicates that the soft mode might originate form the

vibration of the Bi^{3+} ion in the perovskite A site. Figure 3.6 shows the squared frequency of this mode as a function of the La content. The date are well fitted by the following linear relation: $\omega(x)^2 = \omega(0)^2 - Ax$, where $\omega(0)$ is the soft-mode frequency at $x = 0$ and $A = 436.51$. In the mean-field approximation, the frequency of the soft mode is determined by the difference between the short-range force and the Coulomb forces.[26] The phase transition occurs when the short-range force cancels the Coulomb forces, leading to vanishing of the soft-mode frequency. Since the isovalent and nonpolarizable impurity ions only change the short-range force, the substitution of La for Bi alters the short-range force, reducing the soft-mode frequency. The marked similarity between the effects of La substituted BTO and temperature on the soft mode shown by Osada, *et al.* on [27] where the temperature dependence of this mode for BTO is proportional to that of the spontaneous polarization, the soft-mode frequency for substituted material constitutes a valuable probe of structural instability linked to the ferroelectric property in $Bi_4Ti_3O_{12}$. In this content, we find a clear trend between the soft- mode frequency and T_c for $Bi_{4-x}La_xTi_3O_{12}$. Although further studies on different substitutes systems are needed to clarify this correlation, such data should provide useful guidelines for designing BTO-based materials with controlled properties.

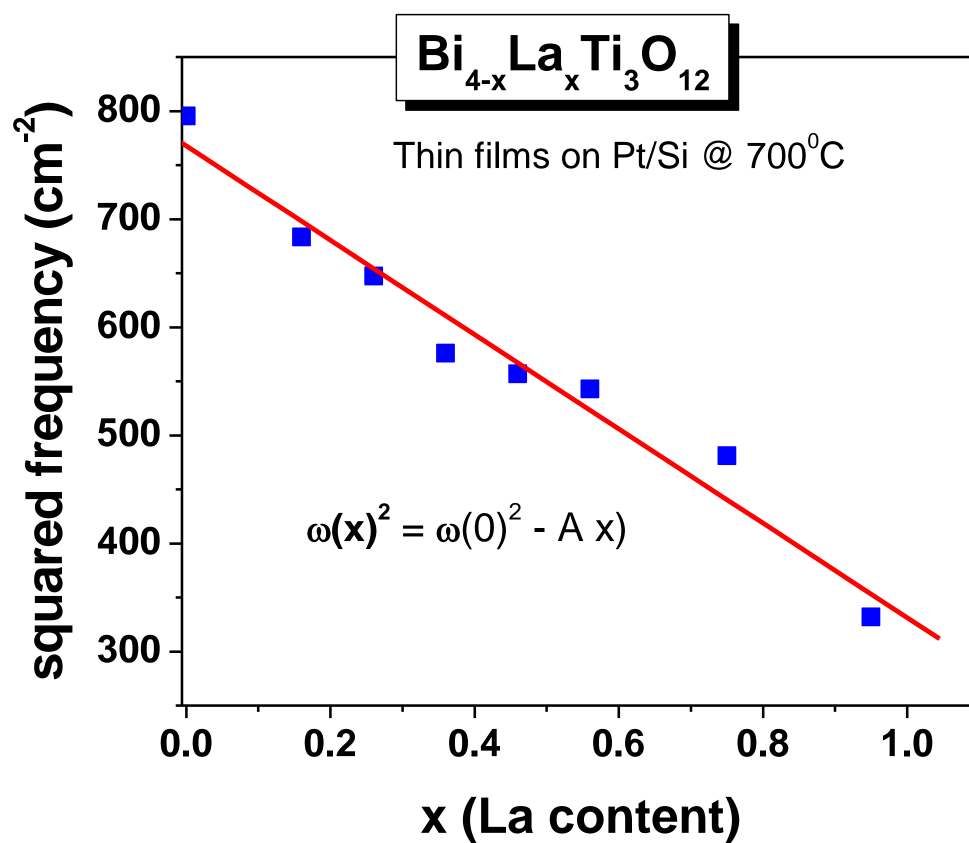

Figure 3.6. Room temperature raman squared frequency of the soft mode as a function of Lanthanum compositions in $Bi_{4-x}La_xTi_3O_{12}$ thin films.

3.3.3. Ferroelectric properties of $Bi_{4-x}La_xTi_3O_{12}$ thin films

For ferroelectric measurements, the top circular electrodes of platinum 200 nm thick and 200 μm diameter were deposited by dc sputtering. Ferroelectric response was recorded by RT6000HVS probe (Radiant Tech.) in virtual ground mode. For comparison, the ferroelectric response for $Bi_{4-x}La_xTi_3O_{12}$ thin films of the compositions x = 0.00, 0.46, 0.56, 0.56 (annealed electrode), 0.75 and 0.95, is showed in Fig.3.7. Before ferroelectric measurements, Pt/(117) oriented $Bi_{3.44}La_{0.56}Ti_3O_{12}$/Pt capacitor structure was post annealed at 200^0C to improve the top Pt electrode. A polarization ($2P_r$ ~ 95 μC/cm^2) for the film with composition x = 0.56 is shown in figures 3.7 (a) and 3.7 (b) with coercive field Ec = 100 kV/cm for a maximum applied electric field 266 kV/cm. In un-annealed capacitor structure $2P_r$ ~ 84 μC/cm^2 is shown in the figure 3.7(b). For other compositions the polarization is much lower. The effects of the La-content on the variation of the remnant polarization (Pr) and the coercive field (Ec) of thin film were systematically examined at an applied electric field. As presented in figure 3.8, the value of the P_r increases gradually with increasing La-content for x below a certain critical level. The P_r shows its maximum value of 47.59 μC/cm^2 at x = 0.56 (annealed electrode) and decreases thereafter. The E_c increases rather steeply with increasing La-content from 48 to 100 kV/cm. The E_c shows its maximum value at x = 0.56 and decreases gradually

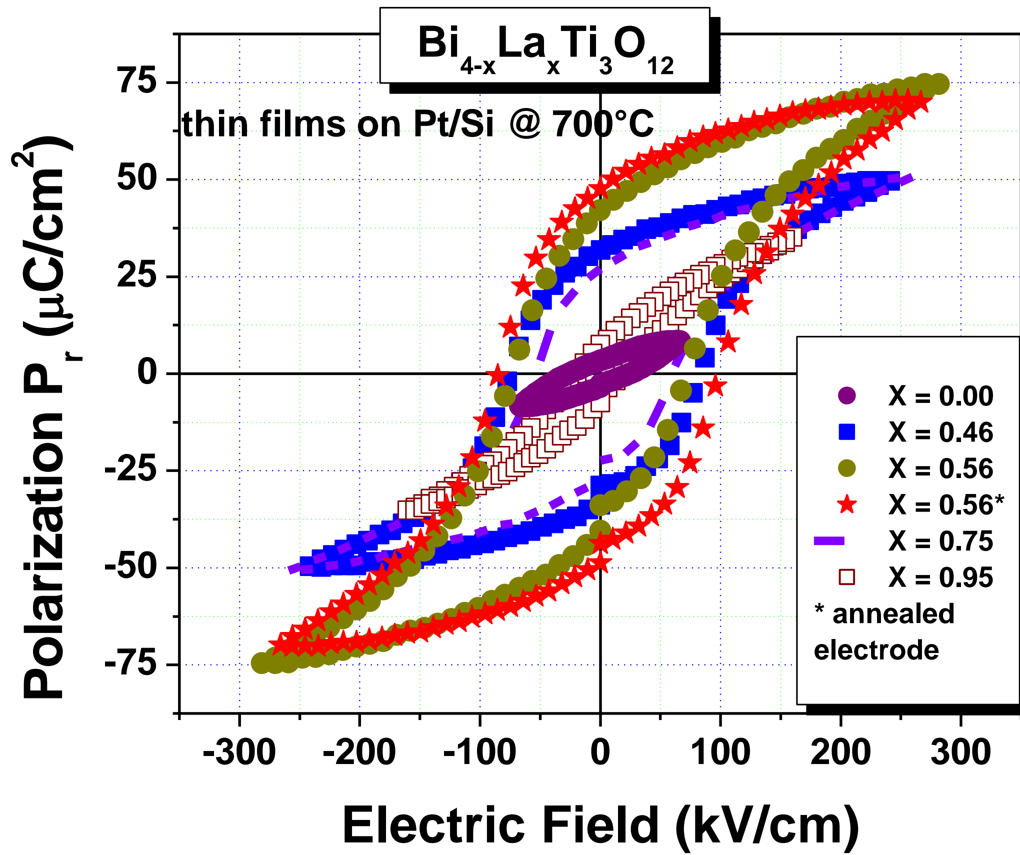

Figure 3.7. a) Superposition of Ferroelectric response of the $Bi_{4-x}La_xTi_3O_{12}$ thin films for x = 0.00, 0.46, 0.56, 0.56 (annealed electrode), 0.75 and 0.95, on Pt ($Pt/TiO_2/SiO_2/Si$) substrate at 700°C.

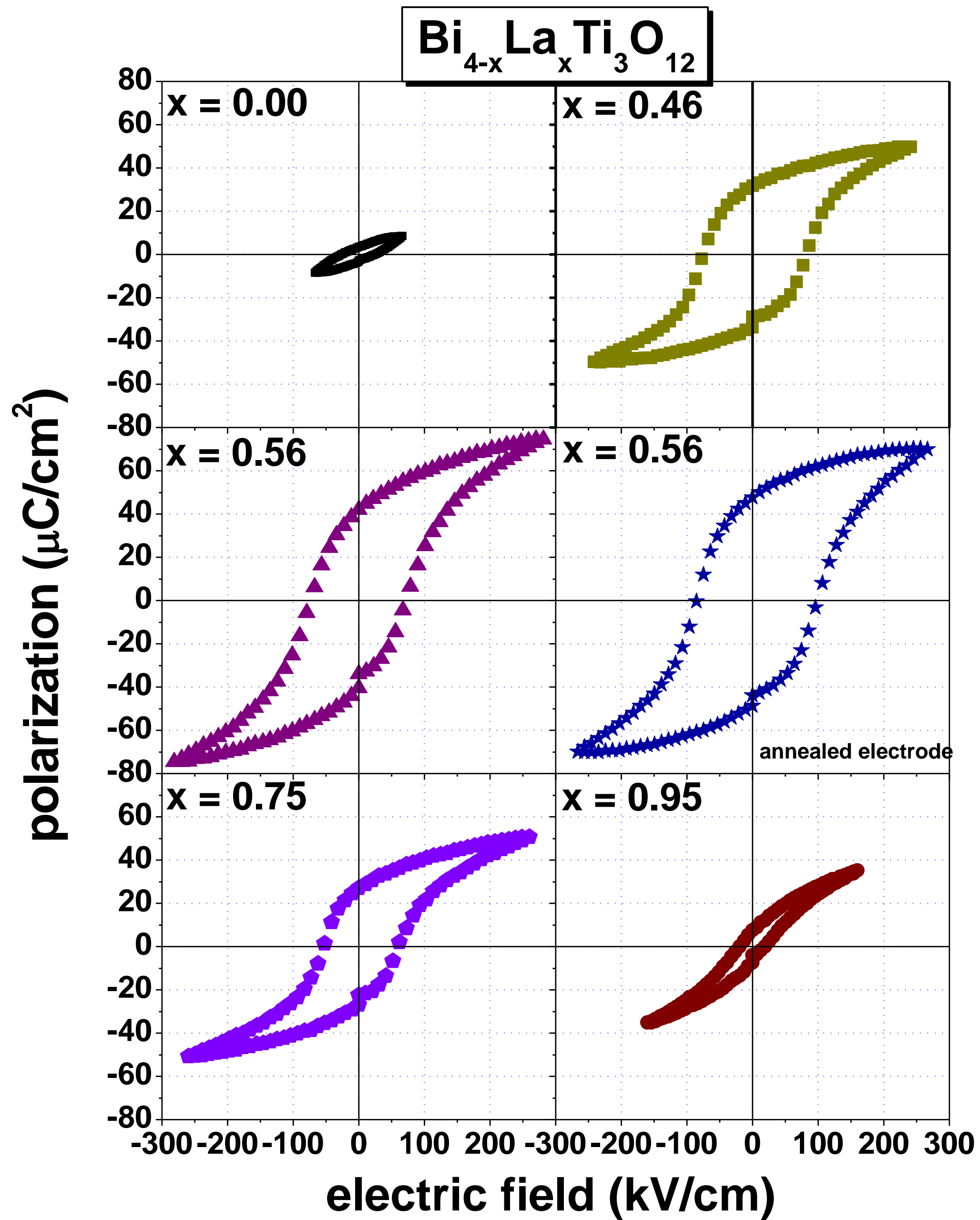

Figure 3.7. b) Separate ferroelectric response of the $Bi_{4-x}La_xTi_3O_{12}$ thin films for x = 0.00, 0.46, 0.56, 0.56 (annealed electrode), 0.75 and 0.95, on Pt ($Pt/TiO_2/SiO_2/Si$) substrate at 700°C.

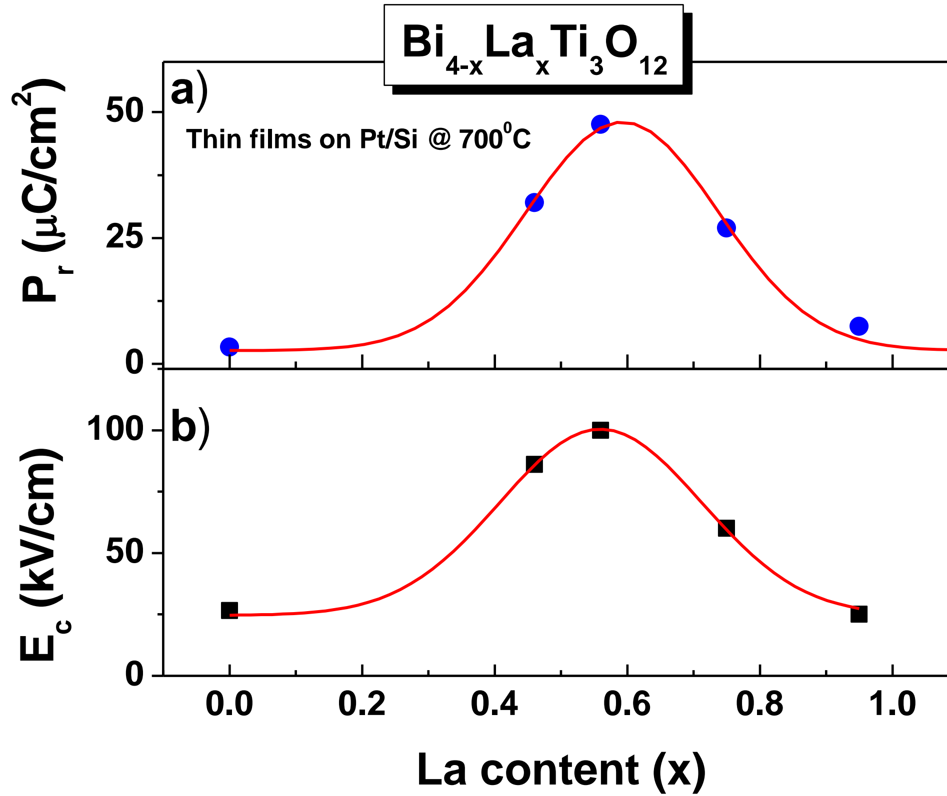

Figure 3.8. The values of a) the remnant polarization (P_r) and b) the coercive field (E_c) of the $Bi_{4-x}La_xTi_3O_{12}$ thin films for x = 0.00, 0.46, 0.56 (annealed electrode), 0.75, and 0.95, on Pt ($Pt/TiO_2/SiO_2/Si$) substrate at 700°C.

thereafter. These results indicate that the substitution of La for Bi in $Bi_4Ti_3O_{12}$ crystals substantially increases the P_r value and that there is a critical La-concentration above which the P_r decreases again. This occurs in $Bi_{4-x}La_xTi_3O_{12}$ when near to ferroelectric-paraelectric phase transition at room temperature with increase x composition in the sample. The giant polarization ($2P_r$ = 95 μC/cm^2) observed in x = 0.56 (annealed electrode) is remarkable in a sense that $2P_r$ of the Pulsed Laser Deposition grown BLT is only 24 μC/cm^2 [6]and that of the highly c-axis oriented is 33 μC/cm^2 [28].

Due to the difference in ionic diameters of La (r(La^{3+}) = 1.36Å)[29] in the pseudoperovskite layer of La^{3+} substituted $Bi_4Ti_3O_{12}$, and the results above cited suggest a tilt in the TiO_6 octahedra that contributed to the development of P_s (spontaneous polarization) along the *c axis* that was demonstrated for Chon.[30] But we believe that the giant polarization in preferred (117) orientation $Bi_{3.44}La_{0.56}Ti_3O_{12}$ thin films, result by the contribution of both *a*-axis polarization and *c*-axis polarization component.

The polarization switching behavior of $Bi_{3.44}La_{0.56}Ti_3O_{12}$ thin film before and after fatigue is showed in figure 3.9 (a) shows the P-E hysteresis loop of the ferroelectric optimized Pt/(117) oriented $Bi_{3.44}La_{0.56}Ti_3O_{12}$/Pt capacitor before and after 1.4 x 10^9 cycles of polarization switching using 100 kHz triangular wave, which showed polarization P_r = 47.7 μC/cm^2 and coercive field Ec = 112 kV/cm for a maximum applied electric field of 282 kV/cm. After 1.4 x 10^9 switching cycles, 15.3 % degradation of P_r is observed in the film. Furthermore, no significant change in the shape of the hysteresis loops was observed even after 1.4x10^9 switching cycles. Before fatigue the film has

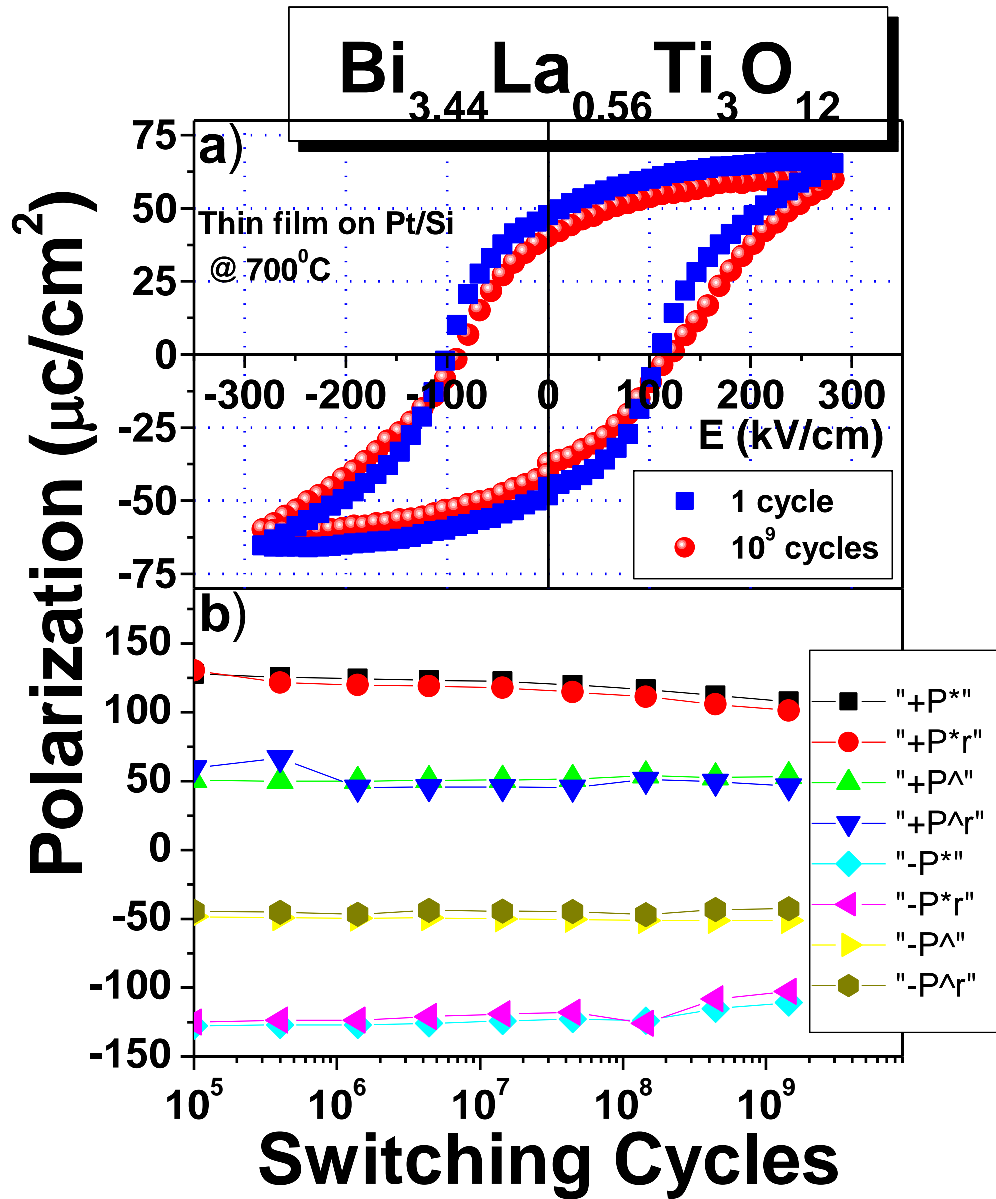

Figure 3.9. a) Ferroelectric response of the $Bi_{3.44}La_{0.56}Ti_3O_{12}$ thin film deposited on Pt ($Pt/TiO_2/SiO_2/Si$) substrate and annealed at 7000C, for 1 cycle and after fatigue $1.4x10^9$ cycles. b) Fatigue characteristics of the $Bi_{3.44}La_{0.56}Ti_3O_{12}$ film under $1.4x10^9$ cycles at a frequency of 1 MHz.

positive imprint (internal bias impede positive polarization switching). After $1.4x10^9$ cycles pulse the imprint is significantly increased. The imprint makes $-E_c$ switching easier and $+E_c$ switching difficult. The switchable and saturation polarization remain almost unaltered. Figure 3.9(b) shows the pulse fatigue characteristics. A triangular waveform of 100 kHz frequency with electric field (282 kV/cm) was used to measure the fatigue test, under 1.4×10^9 cycles at a frequency of 1 MHz. All memory testing parameters (P^*, P_r^*, $\hat{P}$, $\hat{Pr}$, etc) have excellent fatigue resistance up to $1.4x\ 10^9$cycles of the $Bi_{3.44}La_{0.56}Ti_3O_{12}$. After $1.4x10^9$ switching cycles, the polarization was affected by the charge aggregation on the domain wall;[31,32] then, polarization fatigue was caused because of the aggregated charge screen of the electric field. Drift and aggregation of oxygen vacancies have been proposed to result in polarization fatigue. The results imply that there is a low accumulation of vacancies at interfaces with electrodes, space-charge buildup, and domain pinning.[32-34]This result indeed excellent fatigue resistance in $Bi_{3.44}La_{0.56}Ti_3O_{12}$ thin film.

3.3.4 Dielectric properties of $Bi_{4-x}La_xTi_3O_{12}$ thin films

Figure 3.10 a) shows the variation of dielectric constant (K) and loss (tan δ) with applied electric field at 1 MHz. The typical butterfly shape of the measured dielectric constant-electric field, clearly indicate the ferroelectric nature of $Bi_{3.44}La_{0.56}Ti_3O_{12}$ thin films. The peak was observed at about ± 100 kV/cm, which corresponded to positive and negative coercive fields. The dielectric constant and the dissipation factor (tan δ) of the $Bi_{3.44}La_{0.56}Ti_3O_{12}$ film capacitor were measured at 25^0C as a function of frequency. As

shown in Fig. 3.10 b), The Dielectric constant and the dissipation factor are 535 and 0.09 at a frequency of 1 MHz, respectively. These values are comparable to those of LBT, PZT and SBT capacitors[6,35,36]. Although the dielectric constant decreases steadily with increasing frequency, there is no sudden change in its value up to 1 MHz. The dissipation factor (tan δ) shows little change with increasing frequency up to 1 MHZ. All these indicate that the observed ferroelectric response of the $Bi_{4-x}La_xTi_3O_{12}$ capacitor mostly originates from the ferroelectric polarization switching of bound charges, not form the response of freely moving charges. The frequency dispersion characteristics of dielectric constant and loss tangent in Fig.3.10 b) unambiguously indicate that $Bi_{3.44}La_{0.56}Ti_3O_{12}$ film have large distribution of relaxation time associate with polarize species. Since the range of frequency measurement is relatively low in the case presented, the dispersion is probably due to species with large masses. The most likely source of massive dipoles in these materials is abundance of oppositely charged species in the form of Bi and oxygen vacancy that can form during the high temperature process steps. The dipole concentration, for example, Bi and oxygen vacancy pairs, would depend on the processing conditions. A distribution in relaxation time is expected if the dipoles find themselves in varying environments due to random disorder in the sample. Hence, the presence of random disorder, whose degree is dependent on processing conditions, would give rise to dispersion in dielectric properties. Since the conversion of as deposited amorphous phase to layered Aurivillius phase involves the random nucleation of intermediate phases (e.g., fluorite), large number of defective regions develop in thin films. These defective regions don not have the opportunity to relax since the temperature

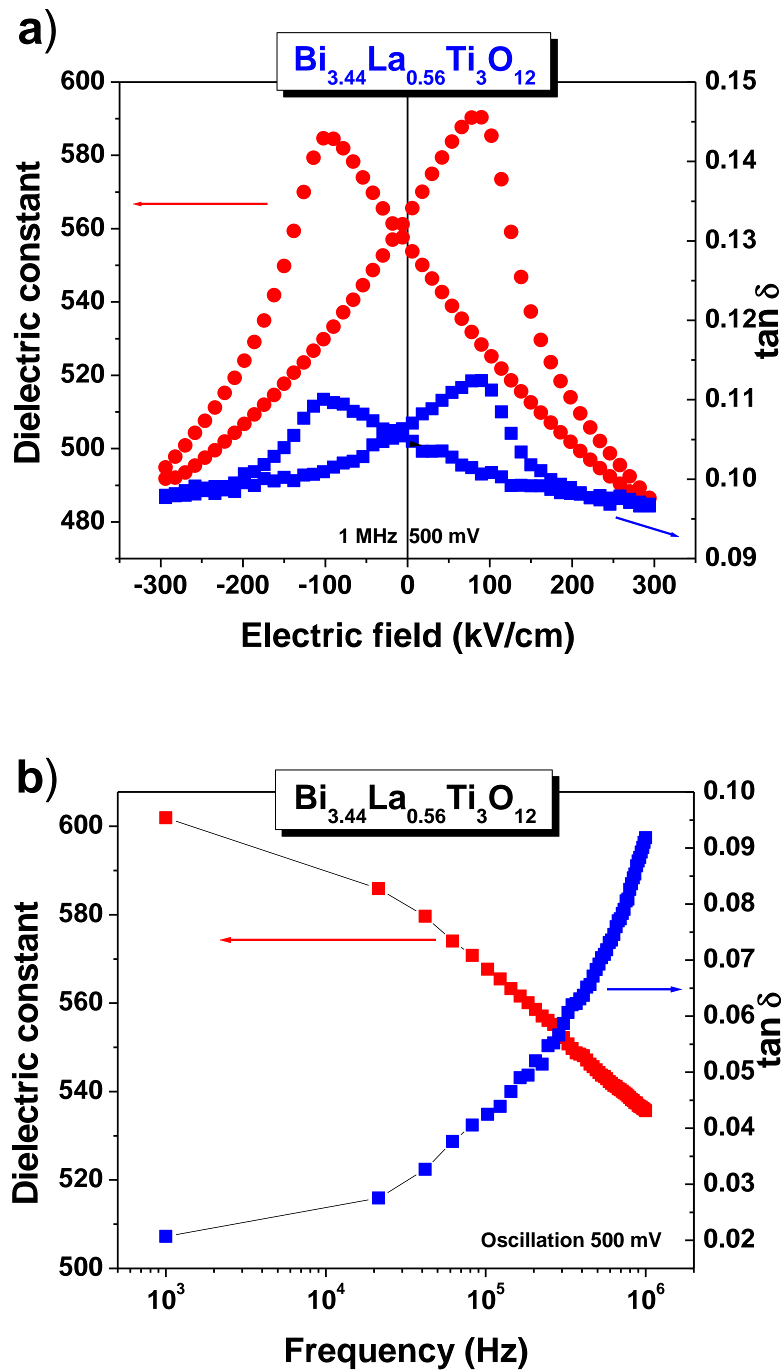

Figure 3.10. a) Dielectric constant and loss (tan δ) vs applied electric field on $Bi_{3.44}La_{0.56}Ti_3O_{12}$ film at 1 MHz, and b) dielectric constant measured at 25^{0}C as a function of frequency in the range between 1 kHz and 1 MHz.

is not sufficient for defect migration and annihilation. It can be observed from frequency dispersion measured values shown in Fig. 3.10 b) that the loss tangent (tan δ) at higher frequencies is about 9% which is comparable with the well established ferroelectric materials such as ferroelectric lead zirconate titanate and SBT.

3.3.5 Leakage current properties of $Bi_{4-x}La_xTi_3O_{12}$ thin films

Figure 3.11 shows steady state dc conductivity, i.e. room temperature leakage current density (J) versus electric field (E) characteristics of $Bi_{4-x}La_xTi_3O_{12}$ (BLT) films on Pt ($Pt/TiO_2/SiO_2/Si$) substrate for the compositions: x = 0.00, 0.46, 0.56, 0.75, 0.95 and 1.50 by Sol-Gel route and spin coating. The voltage step and delay time were kept at 0.2 V and 10 s respectively. The general feature of J-E characteristics is the linear increase of leakage current under low fields and at the certain intermediate field, point of inflexion is clearly observed in each composition of BLT films. At higher fields, current appears to follow a power law ($J = kE^{\alpha}$) and then dielectric breakdown occurs. Because, film is thick (~ 0.50 μm), tunneling phenomena can be ruled out, and the non-linear ohmic conduction due to Poole-Frenkel current (Ln J vs $E^{1/2}$) was plotted and the absence of linearity between these parameters eliminates that mechanism. The general characteristics of the J-E, namely a linear regime followed by a power law, gave evidence of current injection due to space-charge-limited conduction (SCLC)[37] It is important, to note that pure $Bi_4Ti_3O_{12}$ films show larger leakage current in comparison with the BLT films. One can also observe in Fig. 3.11 that for x = 0.56 composition, shows lowest leakage current (~ 10^{-7} A/cm^2) and for x = 1.50 composition leakage current follows

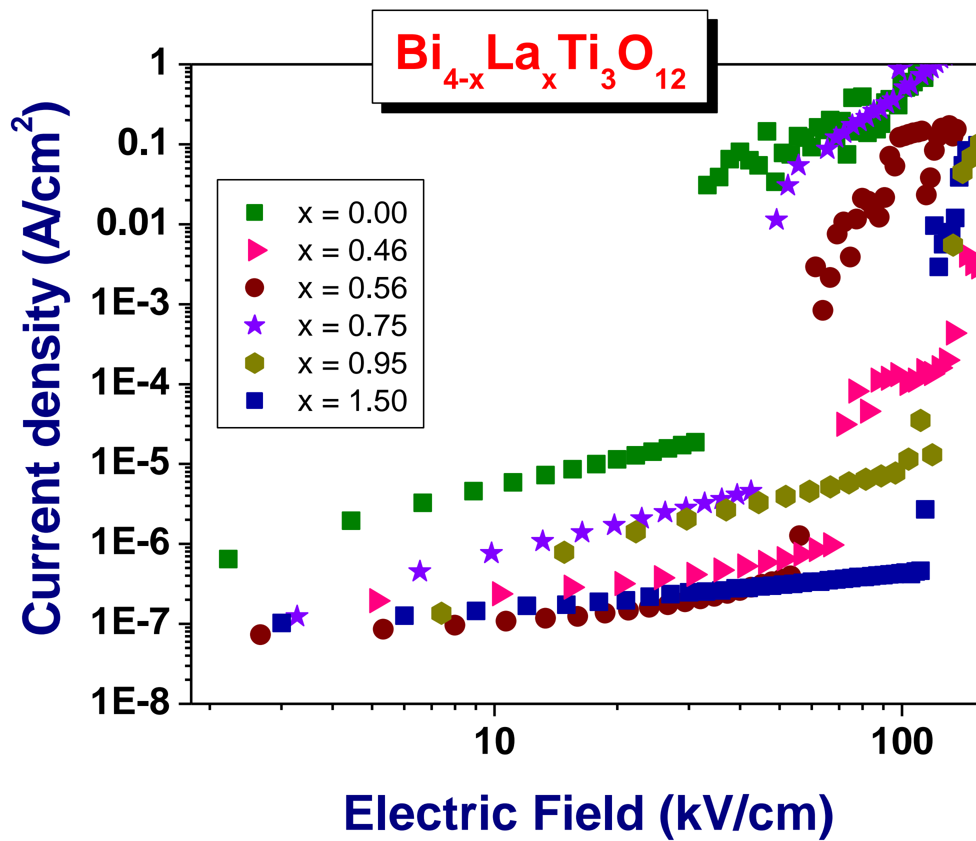

Figure 3.11. Leakage current at room temperature of the $Bi_{4-x}La_xTi_3O_{12}$ thin films deposited on Pt ($Pt/TiO_2/SiO_2/Si$) substrate and annealed at 700°C for the compositions: x = 0.00, 0.46, 0.56, 0.75, 0.95 and 1.50.

ohmic behavior even at higher applied field. In dielectrics, the low fields region, current flows in the film is controlled by the bulk i.e. ohmic behavior, and in intermediate fields, grain boundary regions may be effective, and under very high fields, space charge limited current (SCLC) and electrode-film interfacial resistance may dominate. But, in the case of BLT for most compositions films, dielectric breakdown occurs at higher field. These results suggest that La substitution is effective for improving the chemical stability of oxygen in the perovskite layers. Since charge neutrality is satisfied in the lattice, the higher stability of oxygen leads to fewer Bi (A site) vacancies in the BLT lattice. Therefore, the lower leakage current results from La preventing Bi from evaporating, and the higher leakage current is due to the evaporation of Bi during annealing which is the reason why the purity $Bi_4Ti_3O_{12}$ films exhibited a higher leakage current at room temperature. In fact, for the BLT films with x = 0.56, La substituted BTO results in a much larger P_r, than that of pure $Bi_4Ti_3O_{12}$ and a marked improvement in the leakage current (3.9 x 10^{-7} A/cm^2 at electric field of the 53 kV/cm) properties. This implies that La substituted BTO leads to efficient decrease in space charge density. The measured leakage current densities in 10^{-7} - 10^{-8} A/cm^2 are comparable with the leakage current in PZT and SBT films.

3.4. Conclusions

$Bi_{4-x}LaxTi_3O_{12}$ thin films were grown on Pt ($Pt/TiO_2/SiO_2/Si$) substrates by Sol-Gel process and spin coating. All of the BLT films consist of a single phase of a bismuth-layered structure and have small grains of arbitrary shape with preferred (117)

orientation, shows complete solid solution up to the composition $x \leq 1.50$. It seems probable that the BLaT undergoes a ferroelectric-paraelectric phase transition at $x \approx 1.0$ at room temperature. At an applied voltage of 266 kV/cm, the remanent polarization and the coercive field of the BLT film with x = 0.56 annealed at 700°C are about 47.5 μC/cm^2 and 100 kV/cm, respectively. At lower field, the leakage current is dominated by ohmic behavior in BLT films. However, after 1.4 x 10^9 switching cycles, not show any significant fatigue at a frequency of 1 MHZ, in the film with x = 0.56. Also, the measured dielectric loss was observed to be less than 9% at 1MHz. The results on the structural, ferroelectric and dielectric properties of $Bi_{4-x}LaxTi_3O_{12}$ indicate that they are important new candidate for nonvolatile random access memory devices.

3.5 References

1. J.F.Scott and C.A. Araujo, Science, **246**, 1400 (1989).
2. S. H. Kim, C. Y. Koo, D. Y. Park, D. S. Lee, J. H. Yeom, J. Lim, C. S. Hwang and J. Ha, J. Korean Phys. Soc. **42**, S1417 (2003).
3. K. Lee, H. S. Choi, J. H. Lee, Y. M Jang and I. H. Choi, J. Korean Phys. Soc. **40** 733 (2002).
4. H. N. Lee, A. Visinoiu, S. Senz, C. Harnagea, A. Pignolet, D. Hesse and U. Gösele, J. App. Phys. 88, 6658 (2000).
5. S. Bhattacharyya, A. Laha and S.B. Krupanidhi, J. App. Phys. **92**, 1056 (2002).
6. B. H. Park, B. S. Kang, S. D. Bu, T. W. Noh, J. Lee and W. Jo, Nature (London) **401**, 682 (1999).
7. Y. Ding, J. S. Liu, H. X. Qin, J. S. Zhu and Y. N. Wang, Appl. Phys. Lett. **78**, 4175 (2001).
8. R. W. Whatmore, P. L. Osbond and N. M. Shorrocks, Ferroelectrics **76**, 351 (1987).

9. U. Chon, G. -C. Yi, and H. M. Jang, Appl. Phys. Lett. 78, 658 (2001).

10. R.E. Melgarejo, M. S. Tomar, S. Bhaskar, P. S. Dobal, and R. S. Katiyar, Appl. Phys. Lett. **81**, 2611 (2002).

11. M. S. Tomar, R. E. Melgarejo A. Hidalgo, S. B. Majumder and R. S. Katiyar, Appl. Phys. Lett. **83**, 341 (2003).

12. R. E. Melgarejo and M.S. Tomar, Mat. Res. Soc. Symp. Proc. **784**, 219 (2004).

13. Y. Shimakawa, Y. Kubo, Y. Nakagawa, T. Kamiyama, H. Asano and F. Izumi, Phys. Rev. B 61, 6559 (2000).

14. B. Aurivillius, Ark. Kemi **1**, 463 (1950); **1**, 499 (1950); **2**, 519 (1951).

15. E. C. Subbarao, Phys. Rev. **122**, 804 (1961).

16. T. W. Noh, B. S. Kang, Y. W. So, B. H. Park and S. D. Bu, J. Korean Phys. Soc. **39**, S35 (2001).

17. B. S. Kang, H. H. Park, S. D. Bu, T. W. Noh, J. Lee, H. –D. Kim and T. H. Kim, J. Korean Phys. Soc. **35**, S1306 (1999).

18. D. Cullity, *Elements of X-ray diffraction* (Addition-wesley publishing Co., Inc USA, 1967) p 261.

19. P. R. Graves, G. Hua, S. Myhra, and J. G. Thompson, J. Solid State Chem. 144, 112 (1995).

20. S. Kojima, R. Imaizumi, S. Hamazaki, and M. Takaahige, Jpn. J. Appl. Phys. **33**, 5559 (1994).

21. M. Osada, M. Tada, M. Kakihama, T. Watanabe, and H. Funakubo, Jpn. J. Appl. Phys. Part 1, **40**, 5572 (2001).

22. S. Kojima and S. Shimida, Physica, **B 219-220**, 617 (1996).

23. Y. Shimakawa, Y. Kubo, Y. Tauchi, H. Asano, F. Izumi, and Z. Hiroi, Appl.Phys. Lett.**79**, 2791 (2001).

24. R. L. Withers, J. G. Thompson and A. D. Rae, J. Solid State Chem. **94**, 404, (1991).

25. C. H. Hervoches and P. Lightfoot, J. Solid State Chem. **153**, 66, (2000).

26. W. Cochran, Adv. Phys. **9**, 387 (1960).

27. M. Osada, M. Tada, M. Kakihana, T. Watanabe, and H. Funakubo, Jpn. J. Appl. Phys. **40**, 5572 (2001).

28. U. Chon, H. M. Jang and I. W. Park, Solid State Commun. **127**, 469 (2003).

29. R.D. Shannon , Acta Crystallogr., Sect A: Cryst. Phys.,Diffr., Theor. Gen.

30. U. Chon, H. M. Jang, M. G. Kim, and C. H. Chang, Phys. Rev. Lett. **89**, 87601-1 (2002).

31. D. Wu, A. Li, T. Zhu, Z. Liu and N. Ming, J. Appl. Phys. **88**, 5941 (2000).

32. Y. Noguchi, I. Miwa, Y. Goshima and M. Miyayama, Jpn. J. Appl. Phys. 39, L1259 (2000).

33. X. Du and I-W. Chen, J. Am. Ceram. Soc. **81**, 3253 (1998).

34. Y. Noguchi and M. Miyayama, Appl. Phys. Lett. **78**, 1903 (2001).

35. H. D. Chen, K. R. Udayakumar, C. J. Gaskey and L. E. Cross, Appl. Phys. Lett. 67, 3411 (1995).

36. R. Dat, J. K. Lee, O. Auciello and A. I. Kingon, Appl. Phys. Lett. 67, 572 (1995).

37. P. C. Joshi, S. B. Krupanidhi, J. Appl. Phys. 73, 7627 (1993).

Chapter 4

Studies of $Bi_{4-x}Nd_xTi_3O_{12}$ for ferroelectric devices

In this chapter, we report the results on $Bi_{4-x}Nd_xTi_3O_{12}$ (BNdT) thin films prepared by sol-gel process. They showed high polarizations and fatigue free response. The effects of Nd-ion substitution on the structural and the ferroelectric properties of the BNdT thin films were investigated.

4.1. Experimental Details

The precursor solutions for $Bi_{4-x}Nd_xTi_3O_{12}$ (with x = 0.00, 0.36, 0.46, 0.56, 0.75, 0.85, 1.00 and 2.00) were bismuth nitrate pentahydrate, neodymium nitrate hexahydrate, and titanium isopropoxide. Bismuth nitrate pentahydrate and neodymium nitrate hexahydrate. The details of the sol preparation are described in the experimental section of chapter 2, section 2.3.2.

For the fabrication of the NdBTO thin films, the diluted sol (0.3M) of the desired composition was used the NdBTO precursor solution was syringed through a 0.2 μm syringe filter onto a $Pt/TiO_2/SiO_2/Si$ substrate. The films were produced by using a spin-coating technique with a spinner operated at 3000 rpm for 30s. To remove the organic contaminations, after the spin-coating procedure, we kept the films on a furnace at 600°C

for 5 min., the coating and firing cycles were repeated required number of times and finally the films were annealed at 700°C for 1 h under air atmosphere for crystallization.

4.2 Result and Discussions

4.2.1 XRD Analysis

Phase analysis was performed using X-ray diffractometer (Siemens D5000) with CuKα radiation (1.5405Å). figure 4.1 shows the X-ray diffraction patterns of $Bi_{4-x}Nd_xTi_3O_{12}$ (BNdTO) thin films on $Pt/TiO_2/SiO_2/Si$ substrate for the compositions x = 0.00, 0.26, 0.46, 0.56, 0.75, 0.85, 1.00 and 2.00. Miller indices are indicated for the diffraction peaks. All of the films consisted of a single phase of a bismuth layered structured showing the preferred (117) orientation. The X-ray diffraction intensity tends to decrease with increasing Nd-content. The crystalline quality of the film can be estimated from the measured Full Width at Half the Maxima (FWHM) of the most intense (117) diffraction peak. Smaller FWHM value indicates better crystallinity of the film. The crystallite sizes of the $Bi_{4-x}Nd_xTi_3O_{12}$ films were calculated using Scherrer formula[1]. Table 4.1 shows that the crystallite sizes decrease as the Nd content increase. This may support the microstructural observation, as done using SEM (scanning electron microscopy), that the average grain size of perovskite BNdT films decreases with increasing Nd-content. The lattice parameters of the $Bi_{4-x}Nd_xTi_3O_{12}$ films were calculated from their X-ray diffractograms. The lattice constants *a, b*, and *c* for BNdT which were estimated from the (006), (200) and (111) Bragg reflection in the XRD patterns, are presented in figure 4.2 where shows the variation of lattice constants of BNdT thin films

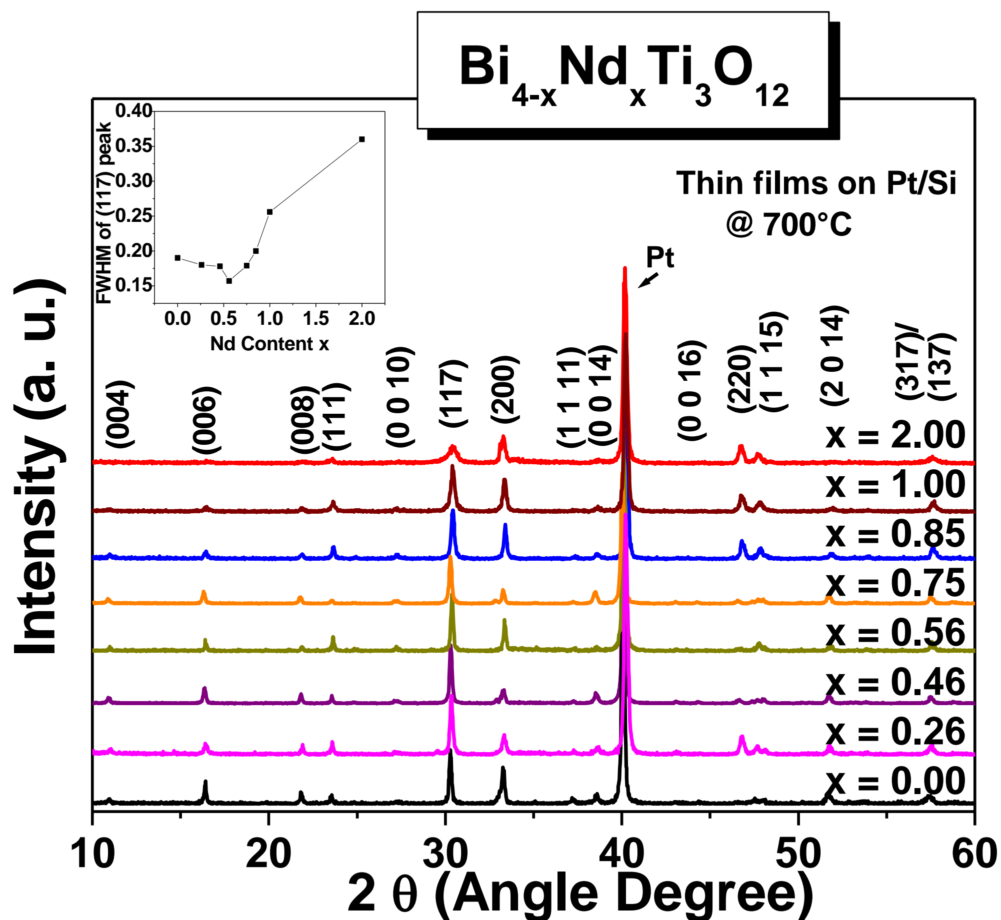

Figure 4.1 X-ray diffraction patterns of $Bi_{4-x}Nd_xTi_3O_{12}$ (NdBTO) thin films on Pt/TiO_2/SiO_2/Si substrate for the compositions x = 0.00, 0.26, 0.46, 0.56, 0.75, 0.85, 1.00 and 2.00, the inset shows the variation of the FWHM of (117) peak with Nd content.

TABLE 4.1 Variation of crystallite size for different Nd content in $Bi_4Ti_3O_{12}$ films

Composition X	Crystallite size (nm)
0.00	62
0.26	54
0.46	56
0.56	51
0.75	48
0.85	36
1.00	33
2.00	19

as a function of Nd content. It is clear that with the partial substitution of Nd^{3+} ion for Bi^{3+} ion, the lattice parameter of *c* increases and the lattice parameters of *a* and *b* decreased. This distortion may mainly attribute to the difference of the ionic radii between Nd^{3+} and Bi^{3+} ions. The slightly change in lattice constants indicates that Nd atoms are dissolved in the BTO lattice systematically. The lattice distortion (a/b ratio) of the orthorhombic phase was smallest in the samples. The crystal structure of neodymium substituted bismuth titanate $Bi_{4-x}Nd_xTi_3O_{12}$, which is considered to be orthorhombic at room temperature with space group symmetry A21am and followed by tetragonal structure in the paraelectric phase with crystal symmetry I4/mmm, consists of a layer structure of $(Bi_2O_2)^{2+}$ and $[(Bi_{2-x}Nd_x)Ti_3O_{10}]^{2-}$ pseudoperovskite layers stacked along the *c*-axis direction. For this structure, the rotation of TiO_6 octahedra in the *a-b* plane accompanied with a shift of the octahedron along the a-axis is largely enhanced by the neodymium element substitution for Bi in the pseudoperovskite layer.[2] The high value of P_r in BNdT thin films can be primarily attributed to this distortion.

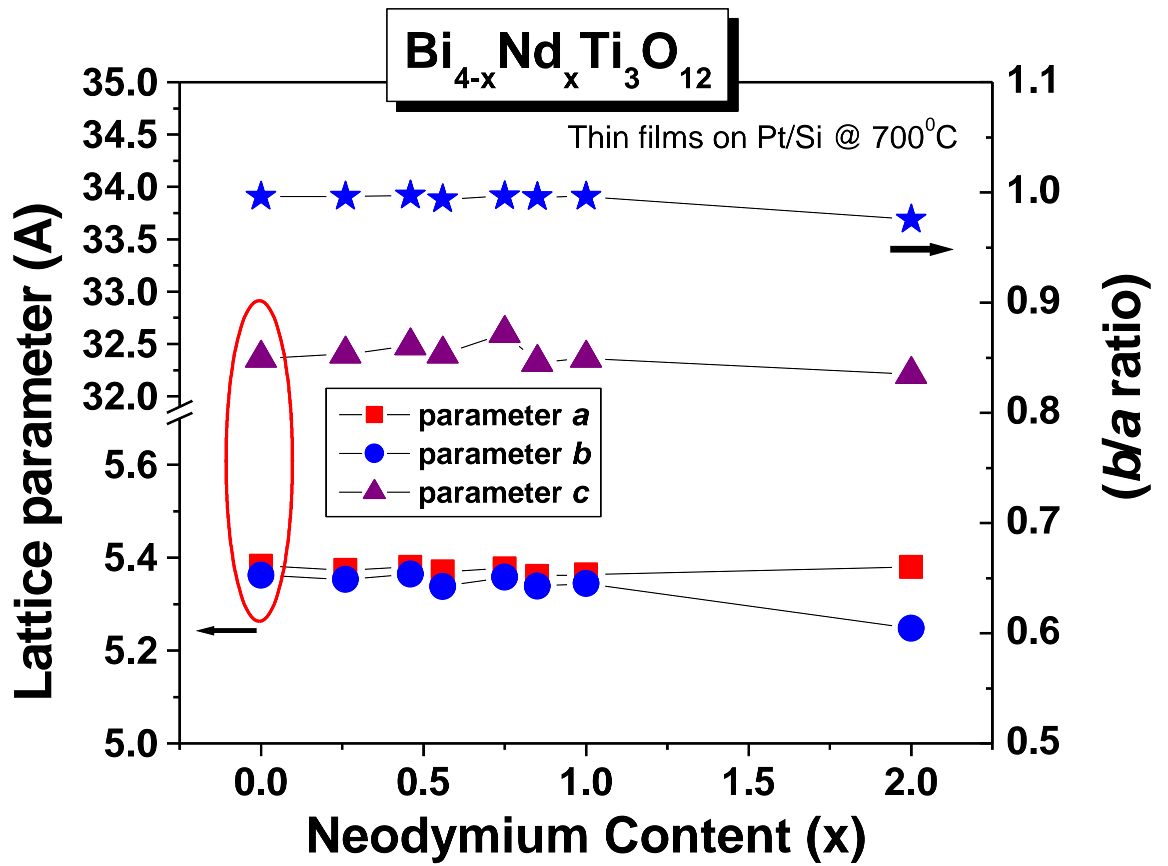

Figure 4.2 Variation in lattice parameters of NdBTO thin films with different Nd content.

Figure 4.4 shows the SEM micrographs of (a) x = 0.00, (b) x = 0.26, (c) x = 40 and d) x = 0.56 Nd substituted BTO thin films on $Pt/TiO_2/SiO_2/Si$ substrates. As shown in micrographs, the grain size of the BTO film is substantially larger than that of the BNdT, because of lower diffusivity of neodymium, the substitution of neodymium for bismuth suppresses the grain growth of BNdT, as observed in figure 4.3 (b), (c) and (d). In Figure 4.3 (a) small grains of arbitrary shape are observed in purity $Bi_4Ti_3O_{12}$. The NdBTO thin films were composed of small rod-like grains. This results suggest that the substitution of Nd^{3+} for Bi^{3+} in BTO films lead to reduction in grain size when the Nd content increase. Thus, the present SEM surface microstructures are consistent with the X-ray diffraction results shown in Fig. 4.1.

4.2.2 Micro Raman analysis

Figure 4.4 shows the room temperature Raman spectra of the polycrystalline BNdT thin films in backscattering geometry using JY T64000 triple-monochromator. An optical microscope with 80X objective was used to focus the 514.5 nm excitation radiation from a Coherent Innova 99 Ar^+ laser and to collect the scattered radiation. The scattered signal was detected by a charge-couple device (CCD) detection system. The Raman selections rules in Aurivillius $Bi_4Ti_3O_{12}$ allow 16 phonon modes of different symmetries ($6\ A_{1g} + 2\ B_{1g} + 8\ E_g$) if a tetragonal structure of the lattice is considered. It consist of Bi_2O_2 layers and perovskite-type structures ($A_{n-1}B_nO_{3n+1}$) with triple TiO_6 octahedra and A site Bi atom. The Bi^{3+} ion in A site is strongly under bonded and Ti^{4+} ion in B site is slightly over bonded. However, different numbers of Raman modes from

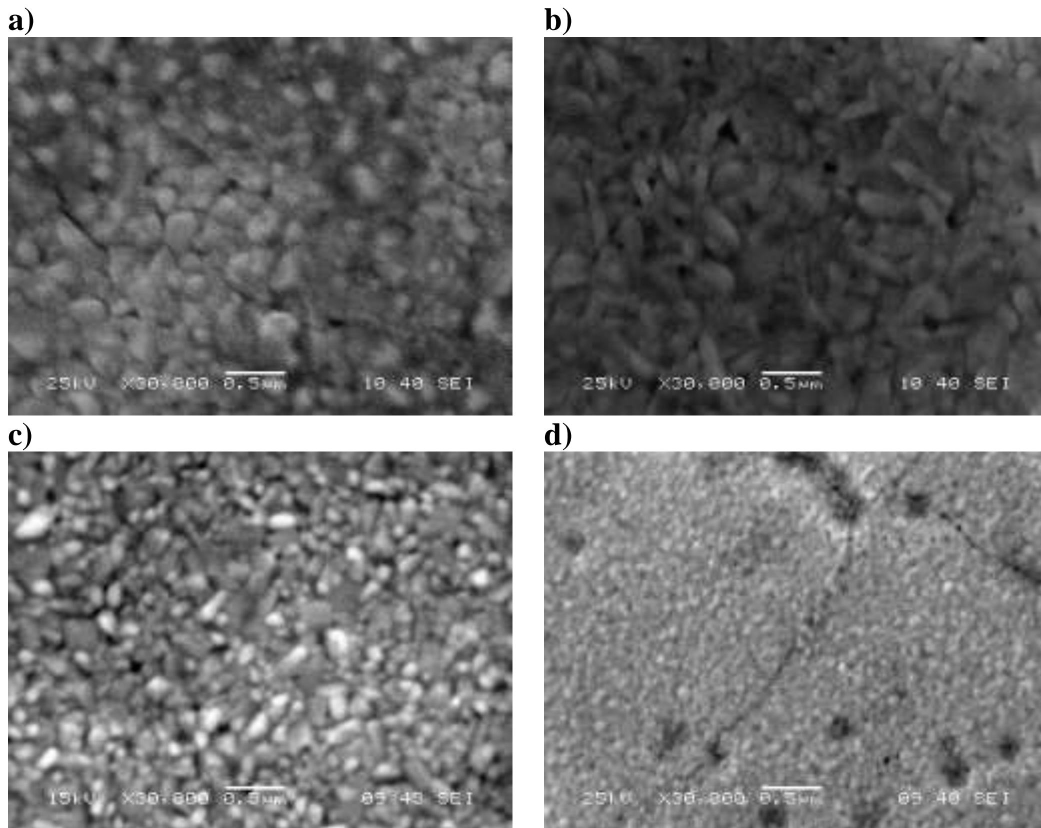

Figure 4.3 SEM micrographs of (a) BTO, (b) x = 0.26, (c) x = 0.40 and d) x = 0.56, Neodymium content in BTO thin films on Pt/TiO_2/SiO_2/Si substrate.

$Bi_4Ti_3O_{12}$ have been reported in the literature[3-4], which can be explained by the possible overlap of the same symmetry vibrations and orthorhombic distortions of the material[4]. Figure 4.4 shows the room temperature recorded Raman spectra of $Bi_{4-x}Nd_xTi_3O_{12}$ films for compositions: x = 0.00, 0.26, 0.46, 0.56, 0.75, 0.85, 1.00 and 2.00. The Raman modes of $Bi_4Ti_3O_{12}$ films are in agreement with those observed in its crystal[3]. The film spectrum exhibits intense phonon modes at about 28, 45, 62, 115, 270, 540 and 850 cm^{-1} and many other weak features. As the vibrational modes strongly depend on the atomic masses, the heavy Bi ions should be responsible for the low frequency modes (ν <100 cm^{-1}). The 62 cm^{-1} mode is known to originate from[3,4] the Bi displacements in Bi_2O_2 layer. The modes at about 270, 540 and 850 cm^{-1} are the internal modes of TiO_6 octahedra having A_{1g} character. The compositional dependence of Raman spectra shows the similar effects on these internal modes they weaken and broaden with increasing content of Nd in films. Such changes are possible as Nd substituted is expected to introduce cationic disorder even though there is only a small difference in the ionic radii of Bi^{+3} and Nd^{+3} ions. The 150 cm^{-1} mode gradually shifts to higher frequency with increasing intensity as the Nd content in films increases. This mode can be assigned to the A_{1g} character involving A-site Bi vibrations. Most prominent effect of Nd substituted was observed on the low frequency modes. The Raman frequencies were obtained for each composition by fitting the peaks with the damped harmonic oscillator-type phonon functions Nd are plotted in figure 4.5. The lowest frequency (28 cm^{-1}) mode, which has been assigned as a soft-mode responsible for a phase transition at 675°C, shows softening behavior with Nd substituted. Compared to the soft mode, a little variation in the 32 cm^{-1} mode and the

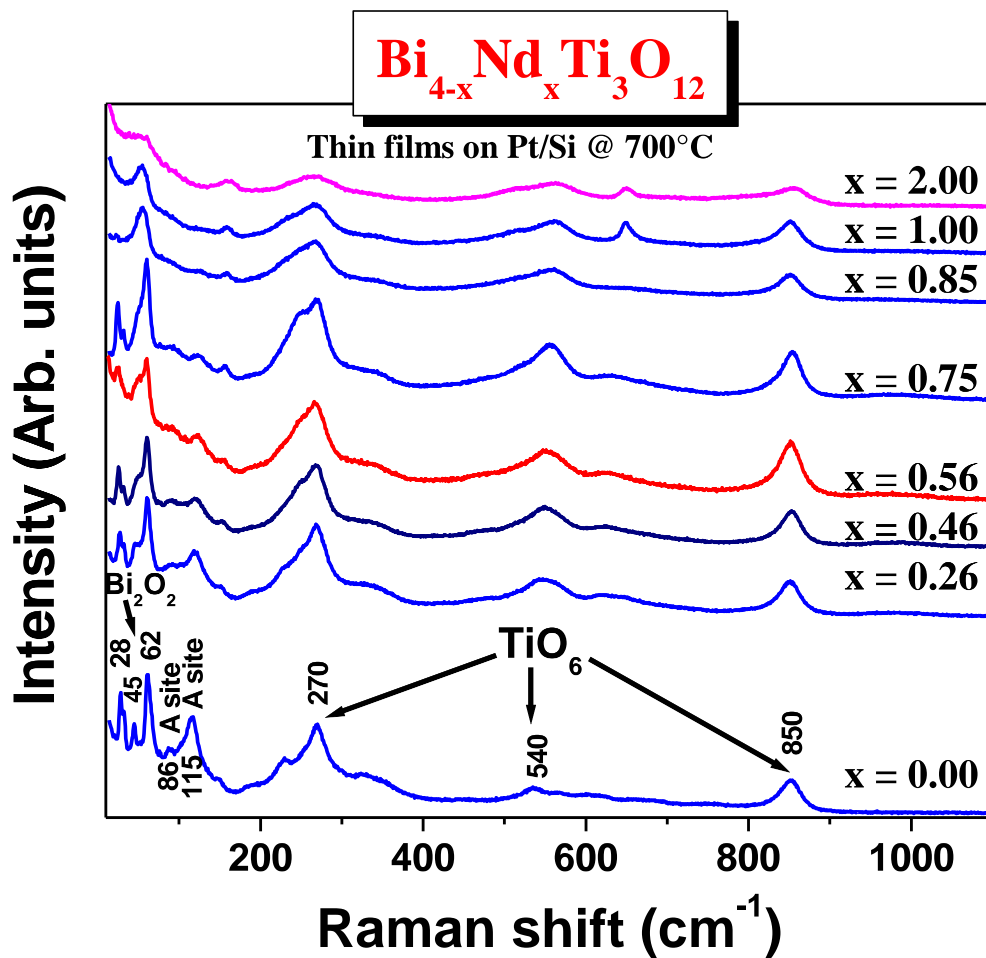

Figure 4.4. Room temperature Raman spectra of $Bi_{4-x}Nd_xTi_3O_{12}$ films on a Pt substrate ($Pt/TiO_x/SiO_2/Si$) for x = 0.00, 0.26, 0.46, 0.56, 0.75, 0.85, 1.00 and 2.00 composition. The indexes in the figure indicate peculiar modes to the local structures.

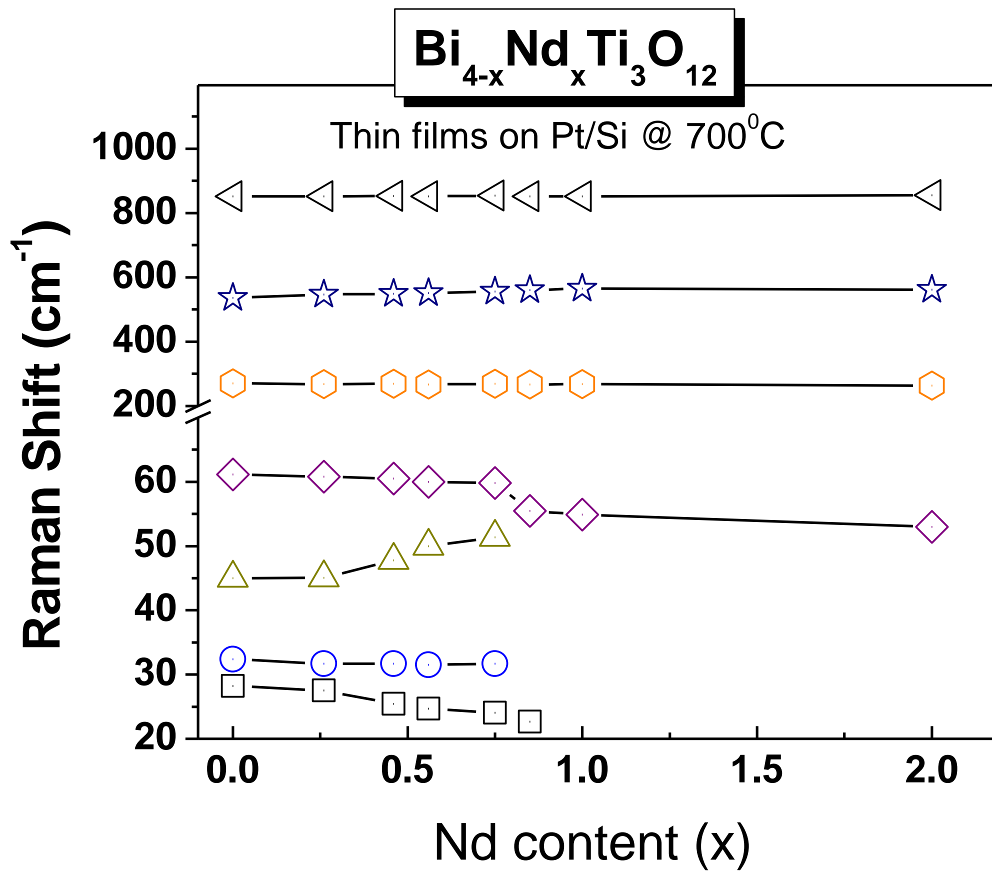

Figure 4.5. Raman frequencies as a function of Neodymium compositions in $Bi_{4-x}Nd_xTi_3O_{12}$ thin films.

62 cm^{-1} mode suggest that the substituted process least affects the Bi_2O_2 layers. If Nd substitutes Bi on the A-sites of the lattice, an increase in the mode frequency is expected from the mass difference as Bi is 1.45 times heavier than Nd. With increasing neodymium content, the A site mode shown in Fig. 4.4 shifted toward higher frequencies up to x = 0.75 then, start the incorporation of neodymium into Bi_2O_2 site. The up-shift of 45 cm^{-1} mode with increasing Nd composition rules out its origin in Bi_2O_2 layers. This 45 cm^{-1} mode merges with the 62 cm^{-1} mode at x = 0.85. Additionally, vanishing of the low frequency modes (ν = 28, 32, 115 cm^{-1}) as well as a small but abrupt change in the TiO_6 octahedral frequencies around x = 0.85 reflects a compositional induced structural transition in $Bi_4Ti_3O_{12}$ at that composition. For x > 0.85, a mode around 650 cm^{-1} has been shown to exhibit A_{1g} character by Graves *et al.*[3] and has been associated with the Ti-O symmetric stretch in $Bi_4Ti_3O_{12}$ crystal. It is possible that the orthorhombic distortions relax for higher Nd-substituted samples, intensifying 650 cm^{-1} oscillation. Since Nd substituted on A sites should least affect the TiO_6 octahedral frequencies, the 650 cm^{-1} mode could not be associated with the substituting.

4.3.3. Ferroelectric properties of $Bi_{4-x}Nd_xTi_3O_{12}$ thin films

For ferroelectric measurements, the top circular electrodes of platinum 200 nm thick and 200 μm diameter were deposited by dc sputtering. Ferroelectric response was recorded by RT6000HVS probe (Radiant Tech.) in virtual ground mode. For comparison, the ferroelectric response for the BNdT films of the compositions x = 0.00, 0.26, 0.36, 0.40, 0.46, 0.56, 0.56 (annealed electrode), 0.75, 0.85 and 1.00 is show in Fig.4.6 (a) and

(b). With post annealing steps of the Pt electrode, a polarization ($2P_r$ ~140 μC/cm^2) for the film with composition x = 0.56 is shown in Fig. 4.6 (a) with coercive field Ec = 150 kV/cm for a maximum applied electric field 412 kV/cm. In un-annealed capacitor structure $2P_r$ ~120 μC/cm^2 is shown in the figure 4.6 (b). For other compositions the polarization is much lower. The effects of the Nd-content on the variation of the remanent polarization (Pr) and the coercive field (Ec) of BNdT thin film were systematically examined at an applied electric field. As presented in figure 4.7, the value of the P_r increases gradually with increasing Nd-content for x below a certain critical level. The P_r shows its maximum value of 70 μC/cm^2 at x = 0.56 (annealed electrode) and decreases thereafter. The E_c increases rather steeply with increasing Nd-content from 48 to 176 kV/cm. The E_c shows its maximum value at x = 0.46 and decreases gradually thereafter. These results indicate that the substitution of Nd for Bi in BTO crystals substantially increases the P_r value parallel to the (117) orientation and that there is a critical Nd-concentration above which the P_r decreases again. The giant polarization ($2P_r$ = 140 μC/cm^2) observed in x = 0.56 (annealed electrode) is remarkable in a sense that $2P_r$ of the sol-gel grown highly c-axis oriented BNdT with x = 0.85 is 103 μC/cm^2 [5] as presented in figure 4.8 for comparison.

Due to the difference in ionic diameters of Nd (r(Nd^{3+}) = 1.27Å)[6] in the pseudoperovskite layer, the calculated values of lattice space $d_{(117)}$ in Nd substituted $Bi_4Ti_3O_{12}$ suggest a tilt in the TiO_6 octahedra[5]. This structural factor and the possibility of dipole formation give rise to the experimentally observed giant ferroelectric polarization[7] in $Bi_{3.44}Nd_{0.56}Ti_3O_{12}$ and large ferroelectric polarization in Nd substituted $Bi_4Ti_3O_{12}$

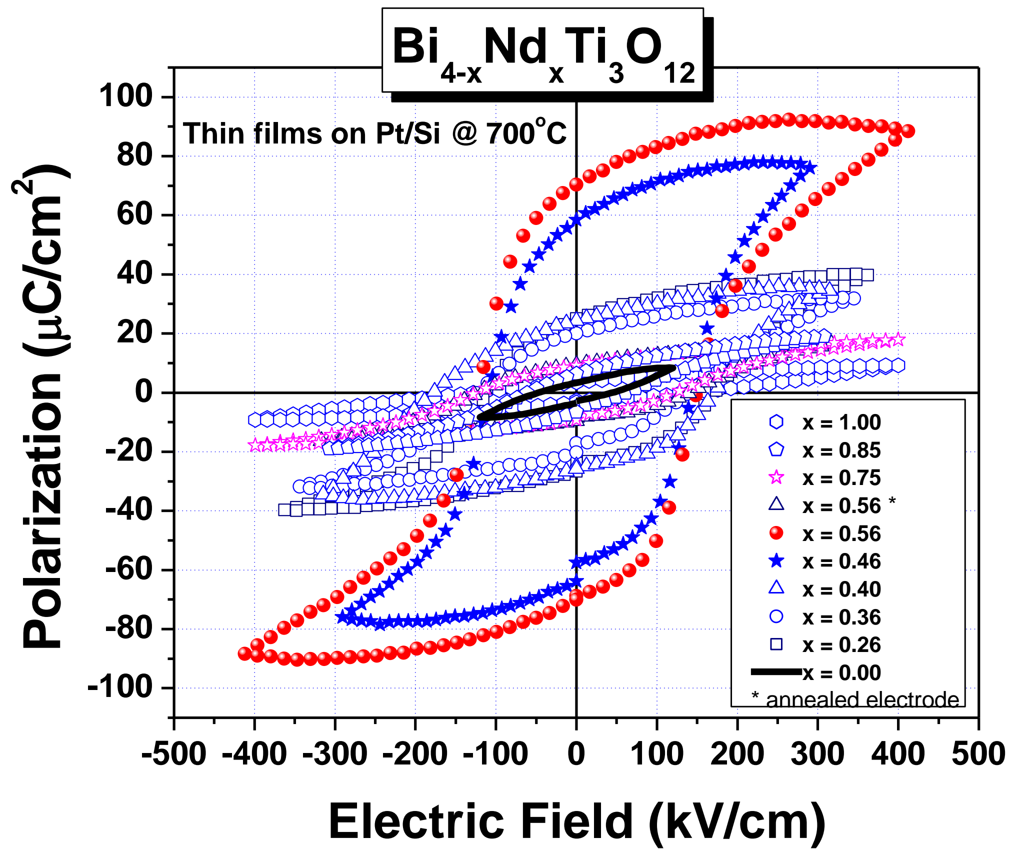

Figure 4.6. a) Ferroelectric response of the $Bi_{4-x}Nd_xTi_3O_{12}$ thin films for x = 0.00, 0.26, 0.36,0.40, 0.46, 0.56, 0.56 (annealed electrode), 0.75, 0.85 and 1.00, on Pt ($Pt/TiO_2/SiO_2/Si$) substrate at 700°C

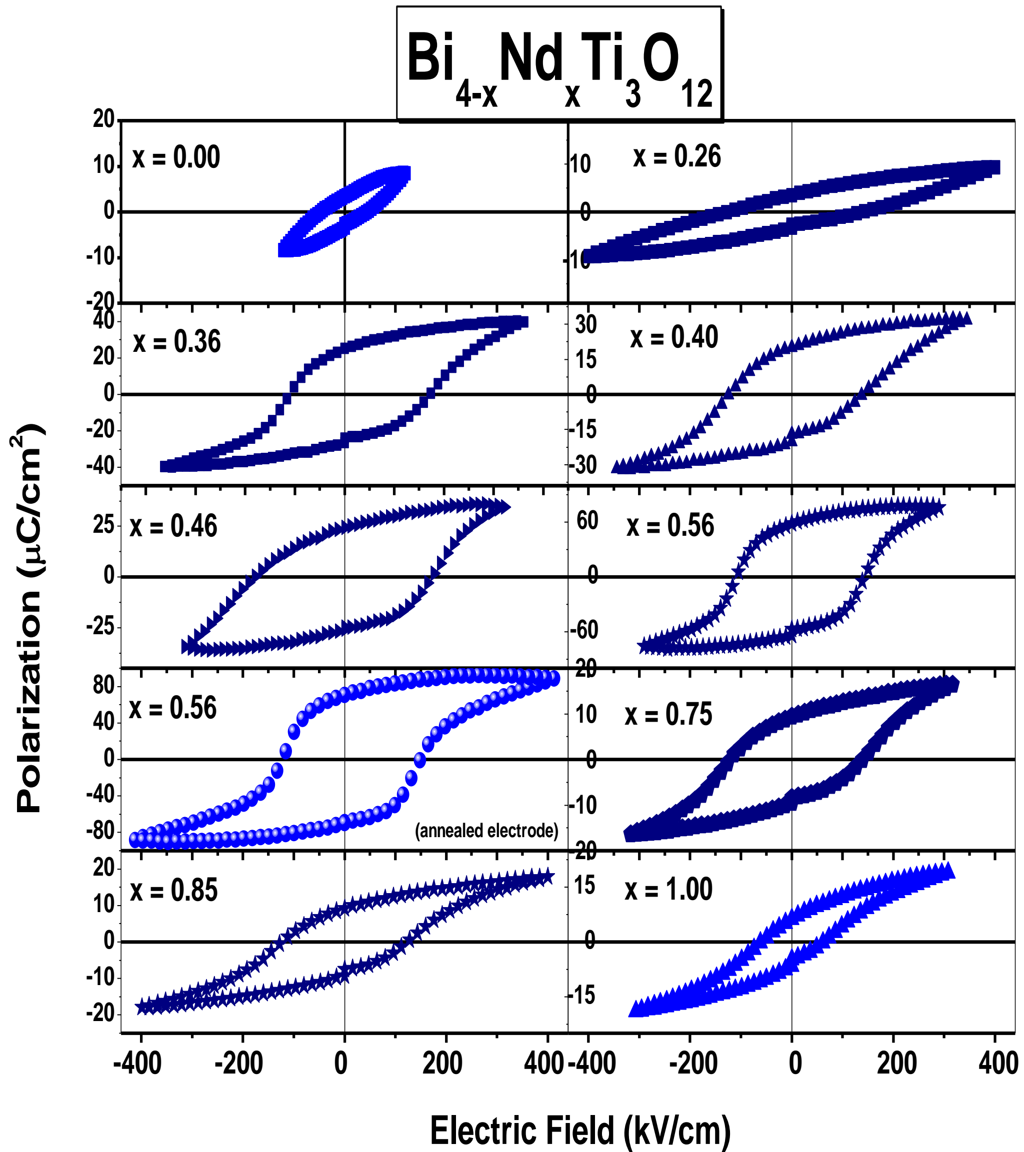

Figure 4.6. b) Separate Ferroelectric response of the $Bi_{4-x}Nd_xTi_3O_{12}$ thin films for x = 0.00, 0.26, 0.36,0.40, 0.46, 0.56, 0.56 (annealed electrode), 0.75, 0.85 and 1.00, on Pt ($Pt/TiO_2/SiO_2/Si$) substrate at 700°C

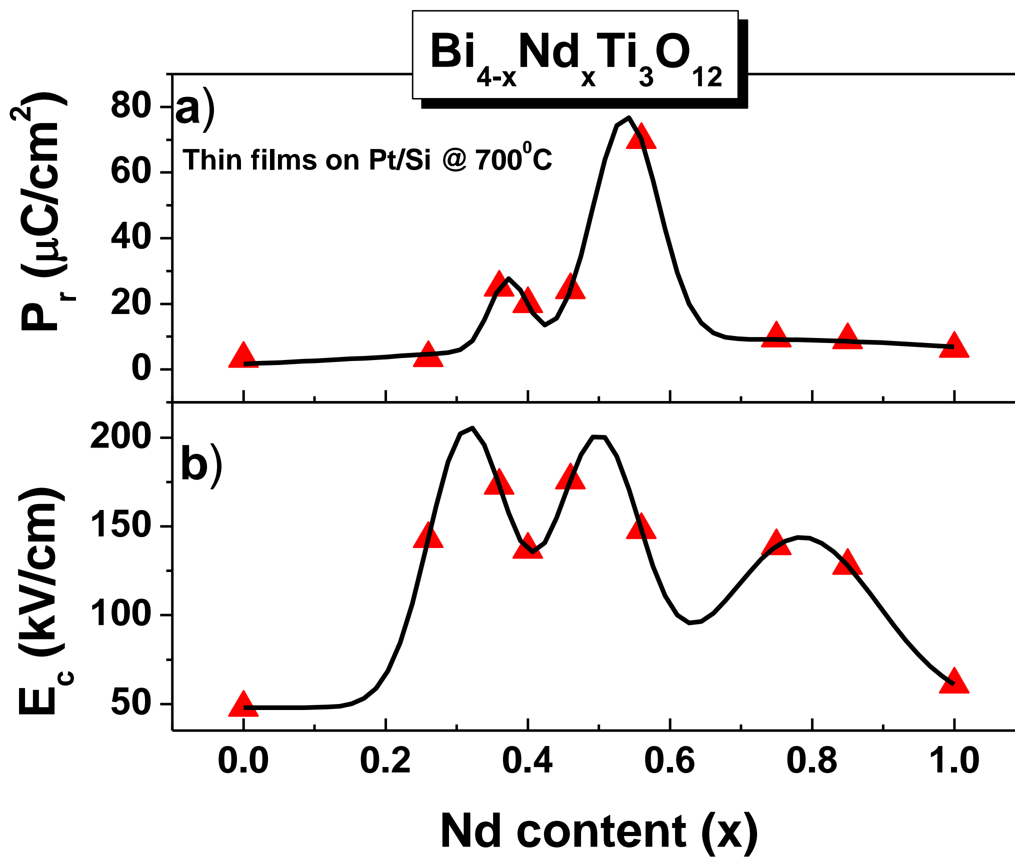

Figure 4.7. The values of a) the remnant polarization (P_r) and b) the coercive field (E_c) of the $Bi_{4-x}Nd_xTi_3O_{12}$ thin films for x = 0.00, 0.26, 0.36,0.40, 0.46, 0.56 (annealed electrode), 0.75, 0.85 and 1.00, on Pt ($Pt/TiO_2/SiO_2/Si$) substrate at 700°C.

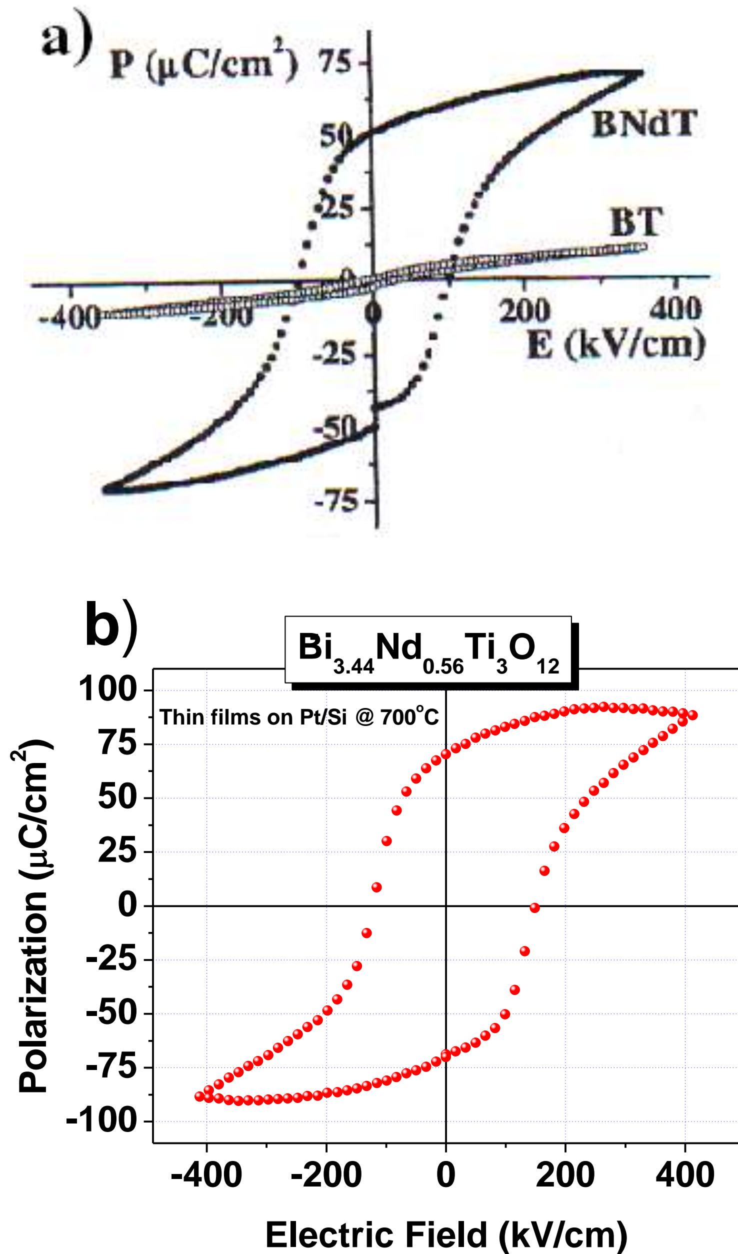

figure 4.8. compares the polarization vs electric field (P-E) switching curve of the a) higly c-axis oriented BNdT film ($Bi_{4-x}Nd_xTi_3O_{12}$ with x = 0.85)[5] with that of the b) (117) preferred oriented $Bi_{3.44}Nd_{0.56}Ti_3O_{12}$ film.

films. This results suggest that the giant polarization in preferred (117) orientation $Bi_{3.44}Nd_{0.56}Ti_3O_{12}$ thin films, result by the contribution of both *a*-axis polarization and *c*-axis polarization component. This explain he relative high remnant polarization of the (117) preferred oriented $Bi_{3.44}Nd_{0.56}Ti_3O_{12}$ compared to the highly c-axis oriented BNdT obtained for Chon.[5]

Figure 4.9 (a) shows the P-E hysteresis loop of the ferroelectric optimized Pt/(117) oriented $Bi_{3.44}Nd_{0.56}Ti_3O_{12}$/Pt capacitor before and after 1.4 x 10^9 cycles of polarization switching using 100 kHz triangular wave, which showed polarization Pr = 58 $\mu C/cm^2$ and coercive field Ec = 155 kV/cm for a maximum applied electric field of 290 kV/cm. After 1.4 x 10^9 switching cycles, 8.6 % degradation of P_r is observed in the film. No significant change in the shape of the hysteresis loops was observed even after 1.4x10^9 switching cycles. Figure 3.9(b) shows the fatigue response of the $Bi_{3.44}Nd_{0.56}Ti_3O_{12}$. A triangular waveform of 100 kHz frequency with electric field (290 kV/cm) was used to measure the fatigue test, under 10^9 cycles at a frequency of 1 MHz. All memory testing parameters (P*, P_r*, P^, Pr^, etc) have excellent fatigue resistance up to 1.4x 10^9cycles of the $Bi_{3.44}Nd_{0.56}Ti_3O_{12}$. We attribute the fatigue-free behavior to the better chemical stability of the perovskite layers against oxygen vacancies after substitution of some Bi^{3+}ions by Nd^{3+} ions and it is also responsible for the fatigue-free behavior that the unpinning rate of domain walls is larger than the pinning rate caused by Nd substitution, resulting in the fact that the domains are easily switched.

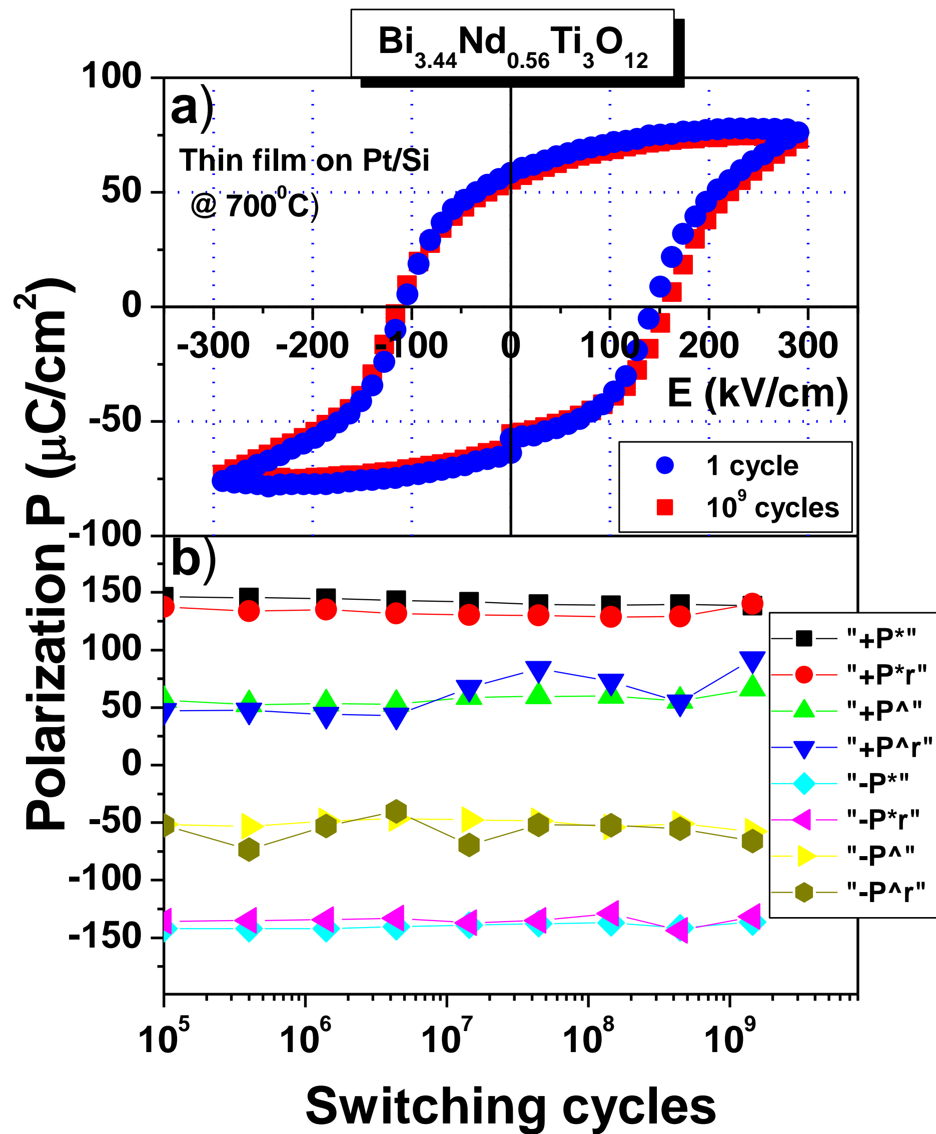

Figure 4.9. a) Ferroelectric response of the $Bi_{3.44}Nd_{0.56}Ti_3O_{12}$ thin film deposited on Pt ($Pt/TiO_2/SiO_2/Si$) substrate and annealed at 700^0C, for 1 cycle and after fatigue 10^9 cycles. b) Fatigue characteristics of the $Bi_{3.44}Nd_{0.56}Ti_3O_{12}$ film under 10^9 cycles at a frequency of 1 MHz.

4.3.4. Dielectric properties of $Bi_{4-x}Nd_xTi_3O_{12}$ thin films

Figure 4.10 a) shows the variation of dielectric constant and loss (tan δ) with applied electric field at 1 MHz. The typical butterfly shape of the measured dielectric constant-electric field in Fig. 4.10 a) clearly indicate the ferroelectric nature of $Bi_{3.44}Nd_{0.56}Ti_3O_{12}$ thin films. The peak was observed at about ± 80 kV/cm, for an maxima applied electric field of ±175 kV/cm which corresponded to positive and negative coercive fields. The dielectric constant and the dissipation factor (tan δ) of the $Bi_{3.44}Nd_{0.56}Ti_3O_{12}$ film capacitor were measured at 25^0C as a function of frequency. As shown in Fig. 4.10 b), The Dielectric constant and the dissipation factor are 434 and 0.07 at a frequency of 1 MHz, respectively. These values are comparable to those of PZT, SBT, and LBTO capacitors[8-10]. Although the dielectric constant decreases steadily with increasing frequency, there is no sudden change in its value up to 1 MHz. The dissipation factor (tan δ) shows little change with increasing frequency up to 1 MHz. the dissipation factor in this kind of ferroelectric thin films originated from various sources such as domain wall pinning, interfacial diffusion between the film and bottom electrodes, space charge accumulation at grain boundaries, oxygen vacancy, and the presence of secondary phase, etc. All these indicate that the observed ferroelectric response of the $Bi_{4-x}Nd_xTi_3O_{12}$ capacitor mostly originates from the ferroelectric polarization switching of bound charges, not form the response of freely moving charges. The frequency dispersion characteristics of dielectric constant and loss tangent in Fig.4.10 b) unambiguously indicate that $Bi_{3.44}Nd_{0.56}Ti_3O_{12}$ film have large distribution of relaxation time associate with polarize species. Since the range of frequency measurement is relatively low in the

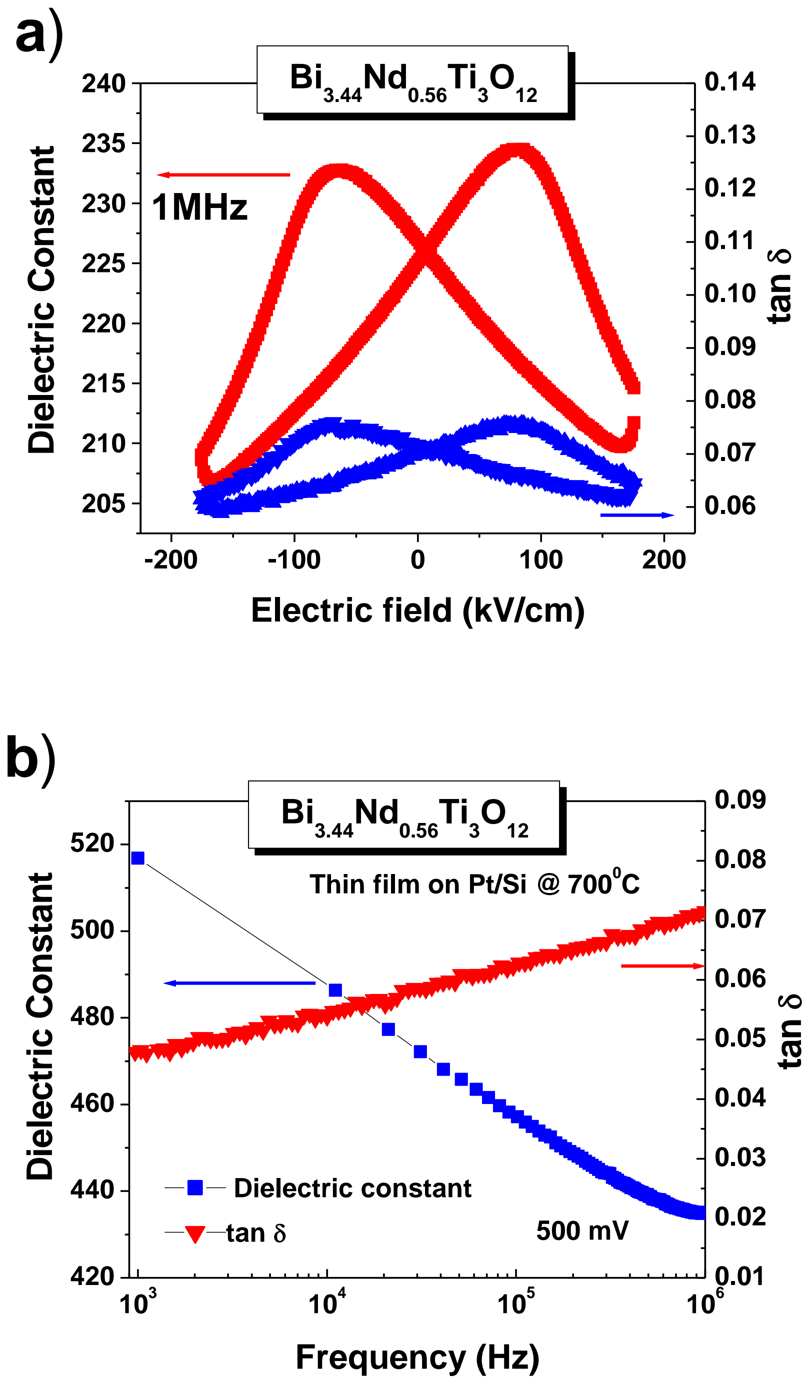

Figure 4.10. a) Dielectric constant and loss (tan δ) vs applied electric field on $Bi_{3.44}Nd_{0.56}Ti_3O_{12}$ film at 1 MHz, and b) dielectric constant measured at 25°C as a function of frequency in the range between 1 kHz and 1 MHz.

case presented, the dispersion is probably due to species with large masses. The most likely source of massive dipoles in these materials is abundance of oppositely charged species in the form of Bi and oxygen vacancy that can form during the high temperature process steps. The dipole concentration, for example, Bi and oxygen vacancy pairs, would depend on the processing conditions. A distribution in relaxation time is expected if the dipoles find themselves in varying environments due to random disorder in the sample. Hence, the presence of random disorder, whose degree is dependent on processing conditions, would give rise to dispersion in dielectric properties. Since the conversion of as deposited amorphous phase to layered Aurivillius phase involves the random nucleation of intermediate phases (e.g., fluorite), large number of defective regions develop in thin films. These defective regions don not have the opportunity to relax since the temperature is not sufficient for defect migration and annihilation. It can be observed from frequency dispersion measured values shown in Fig. 4.10 b) that the loss tangent (tan δ) at higher frequencies is about 7% which is comparable with the well established ferroelectric materials such as ferroelectric lead zirconate titanate and SBT.

4.3.5. Leakage current properties of $Bi_{4-x}Nd_xTi_3O_{12}$ thin films

The steady dc conductivity was examined by the leakage current density (J) versus electric field (E) characteristics.

Figure 4.11 shows the J-E characteristics of $Bi_{4-x}Nd_xTi_3O_{12}$ films on Pt ($Pt/TiO_2/SiO_2/Si$) substrate for the compositions: x = 0.00, 0.26, 0.36, 0.50, 0.56, 0.75,

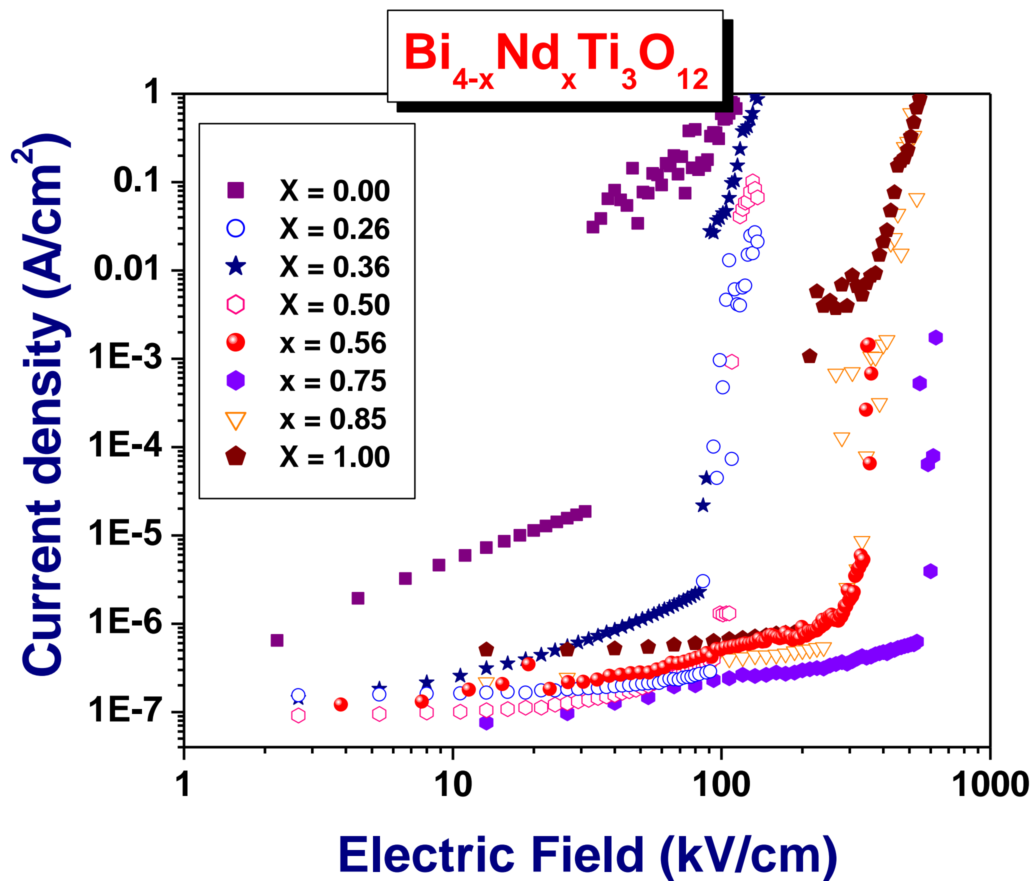

Figure 4.11. Leakage current at room temperature of the $Bi_{4-x}Nd_xTi_3O_{12}$ thin films deposited on Pt ($Pt/TiO_2/SiO_2/Si$) substrate and annealed at 700°C for the compositions: x = 0.00, 0.26, 0.36, 0.50, 0.56, 0.75, 0.85 and 1.00.

0.85 and 1.00 by Sol-Gel route and spin coating. The linear increase of leakage current density under low fields, and point of inflexion at certain intermediate field is clearly observed in each composition of BNdT films. The careful observation of Fig. 4.11 data indicates that the current follow ohmic behavior for low fields, and at higher field it appears to follow a power law until the dielectric breakdown occurs. These features are also observed in Fig. 4.11, but at higher fields these films apparently breakdown in most of the cases. Because, film is thick (0.52 μm), tunneling phenomena can be ruled out, and Ln J vs $E^{1/2}$ does not show nonlinear ohmic conduction, Poole-Frenkel current is also not valid. It is important, however, to note that pure $Bi_4Ti_3O_{12}$ film of same thickness show much large leakage current in comparison with Nd substituted $Bi_4Ti_3O_{12}$ films. One can also observe in Fig. 4.11 that $Bi_{4-x}Nd_xTi_3O_{12}$ films with the composition x = 0.75 showed the lowest leakage current (< 10^{-7} A/cm^2) and it followed the same linear ohmic behavior even at higher applied field, and inflexion at much higher field (400 kV/cm – 500 kV/cm), dielectric break down occurs. In general, BNdT films show dielectric breakdown after point of inflexion at certain high field for each composition. Leakage current of Fig. 4.11 reveals that in pure of $Bi_4Ti_3O_{12}$ films, after inflexion, is limited by the space charge conduction. In dielectrics, the low field region, current flows in the film and it controlled by the bulk i.e. ohmic behavior, and in intermediate fields, grain boundary regions may be effective, and under very high fields, space charge limited current (SCLC) and electrode-film interfacial resistance may dominate. But, in the case of BNdT for most compositions, films, dielectric breakdown occurs at higher field. Thus, in BNdT films, ohmic behavior dominates the leakage current transport in low field region and inflexion

region. These results indicate that the lower leakage current results from Nd preventing Bi from evaporating, and the higher leakage current is due to the evaporation of Bi during annealing. The measured leakage current densities ~ 10^{-7} A/cm^2 are comparable with the leakage current in PZT and SBT films.

These experimental results imply that Nd ions substituting for Bi ions suppresses the generation of oxygen vacancies and reduces the leakage current. In fact, for the BNdT films with x = 0.56, Nd substituted BTO results in a much larger P_r, than that of pure BTO and a marked improvement in the leakage current (5.3 x 10^{-7} A/cm^2 at electric field of the 100 kV/cm) properties. This implies that Nd substituted BTO leads to efficient decrease in space charge density. The reason for the fatigue problem of the BNdT film with x = 0.56 is still uncertain.

4.4. Conclusions

$Bi_{4-x}NdxTi_3O_{12}$ thin films were grown on Pt ($Pt/TiO_2/SiO_2/Si$) substrates by Sol-Gel process and spin coating. All of the BNdT films consist of a single phase of a bismuth-layered structure and have small grains of arbitrary shape with (117) orientation, shows complete solid solution up to the composition $x \leq 0.85$. Raman analyses show that Nd was incorporated into two possible sites, A site and Bi_2O_2 site respectively. At an applied voltage of 412 kV/cm the remanent polarization and the coercive field of the BNdT film with x = 0.56 annealed at 700ºC are about 70 μC/cm^2 and 148 kV/cm, respectively. At lower field, the leakage current is dominated by ohmic behavior in BNdT films. However, after 1.4 x 10^9 switching cycles, 8.6% degradation of P_r is observed in the film

with x = 0.56. The results on the structural, ferroelectric and dielectric properties of $Bi_{4-x}Nd_xTi_3O_{12}$ exhibited the most remarkable ferroelectric properties indicate that are important new candidate for nonvolatile random access memory devices alternate to lead-based ferroelectrics.

4.5 References

1. D. Cullity, *Elements of X-ray diffraction* (Addition-wesley publishing Co., Inc USA, 1967) p 261.

2. Y. Nogochi, M. Miyayama and T. Kudo, Phys. Rev. B 63, 214102 (2001).

3. P. R. Graves, G. Hua, S. Myhra, and J. G. Thompson, J. Solid State Chem. 144, 112 (1995).

4. S. Kojima, R. Imaizumi, S. Hamazaki, and M. Takaahige, Jpn. J. Appl. Phys. **33**, 5559 (1994).

5. U. Chon, H. M. Jang, M. G. Kim, and C. H. Chang, Phys. Rev. Lett. 89, 087601 (2002).

6. R.D. Shannon , Acta Crystallogr., Sect A: Cryst. Phys.,Diffr., Theor. Gen. Crystallogr. **A32**, 751 (1976).

7. M.S. Tomar, R.E. Melgarejo, S.P. Singh, Microelectronic Journal **36** 574 (2005).

8. H. D. Chen, K. R. Udayakumar, C. J. Gaskey, L. E. Cross, Appl. Phys. Lett. **67**, 3411 (1995).

9. R. Dat, J. K. Lee, O. Auciello, A. I. Kingon, Appl. Phys. Lett. **67**, 572 (1995).

10. B. H. Park, B.S. Kang, S. D. Bu, T. W. Noh, J. Lee and W. Jo, Nature **401**, 682 (1999).

11. S. Kojima and S. Shimida, Physica, **B 219-220**, 617 (1996).

Chapter 5

Studies of $Bi_{4-x}Sm_xTi_3O_{12}$ for ferroelectric devices

Thin films of $Bi_{4-x}Sm_xTi_3O_{12}$ (BSmT) were prepared by sol-gel process and thin films were deposited by spin coating on Pt ($Pt/TiO_2/SiO_2/Si$) substrate. We investigated the influence of substituting Sm ions for Bi ions on the structural and the ferroelectric properties. BSmT films annealed at 700°C were found to have of a single phase of a bismuth-layered structure with preferred (117) orientation. Sm substituted $Bi_4Ti_3O_{12}$ leads to a marked improvement in the remnant polarization (P_r) and the coercive field (E_c). The BSmT thin film showed a large remnant polarization Pr = 29 μC/cm^2 and Ec = 160 kV/cm for x = 0.70 composition. Show fatigue free, after 1.4 x10^9 switching cycles, 0.06 % degradation of P_r is observed in the film. The measured leakage current in BSmT films were much lower in comparison with pure $Bi_4Ti_3O_{12}$. The leakage current (less than 10^{-7} A/cm^2) at low field was observed in the film with composition x = 0.70. These results indicate the potential application of Sm substitution bismuth titanate films in non-volatile ferroelectric memories.

5.1. Experimental Details

The precursor solutions for $Bi_{4-x}Sm_xTi_3O_{12}$ (with x = 0.00, 0.36, 0.46, 0.56, 0.70, 0.75, and 0.85.) were bismuth nitrate pentahydrate, samarium nitrate hexahydrate, and titanium isopropoxide. Bismuth nitrate pentahydrate and samarium nitrate hexahydrate

were initially dissolved in acetic acid and then mixed together to obtain Bi and Sm stock solutions. Titanium isopropoxide was added in this solutions were mixed together to prepare the stoichometry, clear, transparent, and stable BSmT precursor. A 5% excess amount of bismuth nitrate pentahydrate was used to compensate for the Bi loss that occurs during the annealing process. Sol was prepared as mentioned in chapter 2 the section 2.3.3.

For the fabrication of the BSmT thin films, the diluted sol (0.3M) of the desired composition was used the BSmT precursor solution was syringed through a 0.2 μm syringe filter onto a $Pt/TiO_2/SiO_2/Si$ substrate. The films were produced by using a spin-coating technique with a spinner operated at 3000 rpm for 30s. To remove the organic contaminations, after the spin-coating procedure, we kept the films on a furnace at 600°C for 5 min. The coating and firing cycles were repeated required number of times. An optical thin films thickness measurement unit (F-20 Filmetrics Inc) was used to evaluate the thickness from the measured reflection spectrum of the annealed films. The top electrodes, 200 μm in diameter, were fabricated by using dc magnetron sputtering to deposit a 200 nm thick Pt film at room temperature.

$Cu\text{-}K_{\alpha}$ radiation (0.15405 nm) was used for recording x-ray diffraction patterns on $Bi_{4-x}Sm_xTi_3O_{12}$ materials for different compositions using Siemens D5000 x-ray diffractometer to determine the degree of orientation and crystallinity of the BSmT thin films. Room temperature micro-Raman spectra of the films were obtained by a spectrometer with triple monochromator (Jovin Yvon T6400) in a back scattering geometry. The spectra were excited with an Ar-ion laser operating at a wavelength of

514.5 nm. The frequency dependent dielectric permittivity and tangent loss were studied from 1 KHz to 1 MHz with an oscillating voltage of 500 mV using an HP 4294A impedance analyzer. The P-E hysteresis loops were measured using ferroelectric tester RT 600 HVS (Radiant Tech.) at virtual ground mode. Fatigue behavior was examined by applying triangular wave at 100 KHZ and 372 kV/cm electric field. Leakage current behavior was studied by electrometer (keithley 6517) interfaced to a computer with a voltage step 0.2V and delay time of 10s.

5.2 Results and Discussions

5.2.1 XRD Analysis

Figure 5.1 shows the X-ray diffraction patterns of $Bi_{4-x}Sm_xTi_3O_{12}$ thin films on $Pt/TiO_2/SiO_2/Si$ substrate for the compositions x = 0.00, 0.36, 0.46, 0.56, 0.70, 0.75, and 0.85. Miller indices are indicated for the diffraction peaks. As shown in Fig. 5.1, all of the films consisted of a single phase of a bismuth layered structured showing the preferred (117) orientation. The X-ray diffraction intensity tends to decrease with increasing Sm-content. The crystalline quality of the film can be estimated from the measured FWHM of the most intense (117) diffraction peak. Smaller FWHM value indicates better crystallinity of the film. The crystallite sizes of the $Bi_{4-x}Sm_xTi_3O_{12}$ films were calculated using Scherrer formula[1]. Table 5.1 shows that the crystallite sizes decrease as the Sm content increase. This may support the microstructural observation, as done using SEM (scanning electron microscopy), that the average grain size of perovskite BSmT films decreases with increasing Sm-content. The lattice parameters of the

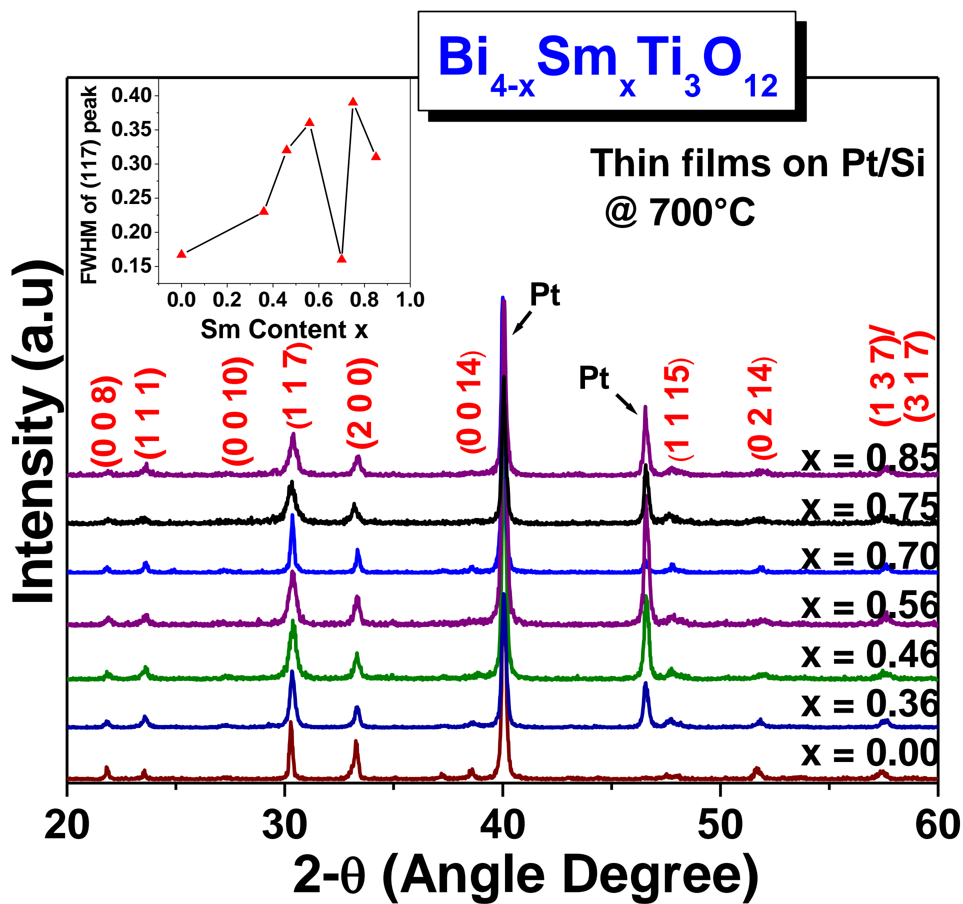

Figure 5.1 X-ray diffraction patterns of $Bi_{4-x}Sm_xTi_3O_{12}$ thin films on $Pt/TiO_2/SiO_2/Si$ substrate for the compositions x = 0.00, 0.36, 0.46, 0.56, 0.70, 0.75, and 0.85. The inset shows the variation of the FWHM of (117) peak with Sm content.

TABLE 5.1 Variation of crystallite size for different Sm content in $Bi_4Ti_3O_{12}$ films

Composition X	Crystallite size (nm)
0.00	62
0.36	42
0.46	30
0.56	27
0.70	60
0.75	25
0.85	31

$Bi_{4-x}Sm_xTi_3O_{12}$ films were calculated from their X-ray diffractograms. The lattice constants *a, b*, and *c* for BSmT which were estimated from the (006), (200) and (111) Bragg reflection in the XRD patterns, are presented in figure 5.2 where shows the variation of lattice constants of BSmT thin films as a function of Sm content. The slightly change in lattice constants indicates that Sm atoms are dissolved in the BTO lattice systematically. The lattice distortion (a/b ratio) of the orthorhombic phase was smallest in the samples.

Figure 5.3 shows the SEM micrographs of (a) x = 0.00, (b) x = 0.56, (c) x = 0.60 and (d) x = 0.70. Sm substituted BTO thin films on $Pt/TiO_2/SiO_2/Si$ substrates. As shown in micrographs, the grain size of the BTO film is substantially larger than that of the BSmT films, because of lower diffusivity of samarium, the substitution of samarium for bismuth suppresses the grain growth of BSmT, as observed in figure 5.3 (b), (c) and (d). In Figure 5.3 (a) small grains of arbitrary shape are observed. The SmBTO thin films were composed of spherical grains. The substitution of Sm^{3+} for Bi^{3+} in BTO films lead to reduction in grain size when the Sm content increase.

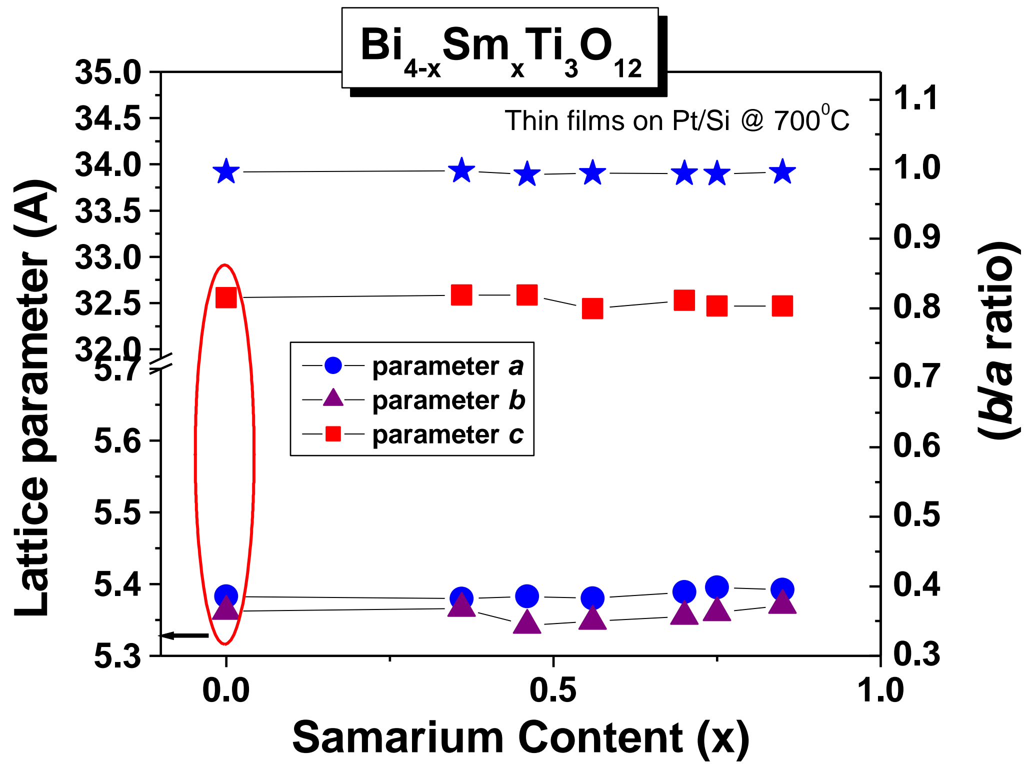

Figure 5.2 Variation in lattice parameters of BSmT thin films with different Sm content.

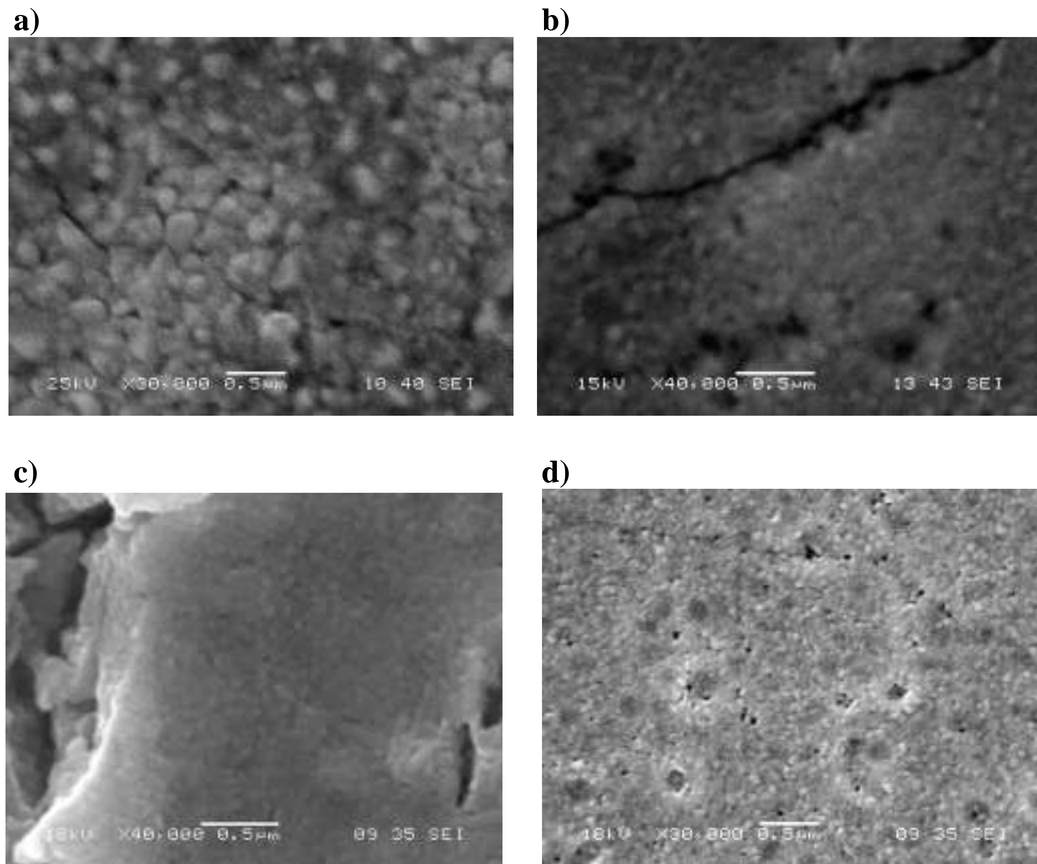

Figure 5.3. SEM micrographs of (a) BTO, (b) x = 0.56, (c) x = 0.70, (d) x = 0.80 Samarium content in $Bi_{4-x}Sm_xTi_3O_{12}$ thin films on $Pt/TiO_2/SiO_2/Si$ substrate.

5.2.2 Micro Raman analysis

Figure 5.4 shows the room temperature Raman spectra of the polycrystalline BSmT thin films in backscattering geometry using JY T64000 triple-monochromator. An optical microscope with 80X objective was used to focus the 514.5 nm excitation radiation from a Coherent Innova 99 Ar^+ laser and to collect the scattered radiation. The scattered signal was detected by a charge-couple device (CCD) detection system. The Raman selections rules in Aurivillius $Bi_4Ti_3O_{12}$ allow 16 phonon modes of different symmetries (6 A_{1g} + 2 B_{1g} + 8 E_g) if a tetragonal structure of the lattice is considered. It consist of Bi_2O_2 layers and perovskite-type structures ($A_{n-1}B_nO_{3n+1}$) with triple TiO_6 octahedra and A site Bi atom. The Bi^{3+} ion in A site is strongly under bonded and Ti^{4+} ion in B site is slightly over bonded. However, different numbers of Raman modes from $Bi_4Ti_3O_{12}$ have been reported in the literature[2-4], which can be explained by the possible overlap of the same symmetry vibrations and orthorhombic distortions of the material[5]. Figure 5.4 shows the room temperature recorded Raman spectra of $Bi_{4-x}Sm_xTi_3O_{12}$ films for compositions: x = 0.00, 0.46, 0.56, 0.70, 0.75, and 0.85. The Raman modes of $Bi_4Ti_3O_{12}$ films are in agreement with those observed in its crystal[2]. The film spectrum exhibits intense phonon modes at about 28, 45, 62, 86, 115, 270, 540 and 850 cm^{-1} and many other weak features. As the vibrational modes strongly depend on the atomic masses, the heavy Bi ions should be responsible for the low frequency modes (ν <100 cm^{-1}). The 60 cm^{-1} mode is known to originate from[2,3] the Bi displacements in Bi_2O_2 layer. The modes at about 270, 540 and 850 cm^{-1} are the internal modes of TiO_6 octahedra having A_{1g} character. The compositional dependence of Raman spectra shows

the similar effects on these internal modes they weaken and broaden with increasing content of Sm in films. Such changes are possible as Sm substituted is expected to introduce cationic disorder even though there is only a small difference in the ionic radii of Bi^{+3} and Sm^{+3} ions. The triplet bands at 86, 115 and 150 cm^{-1}, which were assigned to the modes of Bi ions (A site), became diffuse and their frequency increased clearly with increasing Sm content. If Sm substitutes Bi on the A-sites of the lattice, an increase in the mode frequency is expected from the mass difference as Bi is 1.38 times heavier than Sm, which is in accordance with the observed hardening of these modes. These results suggest that the Sm^{3+} ions are mainly incorporated into the Bi site (A site) of the perovskite slab for low La contents ($x < 0.75$). Most prominent effect of Sm substituted was observed on the low frequency modes. The Raman frequencies were obtained for each composition by fitting the peaks with the damped harmonic oscillator-type phonon functions Sm are plotted in figure 5.5. The lowest frequency (28 cm^{-1}) mode, which has been assigned as a soft-mode responsible for a phase transition at 675°C, shows softening behavior with Sm substituted. Compared to the soft mode, a little variation in the 32 cm^{-1} mode and the 62 cm^{-1} mode suggest that the substituted process least affects the Bi_2O_2 layers. The peak of the Bi_2O_2 layer mode at 62 cm^{-1} clearly broadens at $x \geq 0.75$ where the Sm ions start to incorporate into the Bi_2O_2 layers. We note that this affect the ferroelectric property of this material. We find that the lowest frequency mode at 28 cm^{-1} disappears at $x = 0.85$ probably due to the overdamping. Therefore, it seems probable that BSmT undergoes a ferroelectric-paraelectric phase transition at room temperature at $x = 0.85$.

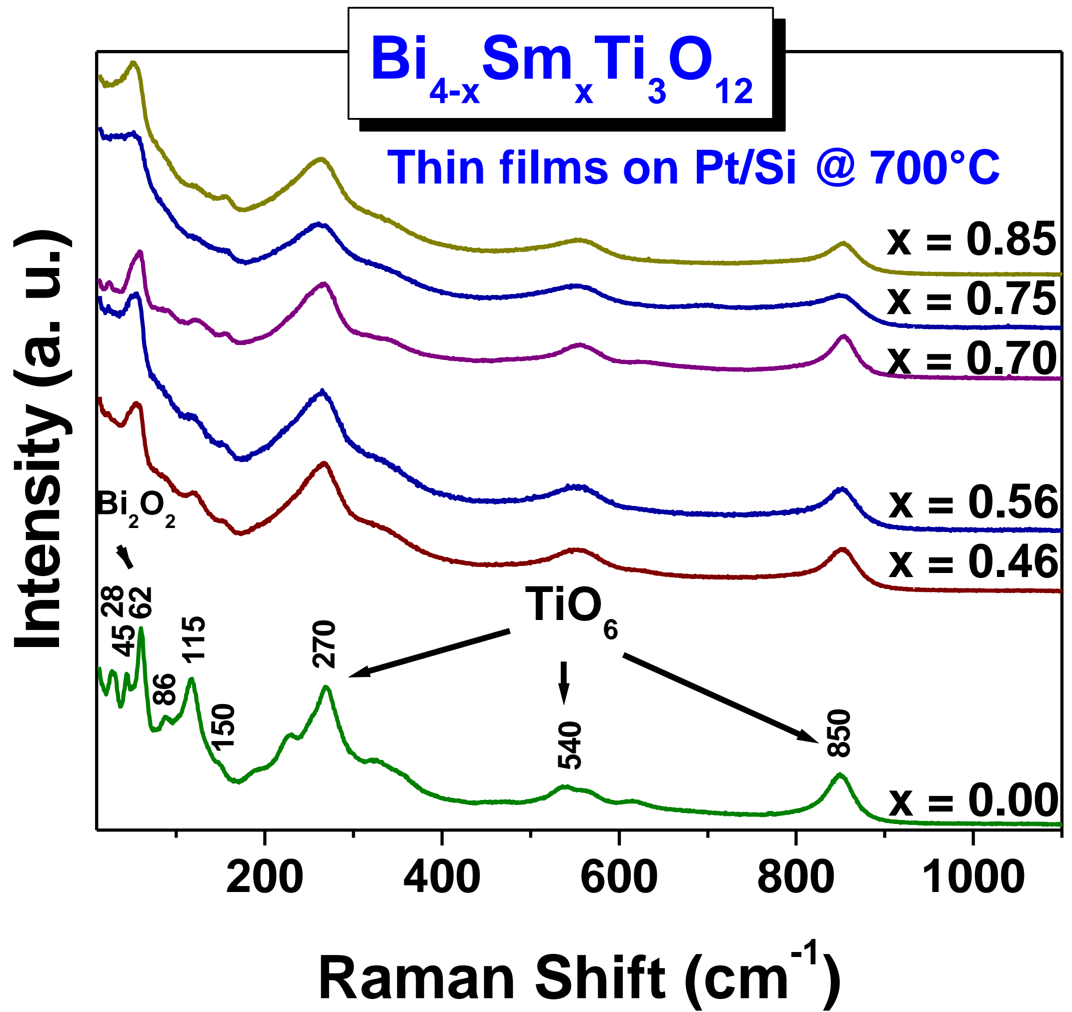

Figure 5.4. Room temperature Raman spectra of $Bi_{4-x}Sm_xTi_3O_{12}$ films on a Pt substrate ($Pt/TiO_x/SiO_2/Si$) for x = 0.00, 0.46, 0.56, 0.70, 0.75, and 0.85 composition. The indexes in the figure indicate peculiar modes to the local structures.

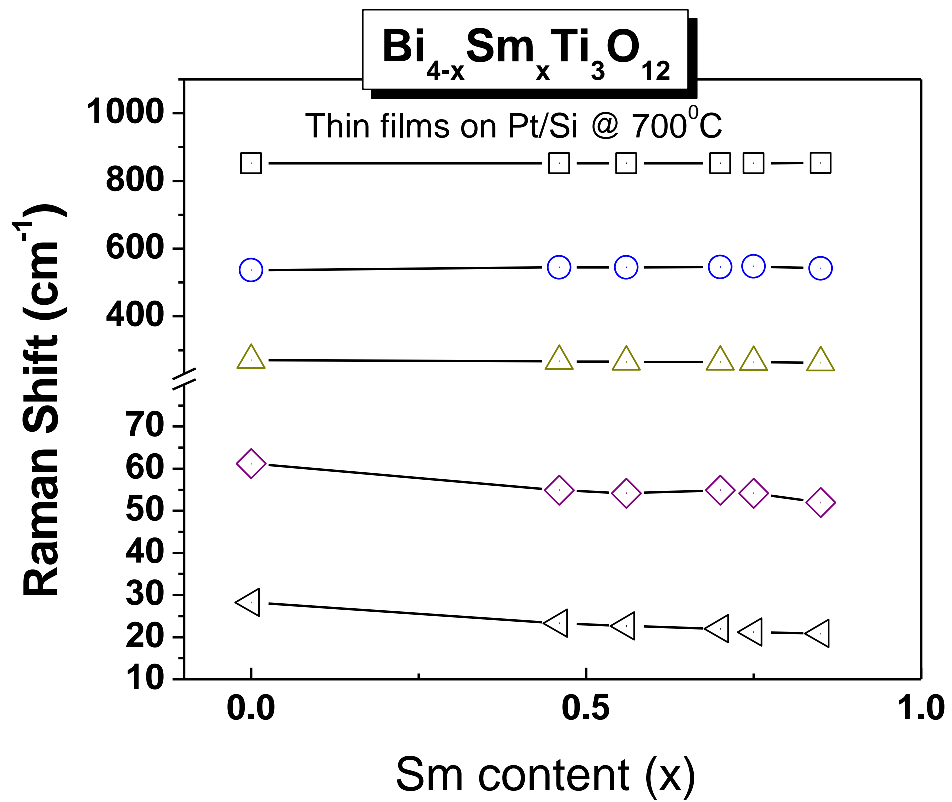

Figure 5.5. Raman frequencies as a function of Samarium compositions in $Bi_{4-x}Sm_xTi_3O_{12}$ thin films.

5.2.3. . Ferroelectric properties of $Bi_{4-x}Sm_xTi_3O_{12}$ thin films

For ferroelectric measurements, the top circular electrodes of platinum 200 nm thick and 200 μm diameter were deposited by dc sputtering. Ferroelectric response was recorded by RT6000HVS probe (Radiant Tech.) in virtual ground mode. For comparison, the ferroelectric response for the BSmT films of the compositions x = 0.00, 0.46, 0.50, 0.60, 0.70, 0.70 (annealed at 750^0C), 0.75 and 0.85, is show in Fig.5.6. With post annealing steps of the Pt electrode, a polarization ($2P_r$ = 58 μC/cm^2) for the film with composition x = 0.70 is shown in Fig. 5.6 with coercive field Ec = 140 kV/cm for a maximum applied electric field 333 kV/cm. In annealed at 750°C capacitor structure (x = 0.70) $2P_r$ ~ 68 μC/cm^2 is shown in the figure 5.6. For other compositions the polarization is much lower. The effects of the Sm-content on the variation of the remanent polarization (Pr) and the coercive field (Ec) of BSmT thin film were systematically examined at an applied electric field. As presented in figure 5.7, the value of the P_r increases gradually with increasing Sm-content for x below a certain critical level. The P_r shows its maximum value of 29 μC/cm^2 at x = 0.70 and decreases thereafter. The E_c increases rather steeply with increasing Sm-content from 48 to 114 kV/cm. The E_c shows its maximum value at x = 0.50 and decreases gradually thereafter. These results indicate that the substitution of Sm for Bi in BTO crystals substantially increases the P_r value parallel to the (117) orientation and that there is a critical Sm-concentration above which the P_r decreases again. The large polarization ($2P_r$ = 58 μC/cm^2) observed in x = 0.70 is remarkable with that of 49 μC/cm^2 for BSmT (x = 0.85) films deposited by metalorganic sol decomposition.[6] Due to the difference in ionic diameters of Sm (r(Sm^{3+}) = 1.24Å)[7] in

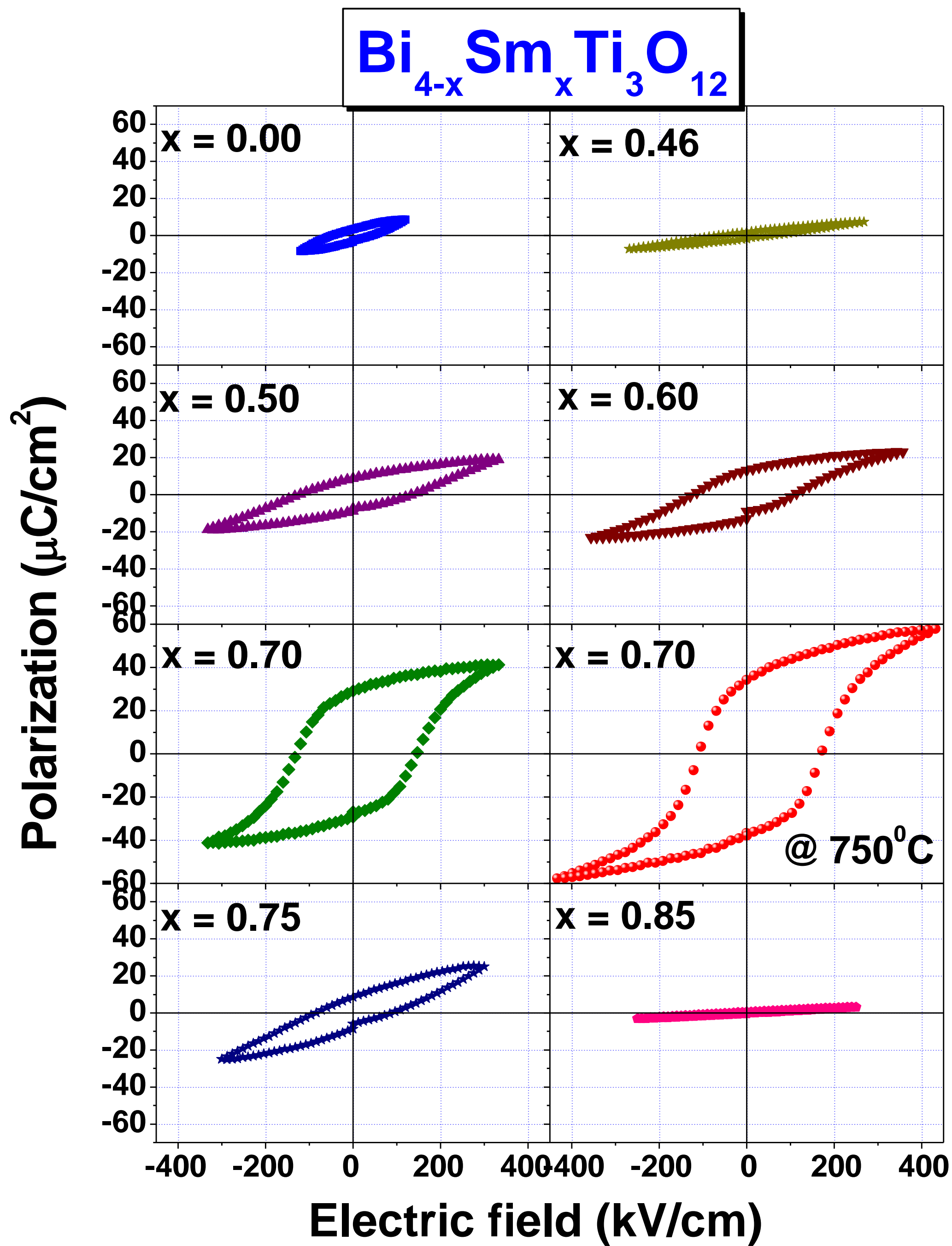

Figure 5.6. Ferroelectric response of the $Bi_{4-x}Sm_xTi_3O_{12}$ thin films for x = 0.00, 0.46, 0.50, 0.60, 0.70, 0.70 (annealed at 750^{0}C), 0.75 and 0.85, on Pt ($Pt/TiO_2/SiO_2/Si$) substrate at 700°C.

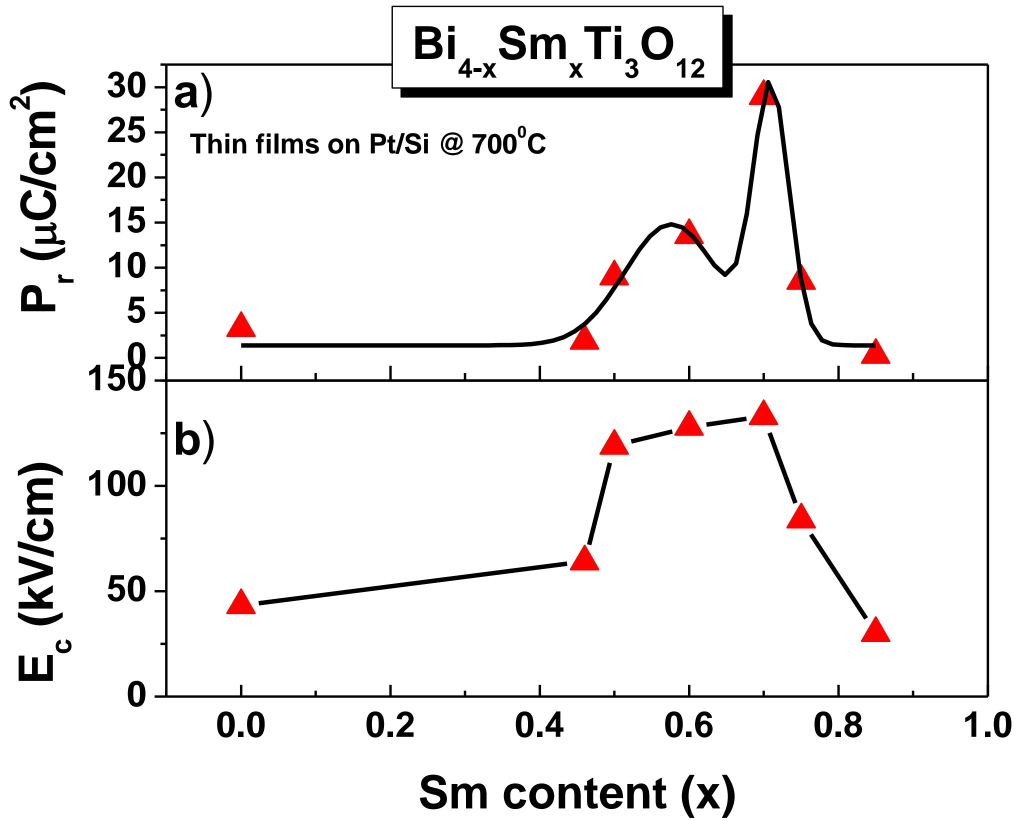

Figure 5.7. The values of a) the remanent polarization (P_r) and b) the coercive field (E_c) of the $Bi_{4-x}Sm_xTi_3O_{12}$ thin films for x = 0.00, 0.46, 0.60, 0.70, 0.75 and 0.85, on Pt ($Pt/TiO_2/SiO_2/Si$) substrate at 700°C.

the pseudo perovskite layer, the calculated values of lattice parameters $d_{(117)}$ in Sm substituted $Bi_4Ti_3O_{12}$ suggest a tilt in the TiO_6 octahedra[8]. This structural factor and the possibility of dipole formation give rise to the experimentally observed large ferroelectric polarization in $Bi_{3.30}Sm_{0.70}Ti_3O_{12}$.[9]

Ferroelectric response of Pt/(117) oriented $Bi_{3.30}Sm_{0.70}Ti_3O_{12}$/Pt capacitor structure was recorder using RT 6000HVS prove. Figure 5.8 (a) shows the P-E hysteresis loop of the ferroelectric optimized Pt/(117) oriented $Bi_{3.30}Sm_{0.70}Ti_3O_{12}$/Pt capacitor before and after 1.4×10^9 cycles of polarization switching using 100 kHz triangular wave, which showed polarization Pr = 17.50 μC/cm^2 and coercive field Ec = 110 kV/cm for a maximum applied electric field of 231 kV/cm. After 1.4×10^9 switching cycles, 0.06 % degradation of P_r is observed in the film. Figure 5.8(b) shows the fatigue response of the $Bi_{3.30}Sm_{0.70}Ti_3O_{12}$. A triangular waveform of 100 kHz frequency with electric field (372 kV/cm) was used to measure the fatigue test, under 1.4×10^9 cycles at a frequency of 1 MHz. For comparison, Figure 5.9 shows the fatigue response of the ferroelectric optimized Pt/(117) oriented $Bi_{3.30}Sm_{0.70}Ti_3O_{12}$/Pt capacitor annealed at 750ºC, after 4.4×10^9 switching cycles using 100 kHz triangular wave, 34. % degradation is observed in the film. It is assumed that fatigue characteristic may be attributed by the oxygen vacancies caused by higher annealing temperature at 750ºC.

Although there are no clear explanations as to why such different ferroelectric properties occur in samples with different amounts of Sm, the above results indicate that the ferroelectrical properties of BSmT should be optimized with an appropriate Sm concentration and annealing temperature.

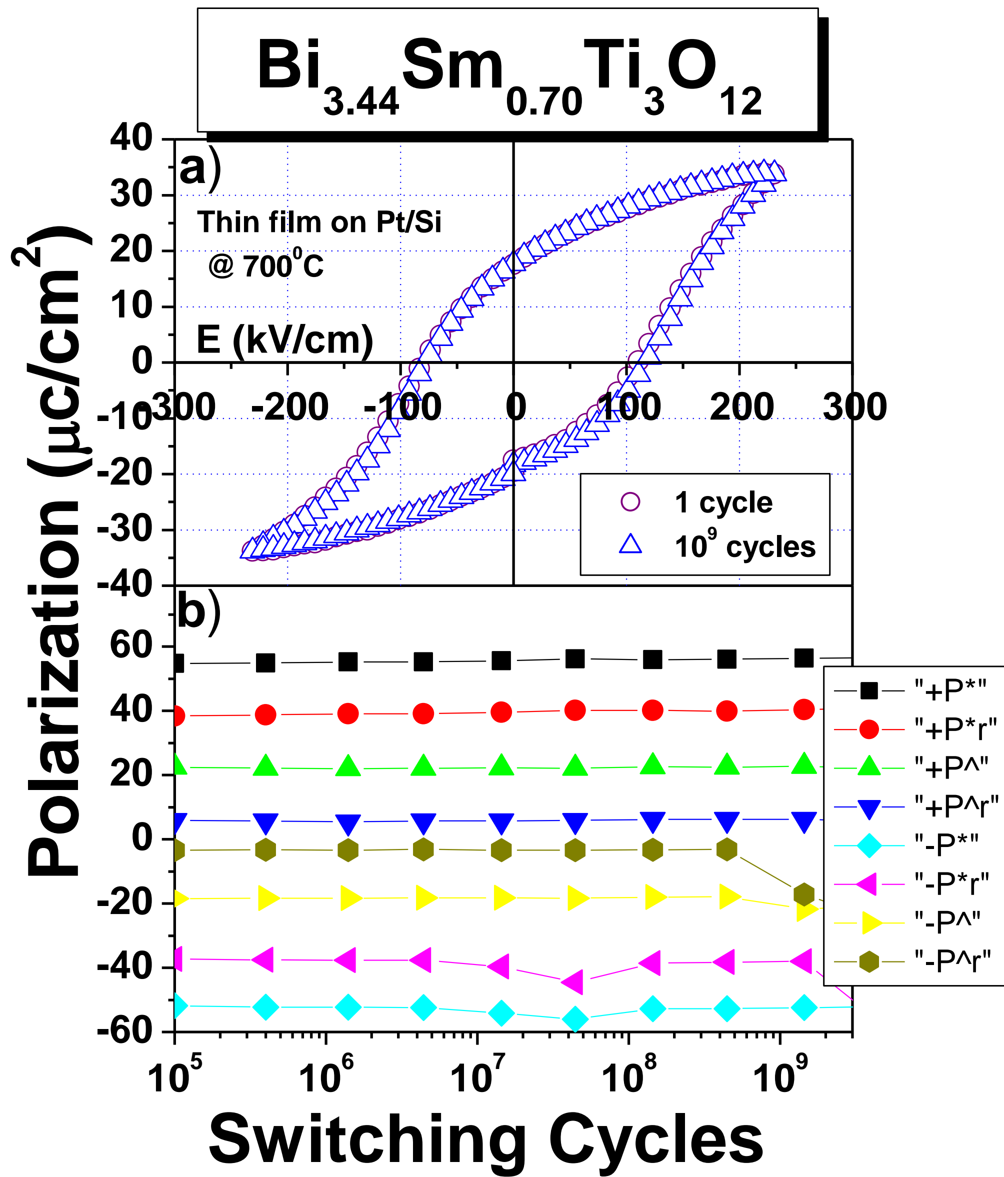

Figure 5.8. a) Ferroelectric response of the $Bi_{3.30}Sm_{0.70}Ti_3O_{12}$ thin film deposited on Pt ($Pt/TiO_2/SiO_2/Si$) substrate and annealed at 700^0C, for 1 cycle and after fatigue $1.4x10^9$ cycles. b) Fatigue characteristics of the $Bi_{3.30}Sm_{0.70}Ti_3O_{12}$ film under $1.4x10^9$ cycles at a frequency of 1 MHz.

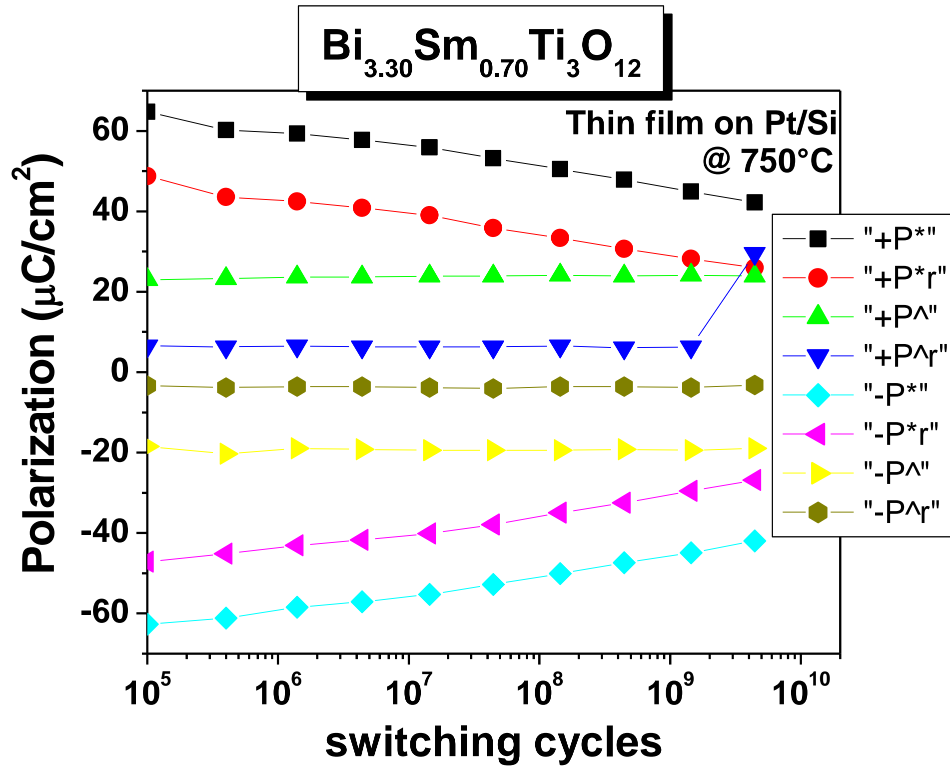

Figure 5.9. Fatigue characteristics of the $Bi_{3.30}Sm_{0.70}Ti_3O_{12}$ film annealed at 750°C under $4.4x10^9$ cycles at a frequency of 1 MHz.

5.2.4. Dielectric properties of $Bi_{4-x}Sm_xTi_3O_{12}$ thin films

The dielectric constant and the dissipation factor (tan δ) of the $Bi_{3.30}Sm_{0.70}Ti_3O_{12}$ film capacitor were measured at 25^0C as a function of frequency. As shown in Figure. 5.10, The Dielectric constant and the dissipation factor are 344 and 0.039 at a frequency of 1 MHz, respectively. These values are comparable to those of PZT, SBT, and LBTO capacitors.[10-12] Although the dielectric constant decreases steadily with increasing frequency, there is no sudden change in its value up to 1 MHz. The dissipation factor (tan δ) shows little change with increasing frequency up to 1 MHZ. All these indicate that the observed ferroelectric response of the $Bi_{4-x}Sm_xTi_3O_{12}$ capacitor mostly originates from the ferroelectric polarization switching of bound charges, not from the response of freely moving charges. The frequency dispersion characteristics of dielectric constant and loss tangent in figure 5.10 unambiguously indicate that $Bi_{3.30}Sm_{0.70}Ti_3O_{12}$ film have large distribution of relaxation time associate with polarize species. Since the range of frequency measurement is relatively low in the case presented, the dispersion is probably due to species with large masses. The most likely source of massive dipoles in these materials is abundance of oppositely charged species in the form of Bi and oxygen vacancy that can form during the high temperature process steps. The dipole concentration, for example, Bi and oxygen vacancy pairs, would depend on the processing conditions. A distribution in relaxation time is expected if the dipoles find themselves in varying environments due to random disorder in the sample. Hence, the presence of random disorder, whose degree is dependent on processing conditions, would give rise to dispersion in dielectric properties. Since the conversion of as deposited

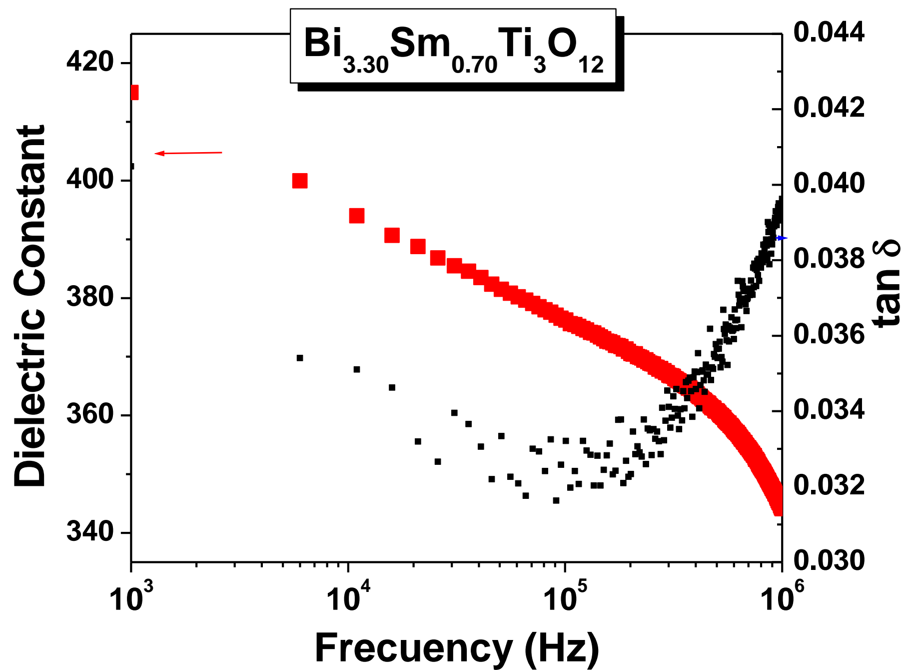

Figure 5.10. Dielectric constant measured at 25^0C on $Bi_{3.30}Sm_{0.70}Ti_3O_{12}$ film as a function of frequency in the range between 1 kHz and 1 MHz.

amorphous phase to layered Aurivillius phase involves the random nucleation of intermediate phases (e.g., fluorite), large number of defective regions develop in thin films. These defective regions don not have the opportunity to relax since the temperature is not sufficient for defect migration and annihilation. It can be observed from frequency dispersion measured values shown in Fig. 5.10 that the loss tangent (tan δ) at higher frequencies is about 4% which is comparable with the well established ferroelectric materials such as ferroelectric lead zirconate titanate and SBT.

5.2.5. Leakage current properties of $Bi_{4-x}Sm_xTi_3O_{12}$ thin films

The steady dc conductivity was examined by the leakage current density (J) versus electric field (E) characteristics. Figure 5.11 shows the J-E characteristics of $Bi_{4-x}Sm_xTi_3O_{12}$ (BSmT) films on Pt ($Pt/TiO_2/SiO_2/Si$) substrate for the compositions: x = 0.00, 0.46, 0.60, 0.70, and 0.75, by Sol-Gel route and spin coating. The linear increase of leakage current density under low fields, and point of inflexion at certain intermediate field is clearly observed in each composition of BSmT films. The careful observation of Fig. 5.11 data indicates that the current follow ohmic behavior for low fields, and at higher field it appears to follow a power law until the dielectric breakdown occurs. These features are also observed in Fig. 5.11, but at higher fields these films apparently breakdown in most of the cases. Because, film is thick (0.56 µm), tunneling phenomena can be ruled out, and Ln J vs $E^{1/2}$ does not show nonlinear ohmic conduction, Poole-Frenkel current is also not valid. It is important, however, to note that pure $Bi_4Ti_3O_{12}$ film of same thickness show much large leakage current in comparison with Sm substituted

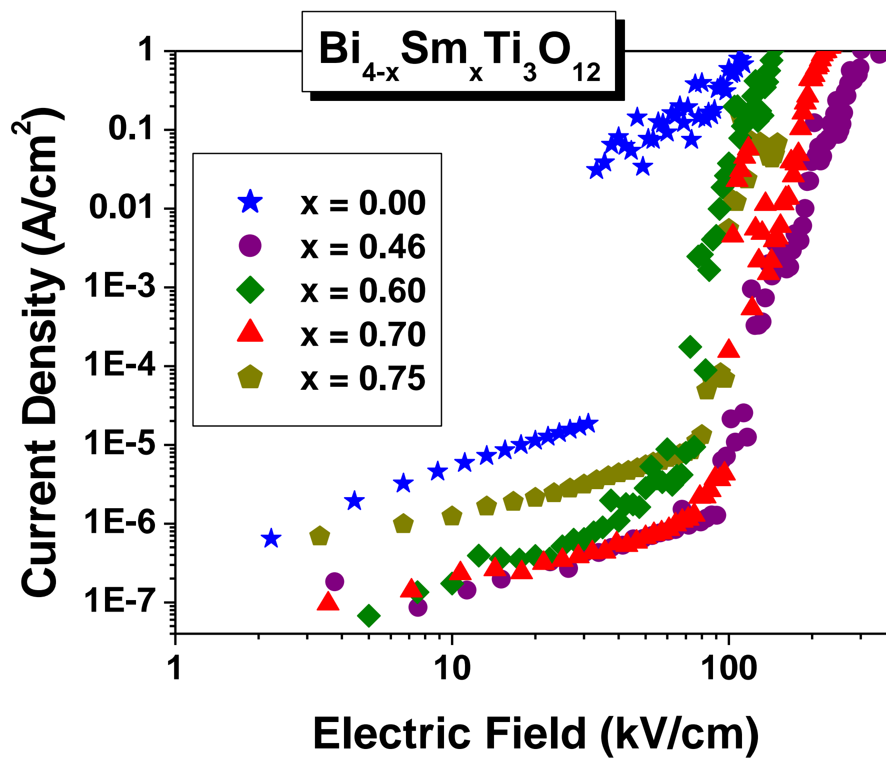

Figure 5.11. Leakage current at room temperature of the $Bi_{4-x}Sm_xTi_3O_{12}$ thin films deposited on Pt ($Pt/TiO_2/SiO_2/Si$) substrate and annealed at 700°C for the compositions: x = 0.00, 0.46, 0.60, 0.70, and 0.75.

$Bi_4Ti_3O_{12}$ films. In general, BSmT films show dielectric breakdown after point of inflexion at certain high field for each composition. Leakage current of Fig. 5.11 reveals that in pure of $Bi_4Ti_3O_{12}$ films, after inflexion, is limited by the space charge conduction. In dielectrics, the low field region, current flows in the film and it controlled by the bulk i.e. ohmic behavior, and in intermediate fields, grain boundary regions may be effective, and under very high fields, space charge limited current (SCLC) and electrode-film interfacial resistance may dominate. But, in the case of BSmT for most compositions, films, dielectric breakdown occurs at higher field. Thus, in BSmT films, ohmic behavior dominates the leakage current transport in low field region and inflexion region. These results indicate that the lower leakage current results from Sm preventing Bi from evaporating, and the higher leakage current is due to the evaporation of Bi during annealing. The measured leakage current densities ~ 10^{-7} A/cm^2 are comparable with the leakage current in PZT and SBT films.

These experimental results imply that Sm ions substituting for Bi ions suppresses the generation of oxygen vacancies and reduces the leakage current. In fact, for the BSmT films with x = 0.70, Sm substituted BTO results in a much larger P_r, than that of pure BTO and a marked improvement in the leakage current (4.3 x 10^{-6} A/cm^2 at electric field of the near 100 kV/cm) properties. This implies that Sm substituted BTO leads to efficient decrease in space charge density. The reason for the fatigue problem of the BSmT film with x = 0.70 is still uncertain, but a deficient Bi content may be a major defect causing ferroelectric fatigue.

5.3. Conclusions

$Bi_{4-x}Sm_xTi_3O_{12}$ thin films were grown on Pt ($Pt/TiO_2/SiO_2/Si$) substrates by Sol-Gel process and spin coating and their grain size, Raman spectra, dielectric hysteresis loops, fatigue, leakage current were systematically investigated as a function of Sm content. All of the BSmTO films consist of a single phase of a bismuth-layered structure and have small grains of arbitrary shape with (117) orientation, shows complete solid solution up to the composition $x \leq 0.85$. At an applied Electric field of 307 kV/cm the remnant polarization and the coercive field of the BSmT film with x = 0.70 annealed at 700°C are about 29 μC/cm^2 and 133 kV/cm, respectively. After 1.4×10^9 switching cycles, 0.06 % degradation of P_r is observed in the film. At lower field, the leakage current is dominated by ohmic behavior in BSmT films. It reveals that A-site substitution is an efficient way in improving ferroelectric nature when with optimum substitution content (x = 0.70 in our experiment).

5.4 References

1. D. Cullity, *Elements of X-ray diffraction* (Addition-wesley publishing Co., Inc USA, 1967) p 261.

2. P. R. Graves, G. Hua, S. Myhra, and J. G. Thompson, J. Solid State Chem. 144, 112 (1995).

3. S. Kojima, R. Imaizumi, S. Hamazaki, and M. Takaahige, Jpn. J. Appl. Phys. **33**, 5559 (1994).

4. M. Osada, M. Tada, M. Kakihama, T. Watanabe, and H. Funakubo, Jpn. J. Appl. Phys. Part 1, **40**, 5572 (2001).

5. S. Kojima and S. Shimida, Physica, **B 219-220**, 617 (1996).

6. U. Chon, K-B. Kim, H. M. Jang, and G-C. Yi, Appl. Phys. Lett. **79**, 3137 (2001).

7. R.D. Shannon , Acta Crystallogr., Sect A: Cryst. Phys.,Diffr., Theor. Gen. Crystallogr. **A32**, 751 (1976).

8. U. Chon, H. M. Jang, M. G. Kim, and C. H. Chang, Phys. Rev. Lett. 89, 087601 (2002).

9. S.Dussan, M. S. Tomar, R.E. Melgarejo, and R. S. Katiyar. Mater. Res. Soc Symp. Proc., Vol 902E 0902-T03-54.1-092-T03-54.6 (2005).

10. H. D. Chen, K. R. Udayakumar, C. J. Gaskey, L. E. Cross, Appl. Phys. Lett. **67**, 3411 (1995).

11. R. Dat, J. K. Lee, O. Auciello, A. I. Kingon, Appl. Phys. Lett. **67**, 572 (1995).

12. B. H. Park, B.S. Kang, S. D. Bu, T. W. Noh, J. Lee and W. Jo, Nature **401**, 682 (1999).

Chapter 6

Structural, ferroelectric and magnetic properties of $Bi_{4-x}Gd_xTi_3O_{12}$ thin films

Thin films of $Bi_{4-x}Gd_xTi_3O_{12}$ were prepared by sol-gel process and thin films were deposited by spin coating at 3000 RPM on Pt ($Pt/TiO_2/SiO_2/Si$) substrate. We investigated systematically the influence of substituting Gd ions for Bi ions on the structural and the ferroelectric properties. BGdT films annealed at 700°C were found to have of a single phase of a bismuth-layered structure with preferred (117) orientation. Gd substituted $Bi_4Ti_3O_{12}$ leads to a marked improvement in the remanent polarization (P_r) and the coercive field (E_c). The BGdT thin film showed a large remanent polarization P_r = 27 μC/cm^2 for x = 0.30 composition. However, after 4.44 x10^9 switching cycles, 9% degradation of P_r is observed in the film. The measured leakage current in BGdT films were much lower in comparison with pure $Bi_4Ti_3O_{12}$. The leakage current (less than 10^{-8} A/cm^2) at low field was observed in the film with composition x = 0.30. Magnetic response of the powder sample for composition: x = 0.85 was tested using SQUID, which showed super-paramagnetic at room temperature and magnetic at 5 K with magnetic coercitivity (Hc = 29 Oe) and very small ferromagnetic magnetization (σr = 5.4 x 10^{-4} emu/g).

6.1. Introduction

The materials having two or more than two distinct properties are inherently important for interesting physics and applications. Mixed metal oxides including perovskite and layered structures have played an important roles as dielectrics, ferroelectrics, and ionic conductors. Aurivillius phase materials consist of alternating perovskite-like $A_{n-1}B_nO_{3n+1}$ and fluorite-like Bi_2O_2 layers, where A is a mono-, di, or trivalent cation, B is a cation with valence 4, 5 or 6, and *n* is the number of perorvskite-like layers[1.2]. $Bi_4Ti_3O_{12}$ is one of the few compounds within the Aurivillius family[3,4]that has a monoclinic ferroelectric structure, with one component of the polarization in the plane of the layers, and the other perpendicular to this plane. The origin of the ferroelectric polarization within the layers may be[5] due to the large displacement of Bi^{3+} ion in A site is strongly underbonded, and Ti^{4+} ion in the B site is slightly overbonded. Thus, the partial replacement of Bi^{3+} by suitable trivalent cations, could modify the polarization behavior[6,7] of the material system. A partial substitution of Bi-ion by Gd ion in $Bi_{4-x}Gd_xTi3O_{12}$ will be enhanced interesting properties.

6.2. Experimental Details

The precursor solutions for $Bi_{4-x}Gd_xTi_3O_{12}$ (with x = 0.00, 0.30, 0.46, 0.56, 0.60, 0.70, 0.85, and 1.00) were bismuth nitrate pentahydrate, gadolinium nitrate hexahydrate, and titanium isopropoxide. Bismuth nitrate pentahydrate and neodymium nitrate hexahydrate were initially dissolved in acetic acid and then mixed together to obtain Bi and Gd stock solutions. Titanium isopropoxide was added in this solutions were mixed

together to prepare the stoichometry, clear, transparent, and stable BGdT precursor. A 5% excess amount of bismuth nitrate pentahydrate was used to compensate for the Bi loss that occurs during the annealing process. Sol was prepared as mentioned in chapter 2 the section 2.3.4.

For the fabrication of the BGdT thin films, the diluted sol (0.3M) of the desired composition was used the BGdT precursor solution was syringed through a 0.2 μm syringe filter onto a $Pt/TiO_2/SiO_2/Si$ substrate. The films were produced by using a spin-coating technique with a spinner operated at 3000 rpm for 30s. To remove the organic contaminations, after the spin-coating procedure, we kept the films on a furnace at 600°C for 5 min. The coating and firing cycles were repeated required number of times. The pre-baked films were annealed at 700°C for 1 h under air atmosphere for crystallization. An optical thin films thickness measurement unit (F-20 Filmetrics Inc) was used to evaluate the thickness from the measured reflection spectrum of the annealed films. The top electrodes, 200 μm in diameter, were fabricated by using dc magnetron sputtering to deposit a 200 nm thick Pt film at room temperature.

Cu-K_α radiation (0.15405 nm) was used for recording x-ray diffraction patterns on $Bi_{4-x}Gd_xTi_3O_{12}$ materials for different compositions using Siemens D5000 x-ray diffractometer to determine the degree of orientation and crystallinity of the BGdT thin films. Room temperature micro-Raman spectra of the films were obtained by a spectrometer with triple monochromator (Jovin Yvon T6400) in a back scattering geometry. The spectra were excited with an Ar-ion laser operating at a wavelength of 514.5 nm. The frequency dependent dielectric permittivity and tangent loss were studied

from 1 KHz to 1 MHz with an oscillating voltage of 500 mV using an HP 4294A impedance analyzer. The P-E hysteresis loops were measured using ferroelectric tester RT 600 HVS (Radiant Tech.) at virtual ground mode. Fatigue behavior was examined by applying triangular wave at 100 KHZ and 375 kV/cm. Leakage current behavior was studied by electrometer (keithley 6517) interfaced to a computer with a voltage step 0.2V and delay time of 10s.

6.3 Results and Discussions

6.3.1 XRD Analysis

Figure 6.1 shows the X-ray diffraction patterns of $Bi_{4-x}Gd_xTi_3O_{12}$ thin films on $Pt/TiO_2/SiO_2/Si$ substrate for the compositions x = 0.00, 0.30, 0.46, 0.56, 0.60, 0.70, 0.85, and 1.00. Miller indices are indicated for the diffraction peaks. As shown in Fig. 6.1, all of the films consisted of a single phase of a bismuth layered structured showing the preferred (117) orientation. The crystalline quality of the film can be estimated from the measured Full Width at Half the Maxima (FWHM) of the most intense (117) diffraction peak. Smaller FWHM value indicates better crystallinity of the film. The crystallite sizes of the $Bi_{4-x}Gd_xTi_3O_{12}$ films were calculated using Scherrer formula[8]. Table 6.1 shows that the crystallite sizes decrease as the Gd content increase. This may support the microstructural observation, as done using SEM (scanning electron microscopy), that the average grain size of perovskite BGdT films decreases with increasing Gd-content. The lattice parameters of the $Bi_{4-x}Gd_xTi_3O_{12}$ films were calculated from their X-ray diffractograms.

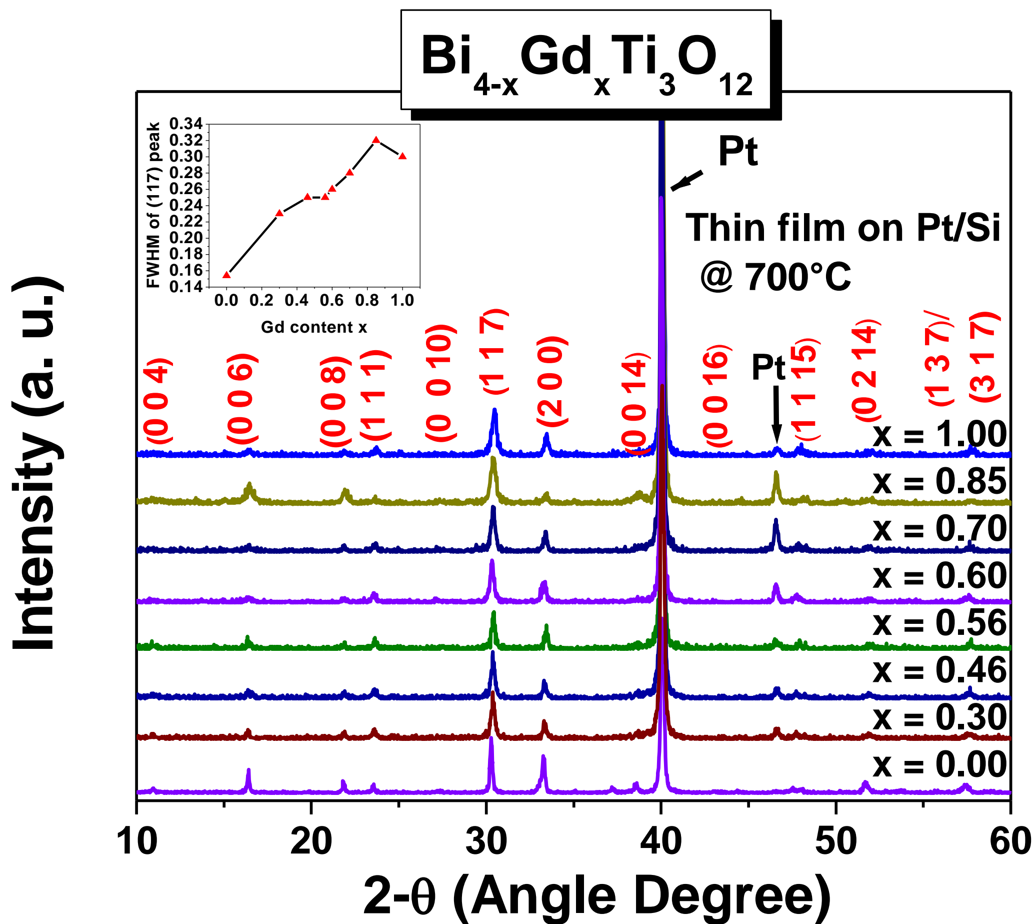

Figure 6.1 X-ray diffraction patterns of $Bi_{4-x}Gd_xTi_3O_{12}$ (BGdT) thin films on $Pt/TiO_2/SiO_2/Si$ substrate for the compositions x = 0.00, 0.30, 0.46, 0.56, 0.60, 0.70, 0.85, and 1.00. The inset shows the variation of the FWHM of (117) peak with Gd content.

TABLE 6.1 Variation of crystallite size for different Gd content in $Bi_4Ti_3O_{12}$ films

Composition X	Crystallite size (nm)
0.00	60
0.30	40
0.46	37
0.56	37
0.60	35
0.70	33
0.85	29
1.00	30

The lattice constants *a*, *b*, and *c* for BGdT which were estimated from the (006), (200) and (111) Bragg reflection in the XRD patterns, are presented in figure 6.2 where shows the variation of lattice constants of BGdT thin films as a function of Gd content. The slightly change in lattice constants indicates that Gd atoms are dissolved in the BTO lattice systematically. The lattice distortion (*a*/*b* ratio) of the orthorhombic phase was smallest in the samples.

Figure 6.3 shows the SEM micrographs of (a) x = 0.00, (b) x = 0.30, (c) x = 0.50 and (d) x = 1.00 Gd substituted BTO thin films on $Pt/TiO_2/SiO_2/Si$ substrates. As shown in micrographs, the grain size of the BTO film is substantially larger than that of the BGdT films (x = 0.30, x = 0.50 and x = 1.00) considering the well-known volatility of bismuth, one expects that the diffusivity of bismuth will be significantly higher than that of gadolinium. In this case, because of lower diffusivity of gadolinium, the substitution of gadoliniium for bismuth suppresses the grain growth of BGdT, as observed in figure 6.3 (b), (c) and (d). In Figure 6.3 (a) small grains of arbitrary shape are observed, but had

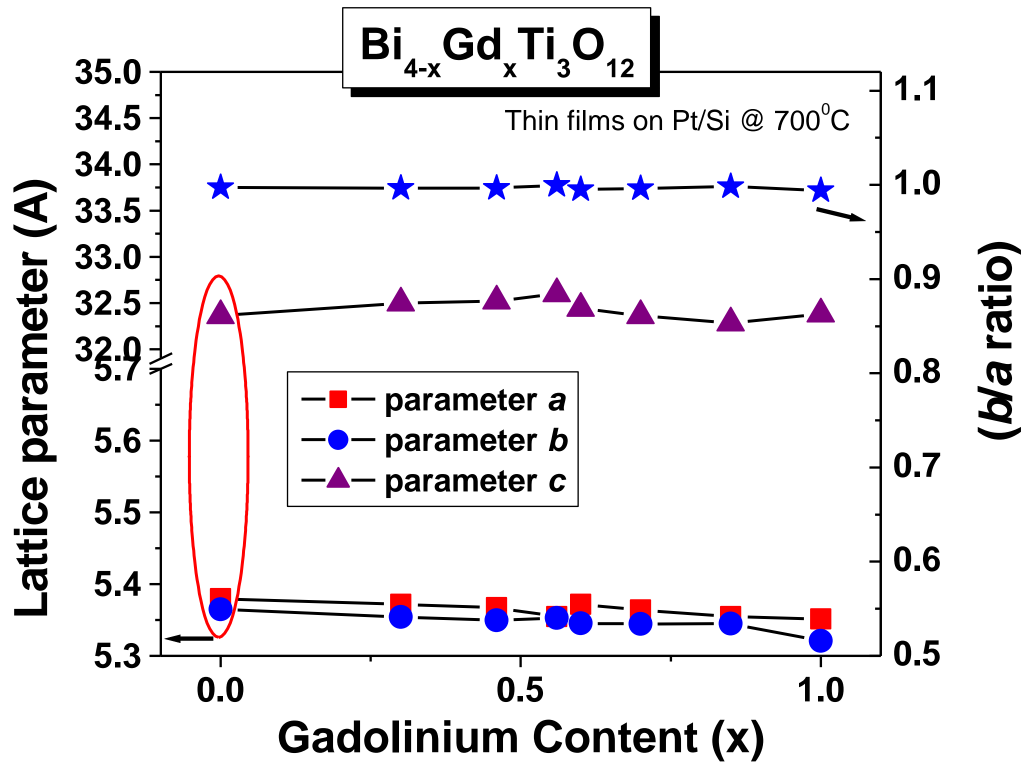

Figure 6.2. Variation in lattice parameters of GdBTO thin films with different Gd content.

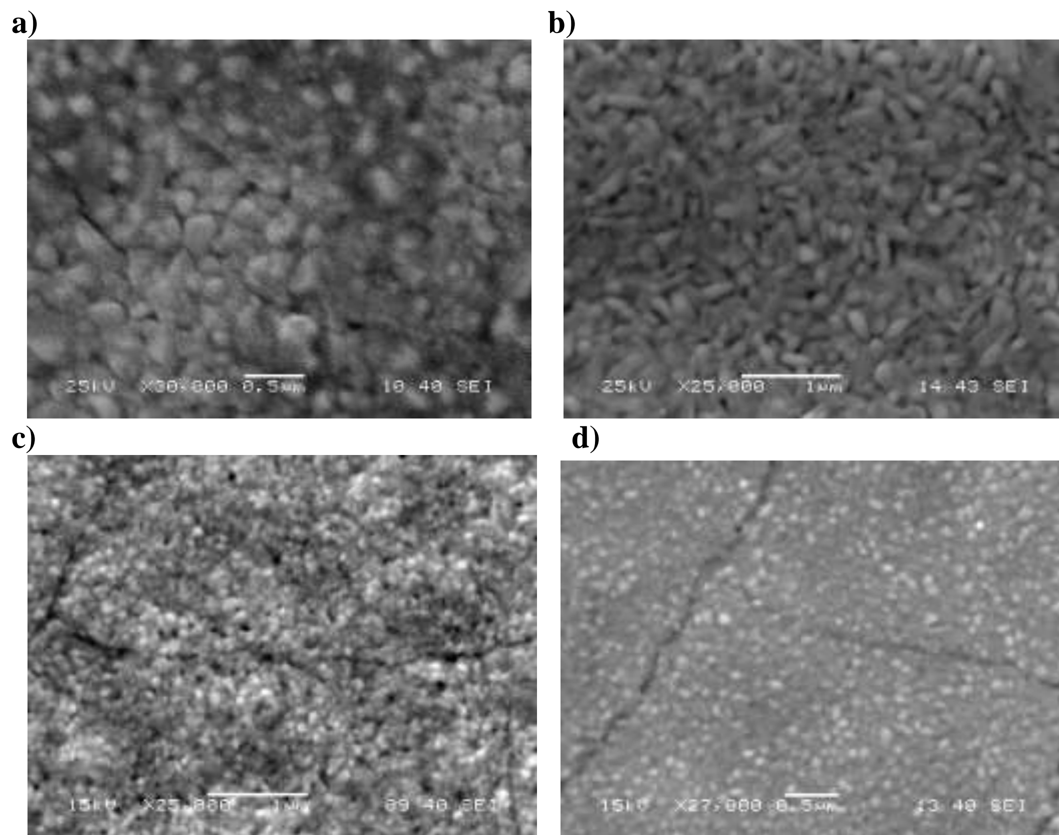

Figure 6.3. SEM micrographs of (a) BTO, (b) x = 0.30, (c) x = 0.50 and (d) x = 1.00. Gadolinium content in BTO thin films on $Pt/TiO_2/SiO_2/Si$ substrate.

large plate like grains Fig. 6.3 (b). The BGdTO thin films were composed of spherical grains. The substitution of Gd^{3+} for Bi^{3+} in $Bi_4Ti_3O_{12}$ films lead to reduction in grain size when the Gd content increase.

6.3.2 Micro Raman analysis

Figure 6.4 shows the room temperature Raman spectra of the polycrystalline BGdT thin films in backscattering geometry using JY T64000 triple-monochromator. An optical microscope with 80X objective was used to focus the 514.5 nm excitation radiation from a Coherent Innova 99 Ar^+ laser and to collect the scattered radiation. The scattered signal was detected by a charge-couple device (CCD) detection system. The Raman selections rules in Aurivillius $Bi_4Ti_3O_{12}$ allow 16 phonon modes of different symmetries ($6\ A_{1g} + 2\ B_{1g} + 8\ E_g$) if a tetragonal structure of the lattice is considered. It consist of Bi_2O_2 layers and perovskite-type structures ($A_{n-1}B_nO_{3n+1}$) with triple TiO_6 octahedra and A site Bi atom. The Bi^{3+} ion in A site is strongly under bonded and Ti^{4+} ion in B site is slightly over bonded. However, different numbers of Raman modes from $Bi_4Ti_3O_{12}$ have been reported in the literature[9-11], which can be explained by the possible overlap of the same symmetry vibrations and orthorhombic distortions of the material[12]. Figure 6.4 shows the room temperature recorded Raman spectra of $Bi_{4-x}Gd_xTi_3O_{12}$ films for compositions: x = 0.00, 0.20, 0.25, 0.30, 0.46, 0.50, 0,60, 0.70, 0.75, 0.85 and 1.00. The Raman modes of $Bi_4Ti_3O_{12}$ films are in agreement with those observed in its crystal[9]. The film spectrum exhibits intense phonon modes at about 28, 45, 62, 115, 270, 540 and 850 cm^{-1} and many other weak features. As the vibrational modes strongly depend on the

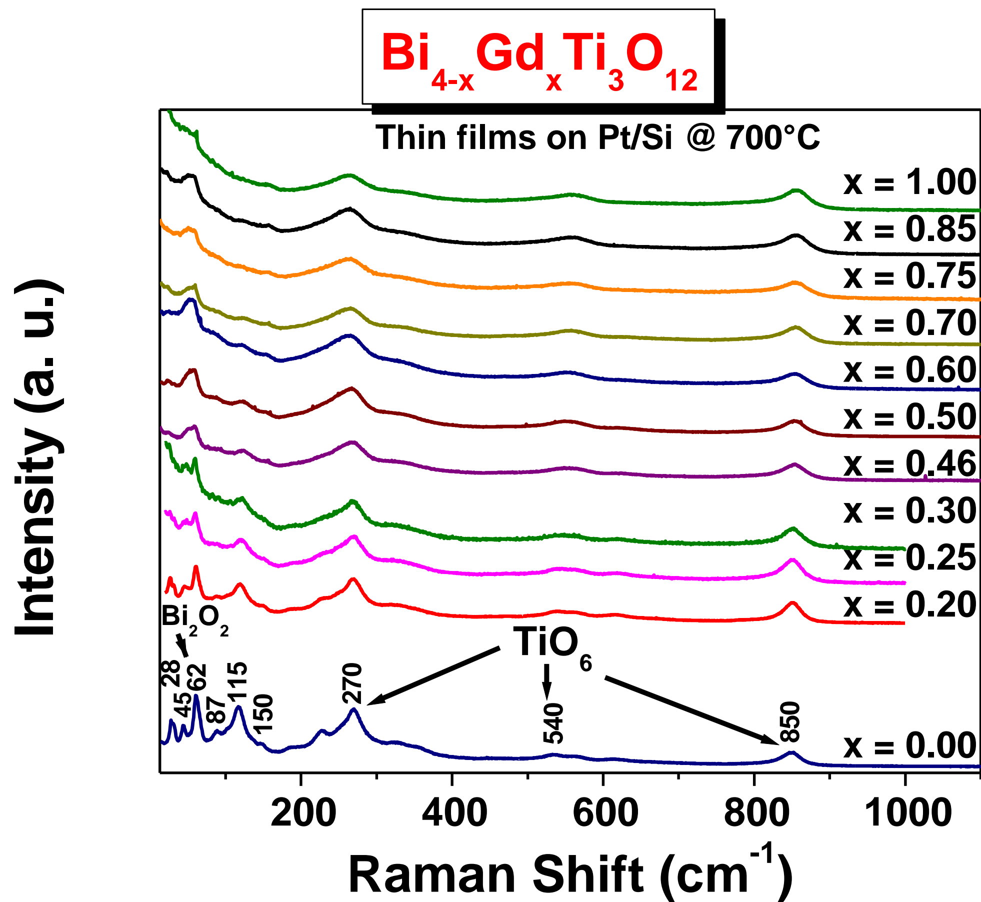

Figure 6.4. Room temperature Raman spectra of $Bi_{4-x}Gd_xTi_3O_{12}$ films on a Pt substrate ($Pt/TiO_x/SiO_2/Si$) for x = 0.00, 0.20, 0.25, 0.30, 0.46, 0.50, 0,60, 0.70, 0.75, 0.85 and 1.00 composition. The indexes in the figure indicate peculiar modes to the local structures.

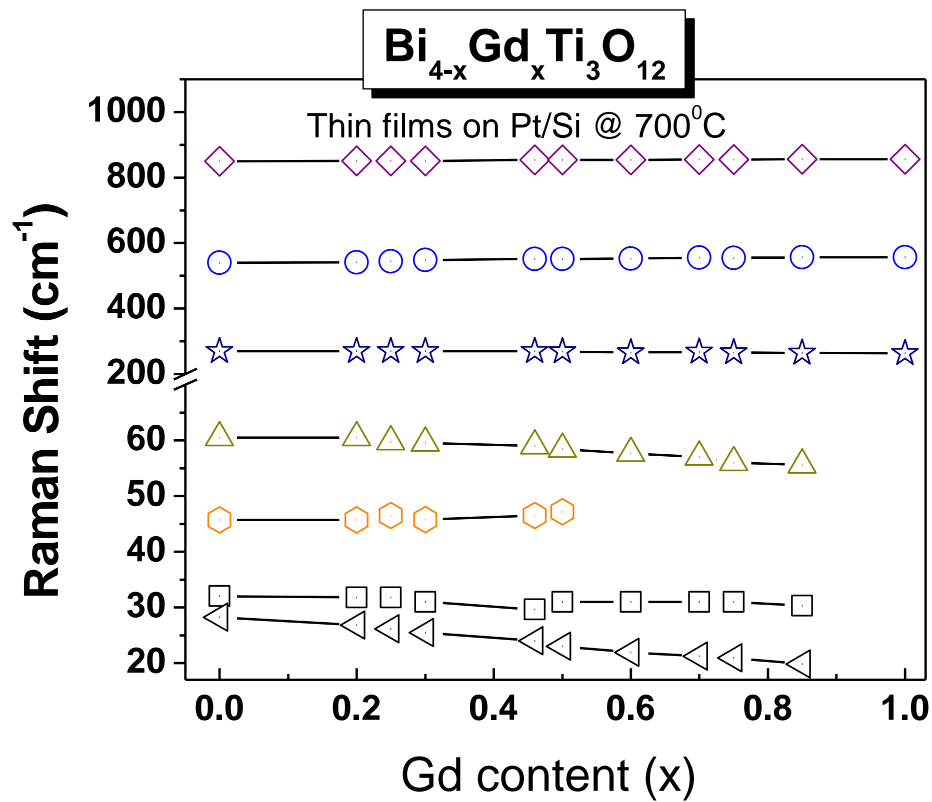

Figure 6.5. Raman frequencies as a function of Gadolinium compositions in $Bi_{4-x}Gd_xTi_3O_{12}$ thin films.

atomic masses, the heavy Bi ions should be responsible for the low frequency modes (ν <100 cm^{-1}). The 60 cm^{-1} mode is known to originate from[9,10] the Bi displacements in Bi_2O_2 layer. The modes at about 270, 540 and 850 cm^{-1} are the internal modes of TiO_6 octahedra having A_{1g} character. The compositional dependence of Raman spectra shows the similar effects on these internal modes they weaken and broaden with increasing content of Gd in films. Such changes are possible as Gd substituted is expected to introduce cationic disorder even though there is only a small difference in the ionic radii of Bi^{+3} and Gd^{+3} ions. The triplet bands at 87, 115 and 150 cm^{-1}, which were assigned to the modes of Bi ions (A site), became diffuse and their frequency increased clearly with increasing Gd content. If Gd substitutes Bi on the A-sites of the lattice, an increase in the mode frequency is expected from the mass difference as Bi is 1.33 times heavier than Gd. which is in accordance with the observed hardening of these modes. These results suggest that the Gd^{3+} ions are mainly incorporated into the Bi site (A site) of the perovskite slab for low Gd contents ($x < 0.85$). The 150 cm^{-1} mode gradually shifts to higher frequency with increasing intensity as the Gd content in films increases. This mode can be assigned to the A_{1g} character involving A-site Bi vibrations. Most prominent effect of Gd substituted was observed on the low frequency modes. The Raman frequencies were obtained for each composition by fitting the peaks with the damped harmonic oscillator-type phonon functions Gd are plotted in figure 6.5. The lowest frequency (28 cm^{-1}) mode, which has been assigned as a soft-mode responsible for a phase transition at 675°C, shows softening behavior with Gd substituted. Compared to the soft mode, a little variation in the 32 cm^{-1} mode and the 62 cm^{-1} mode suggest that the

substituted process least affects the Bi_2O_2 layers. The up-shift of 45 cm^{-1} mode with increasing Gd composition rules out its origin in Bi_2O_2 layers. This 45 cm^{-1} mode merges with the 62 cm^{-1} mode at x = 0.50. Additionally, vanishing of the low frequency modes (ν = 28, 32, 115 cm^{-1}) as well as a small but abrupt change in the TiO_6 octahedral frequencies around x = 0.85 reflects a compositional induced structural transition in $Bi_4Ti_3O_{12}$ at that composition.

6.3.3. Ferroelectric properties of $Bi_{4-x}Gd_xTi_3O_{12}$ thin films

For ferroelectric measurements, the top circular electrodes of platinum 200 nm thick and 200 μm diameter were deposited by dc sputtering. Ferroelectric response was recorded by RT6000HVS probe (Radiant Tech.) in virtual ground mode. For comparison, the ferroelectric response for the $Bi_{4-x}Gd_xTi_3O_{12}$ films of the same thickness (0.40 μm) and different compositions x = 0.00, 0.20, 0.30, 0.36, 0.46, 0.56, 0.60, and 0.70 is show in Fig.6.6. A polarization (2Pr = 55 μC/cm^2) for the films of composition x = 0.30 is Fig. 6.6 shows the coercive field Ec = 159 kV/cm for a maximum applied electric field 500 kV/cm. For other compositions the polarization is much lower. The effects of the Gd-content on the variation of the remanent polarization (Pr) and the coercive field (Ec) of GdBTO thin film were systematically examined at an applied electric field. As presented in figure 6.7, the value of the P_r increases gradually with increasing Gd-content for x below a certain critical level. The P_r shows its maximum value of 27.5 μC/cm^2 at x = 0.30 and decreases thereafter. The E_c increases rather steeply with increasing Gd-content from 48 to 182 kV/cm. The E_c shows its maximum value at x = 0.70. These

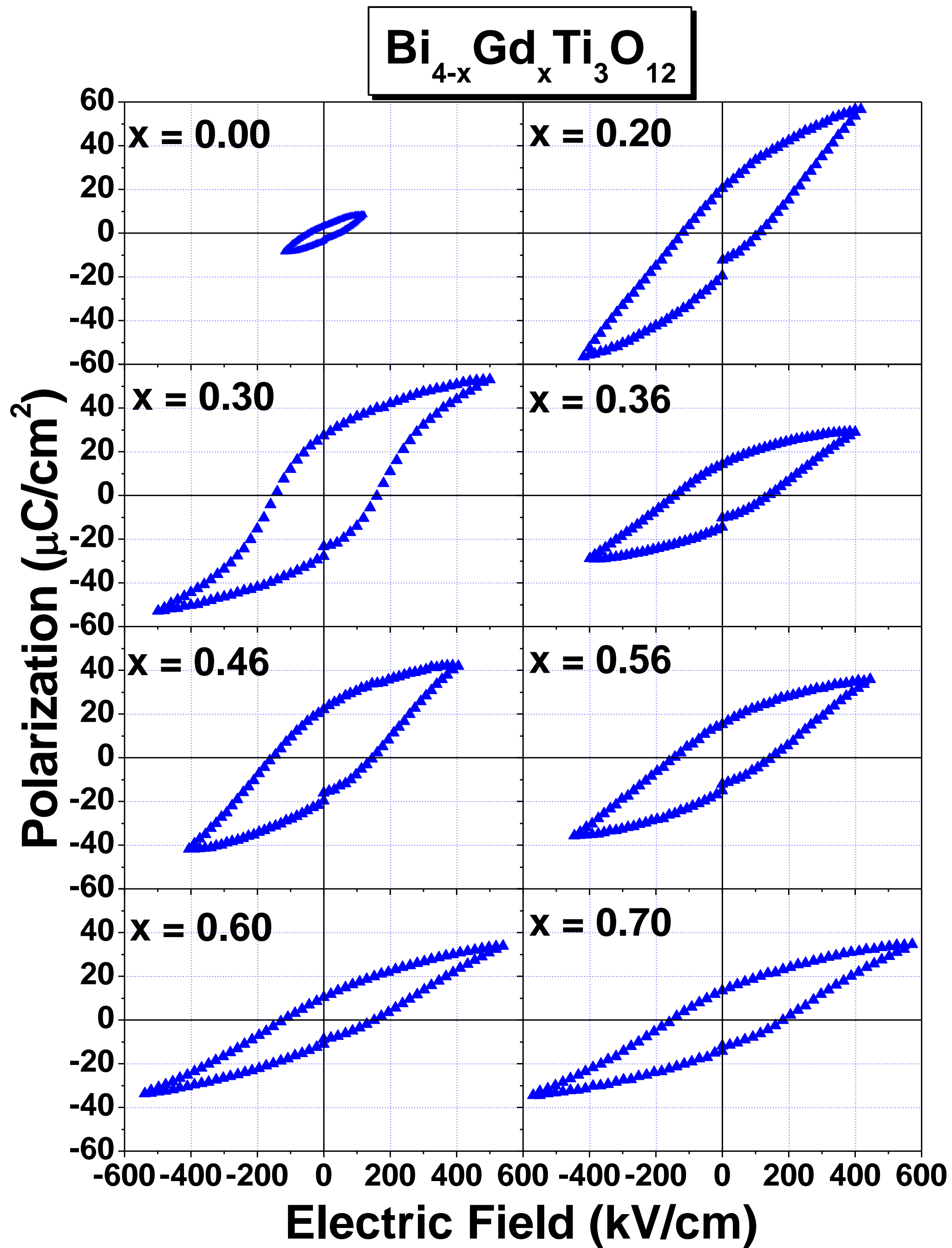

Figure 6.6. Ferroelectric response of the $Bi_{4-x}Gd_xTi_3O_{12}$ thin films for x = 0.00, 0.20, 0.30, 0.36, 0.46, 0.56, 0.60, and 0.70, on Pt ($Pt/TiO_2/SiO_2/Si$) substrate at 700°C.

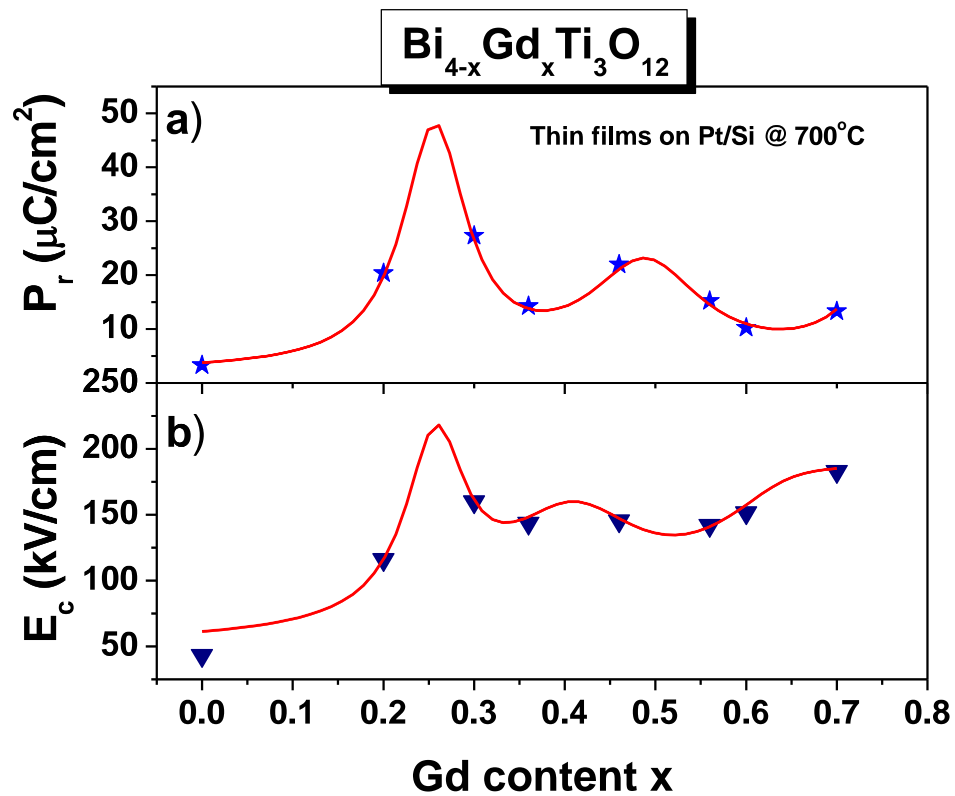

Figure 6.7. The values of a) the remanent polarization (P_r) and b) the coercive field (E_c) of the $Bi_{4-x}Gd_xTi_3O_{12}$ thin films for x = 0.00, 0.20, 0.30, 0.36, 0.46, 0.56, 0.60 and 0.70, on Pt ($Pt/TiO_2/SiO_2/Si$) substrate at 700°C.

results indicate that the substitution of Gd for Bi in BTO crystals substantially increases the P_r value because the contribution of both *a*-axis polarization and *c*-axis polarization component. This explain he relative high remnant polarization of the (117) preferred oriented[14] $Bi_{3.70}Gd_{0.30}Ti_3O_{12}$ compared to the highly c-axis oriented BGdT (with x = 0.85) obtained for Chon[15].

Figure 6.8 shows the fatigue response of the $Bi_{3.70}Gd_{0.30}Ti_3O_{12}$. A triangular waveform of 100 kHz frequency with electric field (375 kV/cm) was used to measure the fatigue test, under $0.4x10^9$ cycles at a frequency of 1 MHz. 1.42 % degradation of P_r is observed in the film. It is quite clear that the BGdT films have good fatigue resistance. These improved fatigue characteristics of the Gd-substituted BTO thin films may be attributed to lesser oxygen vacancies in the perovskite layers than the BTO thin films annealed at 700°C.

6.3.4 Dielectric properties of $Bi_{4-x}Gd_xTi_3O_{12}$ thin films

Figure 6.9 a) shows the variation of dielectric constant and loss (tan δ) with applied electric field at 1 MHz. The typical butterfly shape of the measured dielectric constant-electric field in Fig. 6.9 a) clearly indicate the ferroelectric nature of $Bi_{3.70}Gd_{0.30}Ti_3O_{12}$ thin films. The peak was observed at about ± 80 kV/cm, for a maxima applied electric field of ± 250 kV/cm which corresponded to positive and negative coercive fields. The dielectric constant and the dissipation factor (tan δ) of the $Bi_{3.70}Gd_{0.30}Ti_3O_{12}$ film capacitor were measured at 25^0C as a function of frequency. As shown in Fig. 6.9 b), The Dielectric constant and the dissipation factor are 333 and 0.039

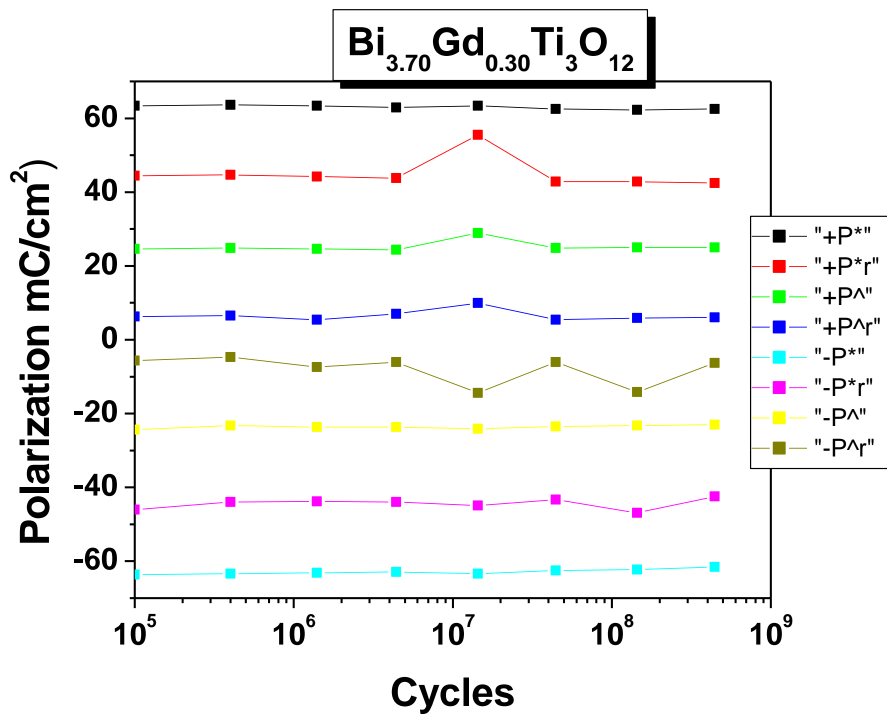

Figure 6.8. Fatigue characteristics of the $Bi_{3.70}Gd_{0.30}Ti_3O_{12}$ film deposited on Pt ($Pt/TiO_2/SiO_2/Si$) substrate and annealed at 700^0C, under $0.4x10^9$ cycles at a frequency of 1 MHz.

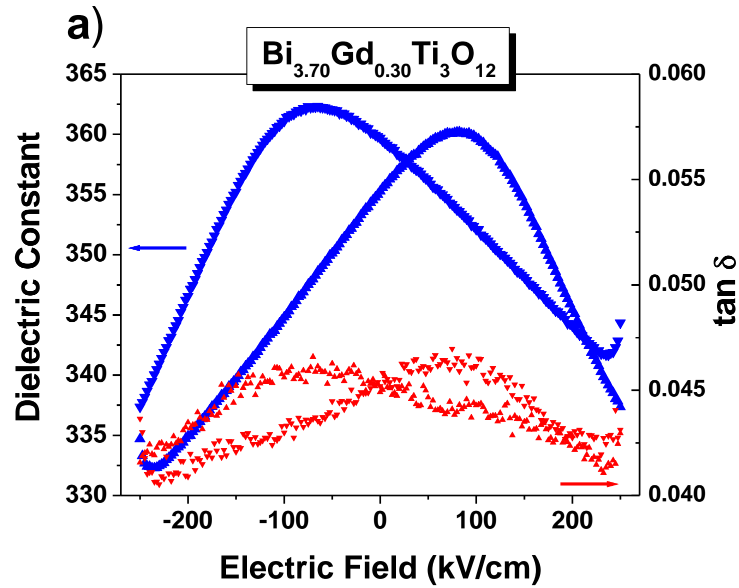

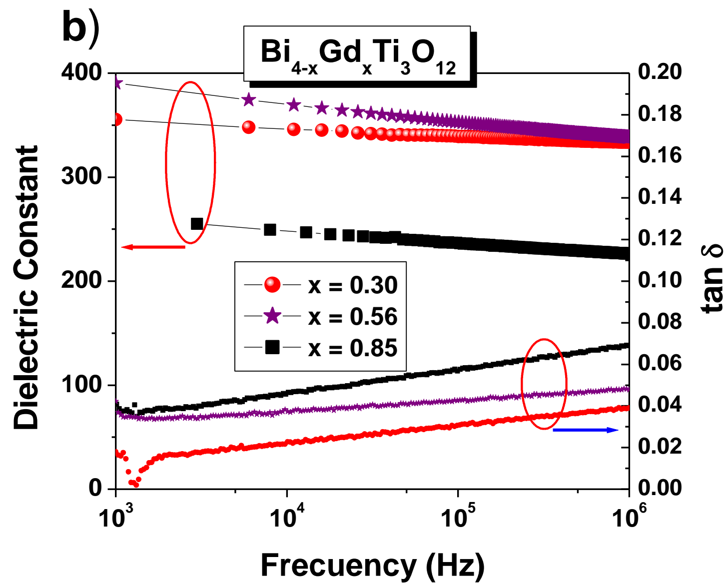

Figure 6.9. a) Dielectric constant and loss (tan δ) vs applied electric field on $Bi_{3.70}Gd_{0.30}Ti_3O_{12}$ film at 1 MHz, and b) dielectric constant measured at 25^0C as a function of frequency on x= 0.30 ,0.56 and 0.85 in the range between 1 kHz and 1 MHz.

at a frequency of 1 MHz, respectively. These values are comparable to BGdT (x = 0.56 and x = 0.85) and those of PZT, SBT, and LBTO capacitors. Although the dielectric constant decreases steadily with increasing frequency, there is no sudden change in its value up to 1 MHz. The dissipation factor (tan δ) shows little change with increasing frequency up to 1 MHZ. All these indicate that the observed ferroelectric response of the $Bi_{4-x}Gd_xTi_3O_{12}$ capacitor mostly originates from the ferroelectric polarization switching of bound charges, not form the response of freely moving charges. The frequency dispersion characteristics of dielectric constant and loss tangent in Fig.6.9 b) unambiguously indicate that $Bi_{3.70}Gd_{0.30}Ti_3O_{12}$ film have large distribution of relaxation time associate with polarize species. Since the range of frequency measurement is relatively low in the case presented, the dispersion is probably due to species with large masses. The most likely source of massive dipoles in these materials is abundance of oppositely charged species in the form of Bi and oxygen vacancy that can form during the high temperature process steps. The dipole concentration, for example, Bi and oxygen vacancy pairs, would depend on the processing conditions. A distribution in relaxation time is expected if the dipoles find themselves in varying environments due to random disorder in the sample. Hence, the presence of random disorder, whose degree is dependent on processing conditions, would give rise to dispersion in dielectric properties. Since the conversion of as deposited amorphous phase to layered Aurivillius phase involves the random nucleation of intermediate phases (e.g., fluorite), large number of defective regions develop in thin films. These defective regions don not have the opportunity to relax since the temperature is not sufficient for defect migration and

annihilation. It can be observed from frequency dispersion measured values shown in Fig. 6.9 b) that the loss tangent (tan δ) at higher frequencies is about 3.9 % which is comparable with the well established ferroelectric materials such as ferroelectric lead zirconate titanate and SBT.

6.3.5 Leakage current properties of $Bi_{4-x}Gd_xTi_3O_{12}$ thin films

For leakage current measurements, the steady dc conductivity was examined by the leakage current density (J) versus electric field (E) characteristics. Figure 6.10 shows the J-E characteristics of $Bi_{4-x}Gd_xTi_3O_{12}$ films on Pt ($Pt/TiO_2/SiO_2/Si$) substrate for the compositions: x = 0.00, 0.30, 0.56, and 0.85.by Sol-Gel route and spin coating. The linear increase of leakage current density under low fields, and point of inflexion at certain intermediate field is clearly observed in each composition of BGdT films. The careful observation of Fig. 6.10 data indicates that the current follow ohmic behavior for low fields, and at higher field after point of inflexion until the dielectric breakdown occurs. Because, film is thick (0.40 μm), tunneling phenomena can be ruled out, and Ln J vs $E^{1/2}$ does not show nonlinear ohmic conduction, Poole-Frenkel current is also not valid. It is important, however, to note that pure $Bi_4Ti_3O_{12}$ film of same thickness show much large leakage current in comparison with Gd substituted $Bi_4Ti_3O_{12}$ films. One can also observe in Fig. 6.10 that $Bi_{4-x}Gd_xTi_3O_{12}$ films with the composition x = 0.30 showed the lowest leakage current (< 10^{-9} A/cm^2) under low fields. In general, BGdT films show dielectric breakdown after point of inflexion at certain high field for each composition. Leakage current of Fig. 6.10 reveals that in pure of $Bi_4Ti_3O_{12}$ films, after inflexion, is limited by

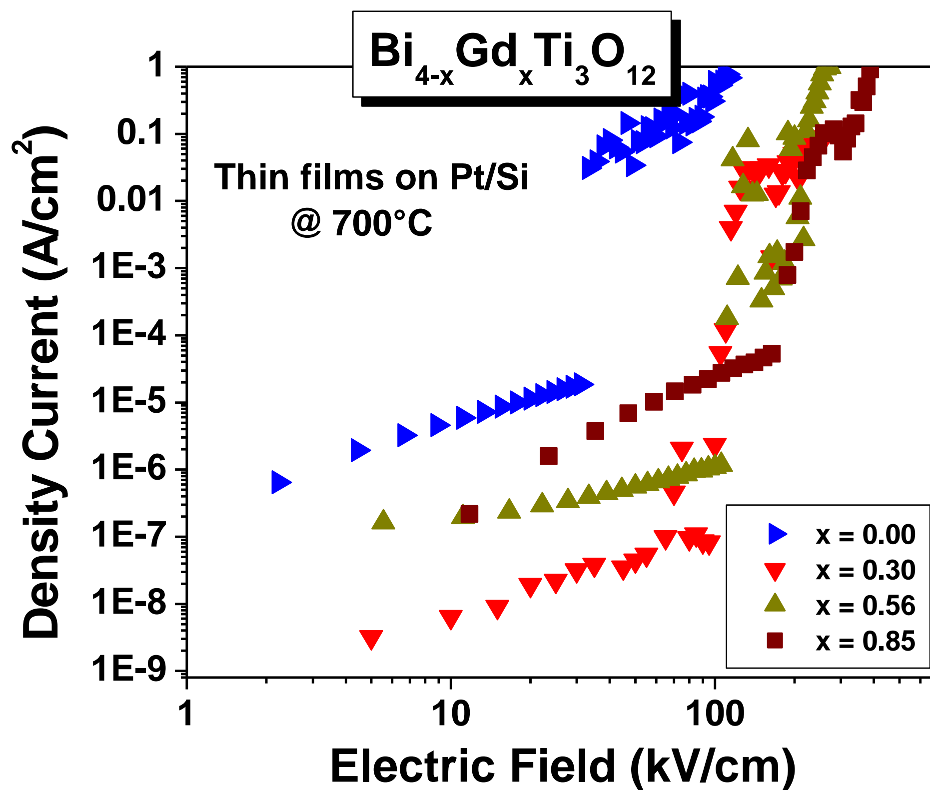

Figure 6.10. Leakage current at room temperature of the $Bi_{4-x}Gd_xTi_3O_{12}$ thin films deposited on Pt ($Pt/TiO_2/SiO_2/Si$) substrate and annealed at 700°C for the compositions: x = 0.00, 0.30, 0.56, and 0.85.

the space charge conduction. In dielectrics, the low field region, current flows in the film and it controlled by the bulk i.e. homic behavior, and in intermediate fields, grain boundary regions may be effective, and under very high fields, space charge limited current (SCLC) and electrode-film interfacial resistance may dominate. But, in the case of BGdT for most compositions, films, dielectric breakdown occurs at higher field. Thus, in BGdT films, homic behavior dominates the leakage current transport in low field region and inflexion region. These results indicate that the lower leakage current results from Gd preventing Bi from evaporating, and the higher leakage current is due to the evaporation of Bi during annealing.

These experimental results imply that Gd ions substituting for Bi ions suppresses the generation of oxygen vacancies and reduces the leakage current. In fact, for the BGdT films with x = 0.30, Gd substituted BTO results in a much larger P_r, than that of pure BTO. This implies that Gd substituted BTO leads to efficient decrease in space charge density.

6.4. Magnetic properties

The magnetic properties of the $Bi_{3.15}Gd_{0.85}Ti_3O_{12}$ powder were measured using a Quantum Design MPMS superconducting quantum interference device (SQUID) magnetometer. The zero field cooled (ZFC) magnetization variation with temperature was measured at 100 Oe of applied magnetic field are shown in Fig. 6.11. Measured magnetization was divides by the total mass of the powder used. At room temperature, the magnetization curve exhibits no hysteresis, indicating the super-paramagnetic

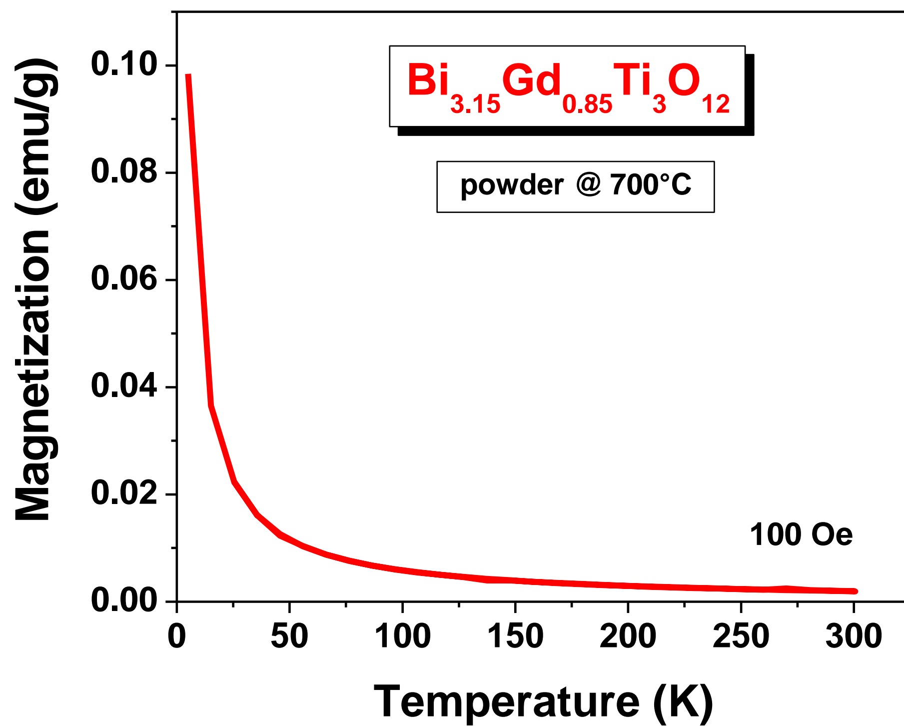

Figure 6.11. Magnetization as a function of temperature at 100 Oe magnetic field of the powder $Bi_{3.15}Gd_{0.85}Ti_3O_{12}$.

behavior, however, the powder eshibit very small ferromagnetic magnetization (σ_r = 5.4 x 10^{-4} emu/g and coercitivity Hc = 20 Oe at 5 K as shown in Fig. 6.12. The remarkable feature of magnetization curves is that the magnetization is far from saturation up to the highest field applied of 50 kOe even at 300 K, which is above the blocking temperature of the sample. This is an indication of strong surface-spin pinning at the particle/support interface, resulting in a non-collinear spin structure within the $Bi_{3.15}Gd_{0.85}Ti_3O_{12}$ particles.

6.5 Conclusions

Gadolinium substituted $Bi_4Ti_3O_{12}$ thin films and powder prepared by Sol-Gel methods was investigated for ferroelectric and magnetic response. Structural studies indicate Gd substitution A-site. $Bi_{4-x}Gd_xTi_3O_{12}$ thin films with several compositions were examined for dielectric, ferroelectric, leakage current and magnetic response. Ferroelectric response for several compositions reveals polarization Pr, values in the range form low 3.3 μC/cm^2 to higher 27.5 μC/cm^2 for different compositions of $Bi_{4-x}Gd_xTi_3O_{12}$ films. However, after 0.4 x 10^9 switching cycles, fatigue-free is observed in the film with x = 0.30. At lower field, the leakage current is dominated by ohmic behavior. $Bi_{3.15}Gd_{0.85}Ti_3O_{12}$ powder shows magnetic behavior with very small remnance at 5 K. The magnetization remain unsaturated up to the highest field applied of 50 kOe. This is an indication of strong surface-spin pinning at the particle/support interface. The feature of magnetic behavior and the presence of ferroelectricity points to the bi-functionality of $Bi_{3.15}Gd_{0.85}Ti_3O_{12}$. Further studies are underway to understand the origin of magnetism and its coupling with ferroelectric polarization.

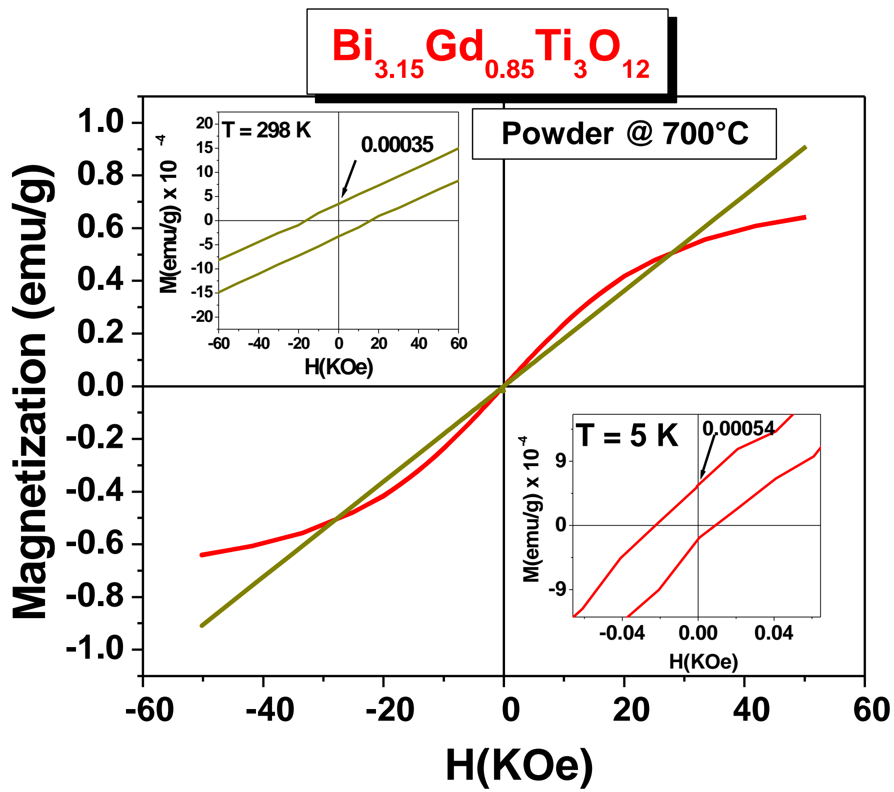

Figure 6.12. Magnetization Vs applied magnetic field for $Bi_{3.15}Gd_{0.85}Ti_3O_{12}$ powder at 300 and 5 K.

6.6 References

1. B. Aurivillius, Ark Kemi 1 463 (1949).

2. E. C. Subbarao, J. Phys. Chem. Solids 23, 665 (1962).

3. R. A. Armstrong and R. E. Newnam, Mater. Res. Bull. 7, 1025 (1972).

4. D. damjancovic, Rep. Prog. Phys. 61, 1267 (1998).

5. R. L. Withers, J. G. Thompson, and A.D. Rae, J. Solid State Chem. 94, 404 (1991).
6. B. H. Park, B. S. Kang, S. D. Bu, T. W. Noh, J. Lee, and W. Jo, Nature (London) 401, 682 (1999).

7. M. S. Tomar, R. E. Melgarejo, A. Hidalgo, S. B, Majumder, and R. S. Katiyar, Appl. Phys. Lett. 81, 341 (2003).

8. D. Cullity, *Elements of X-ray diffraction* (Addition-wesley publishing Co., Inc USA, 1967) p 261.

9. P. R. Graves, G. Hua, S. Myhra, and J. G. Thompson, J. Solid State Chem. 144, 112 (1995).

10. S. Kojima, R. Imaizumi, S. Hamazaki, and M. Takaahige, Jpn. J. Appl. Phys. **33**, 5559 (1994).

11. M. Osada, M. Tada, M. Kakihama, T. Watanabe, and H. Funakubo, Jpn. J. Appl. Phys. Part 1, **40**, 5572 (2001).

12. S. Kojima and S. Shimida, Physica, **B 219-220**, 617 (1996).

13. U. Chon, H. M. Jang, M. G. Kim, and C. H. Chang, Phys. Rev. Lett. **89**, 087601 (2002).

14. M.S. tomar, R.E. Melgarejo, R. Singhal, L. Angelats and R. S. katiyar Mater. Res. Soc. Sump. Proc. Vol 888 V08-09.1 (2006).

15. U. Chon, H.M. Jang, N. S. Shin, J. S. Kim, D. C. Ahn, Y. S. Kim and K. No, Physica B, **338**, 190 (2007).

Chapter 7

7.1 Conclusions

Ferroelectric $Bi_4Ti_3O_{12}$ (BTO) and its rare earth (La, Nd, Sm, Gd)-substituted derivatives thin films were synthesized using a sol-gel method. Polycrystalline $Bi_{4-x}M_xTi_3O_{12}$ (M = La, Nd, Sm, Gd) films of Bi-layered perovskite were crystallized on $Pt/TiO_2/SiO_2/Si$ substrates at 700°C with preferential (117) orientation. $Bi_{3.44}Nd_{0.56}Ti_3O_{12}$ thin film showed the best saturation properties of ferroelectrics with large P_r = 70 μC/cm^2 and small E_c = 148 kV/cm, and enhanced fatigue-free behavior. Because the contribution of both *a*-axis polarization and *c*-axis polarization component. Have superior dielectric constant and loss of 434 and 0.07 respectively in the frequency of 1MHz. These film exhibit a relatively lower leakage current density (5.3 x 10^{-7}A/cm^2 at 100 kV/cm). On the other hand, $Bi_{3.15}Gd_{0.85}Ti_3O_{12}$ powder was tested using SQUID, which showed super-paramagnetic at room temperature and magnetic at 5 K with magnetic coercitivity (Hc = 29 Oe). Rare earth ions (La, Nd, Sm, Gd) substituted BTO thin films investigated in the present study, especially $Bi_{3.44}Nd_{0.56}Ti_3O_{12}$ film, is considered as potential candidate for non-volatile memory devices.

All the results are shown in following table 7.1 indicating the responses.

Table 7.1 Results of properties Ferroelectric, dielectric and leakage current of rare earth substituted bismuth titanates

Compositions	P_r ($\mu C/cm^2$)	E_c (kV/cm^2)	Fatigue 10^9cycles (reduction)	tan δ at 1MHz	Dielectric constant K at 1 MHz	Leakage current (A/cm^2) at 65 kV/cm
$Bi_{3.44}Nd_{0.56}Ti_3O_{12}$	70	150	8.6%	0.07	434	$3.5E^{-7}$
$Bi_{3.44}La_{0.56}Ti_3O_{12}$	47.59	100	15.3%	0.09	535	$1.2E^{-6}$
$Bi_{3.30}Sm_{0.70}Ti_3O_{12}$	29	70	0.06%	0.039	344	$9.6E^{-7}$
$Bi_{3.70}Gd_{0.30}Ti_3O_{12}$	27.5	79.5	1.42%	0.039	333	$9.8E^{-8}$